

**Scuola di Scienze  
Dipartimento di Fisica e Astronomia  
Corso di Laurea Magistrale in Fisica**

**NOVEL ORGANIC SEMICONDUCTING  
SMALL MOLECULES FOR X-RAY  
DETECTION**

**Relatore:  
Prof.ssa Beatrice Fraboni**

**Presentata da:  
Tommaso Neri**

**Correlatore:  
Dott.ssa Laura Basiricò**



# Abstract

*L'elettronica organica* ha trovato negli anni recenti diverse applicazioni, anche in dispositivi di uso quotidiano, come ad esempio gli schermi OLED (Organic Light Emitting Diode). I semiconduttori organici possono essere depositati con tecniche a basso costo, anche su scala industriale, e su grandi aree, fattore, quest'ultimo, che li rende particolarmente adatti alla fabbricazione di sensori di radiazioni ionizzanti. Il lavoro presentato riguarda la realizzazione di transistor organici a film sottile e la loro caratterizzazione, come transistor e come sensori di raggi X. In particolare, l'obiettivo di questo progetto sperimentale è il confronto delle sensibilità di due tipi di dispositivi fabbricati da soluzioni delle molecole diF-TES-ADT (5,11-bis(triethylsilylethynyl)anthradithiophene) e diF-TEG-ADT (5,11-bis(triethylgermylethynyl)anthradithiophene), appartenenti alla classe degli eteroaceni sostituiti. Nella prima molecola sono presenti due gruppi funzionali identici in cui è contenuto un atomo di silicio, mentre nell'altra essi contengono un atomo di germanio, caratterizzato da un numero atomico più alto. In questo lavoro viene dimostrato che il numero atomico più alto, grazie al maggiore coefficiente di assorbimento per la radiazione X, comporta una sensibilità più alta per il sensore di radiazioni ionizzanti, come confermato dai risultati ottenuti.

# Abstract

In recent years *Organic electronics* has known a good development, and nowadays the organic semiconductors are employed in several applications, even in everyday-use devices, like the OLED (Organic Light Emitting Diode) screens. Organic devices can be realized by depositing the organic semiconductors by low cost techniques easily extendable to the industrial scale. Moreover, the possibility to realize the deposition over large areas makes them particularly suitable for the fabrication of ionizing radiation detectors. In this experimental work two types of thin film organic transistors were fabricated with solutions of two molecules, and then they were characterized electrically as transistors and as X-ray detectors. The motivation of this thesis is the comparison of the sensitivities of two types of devices, realized respectively with solutions of diF-TES-ADT (5,11-bis(triethylsilylethynyl)anthradithiophene) and diF-TEG-ADT (5,11-bis(triethylgermylethynyl)anthradithiophene) molecules, belonging to the class of substituted heteroacenes. In the structure of the first molecule there are two identical functional groups containing a silicon atom, whereas in the second one these functional groups have a germanium atom, characterized by a higher atomic number. In the thesis we demonstrate that the higher atomic number, thanks to its higher X-ray absorption cross section, leads to a higher sensor sensitivity, as confirmed by the results obtained.

# Contents

Introduction .....	1
1. Organic Electronics .....	3
1.1. Charge carrier transport in organic semiconductors .....	6
1.1.1. Mobility and dependence on temperature .....	7
1.1.2. Mobility and dependence on electric field .....	7
1.1.3. Charge injection into organic semiconductors .....	9
1.2. Organic field effect transistors .....	11
1.2.1. Organic small molecule for OFETs: soluble acenes and heteroacenes .....	14
2. Ionizing radiation detection .....	23
2.1. Ionizing radiation interaction with matter .....	24
2.1.1. Photoelectric absorption .....	24
2.1.2. Compton scattering .....	25
2.1.3. Pair Production .....	26
2.2. Simplified detector model .....	27
2.3. Detection of X-rays and $\gamma$ -rays .....	29
2.4. Organic direct ionizing radiation detectors .....	31
2.4.1. Organic Direct Detectors based on Thin Films .....	31
2.4.2. Organic direct detectors based on Organic Semiconducting Single Crystal (OSSC) .....	42
2.5. Detector based on alternative materials: perovskites .....	48
2.6. Hybrid organic/inorganic ionizing radiation detectors .....	50
3. Materials and methods .....	56
3.1. Devices preparation .....	57
3.1.1. Fabrication of drop-casted samples .....	58
3.1.2. Fabrication of spin-coated samples .....	59
3.2. Electrical characterization .....	59
3.3. X-Ray photoresponse characterization .....	62
3.4. Data Analysis .....	68
4. Results and discussion .....	72

4.1	Devices realized by drop-casting from solutions at wt.0.5% .....	73
4.2	Devices realized by spin-coating from solutions at wt.1.2% .....	79
4.3	Devices realized by spin-coating from solutions at wt.0.5% .....	86
4.4	Devices realized by spin-coating from solutions at wt.2% .....	94
Conclusions .....		100
Appendix .....		103
A.1	Leakage current plots and raw data plots .....	103
A.1.1	Devices realized by drop-casting from a solution of diF-TES-ADT at wt.0.5% .....	104
A.1.2	Devices realized by drop-casting from a solution of diF-TEG-ADT at wt.0.5% .....	105
A.1.3	Devices realized by spin-coating from a solution of diF-TES-ADT at wt.1.2% .....	106
A.1.4	Devices realized by spin-coating from a solution of diF-TEG-ADT at wt.1.2% .....	107
A.1.5	Devices realized by spin-coating from a solution of diF-TES-ADT at wt.0.5% .....	108
A.1.6	Devices realized by spin-coating from a solution of diF-TEG-ADT at wt.wt.0.5% .....	109
A.1.7	Devices realized by spin-coating from a solution of diF-TES-ADT at wt.2% .....	110
A.1.8	Devices realized by spin-coating from a solution of diF-TEG-ADT at wt.2% .....	111
Bibliography.....		113

# Introduction

In the last years the *Organic electronics* has known a wide development. Until the first uses of the organic semiconductors, about 40 years ago, only their inorganic counterpart, mainly silicon and germanium, was employed in the realization of electronic devices. The main disadvantage of traditional inorganic materials consists in their fabrication, characterized by high energetic and economic costs. On the contrary, the most common organic semiconductors are soluble in organic solvents (often they are functionalized in order to obtain this solubility), and for this reason they can be deposited over the respective substrates by means of low-cost deposition technique realizable in a standard laboratory, and extendable to the industrial scale. Starting from 2007 the organic semiconductors have been proposed as direct X-ray detectors [1], however they are less stable over the time than the inorganic materials and not always reach high sensitivities, because of the low atomic number, and consequently low absorption cross section which characterizes them. In order to enhance the sensitivity, in the literature it is possible to find some solutions, like the addition in the active layer of the devices of nanoparticles with a high atomic number [2] [3], or the improvement of the conductivity, for example adding single walled carbon nanotubes, that provide a better mobility for holes [4].

The purpose of the experimental work carried out during this thesis is the comparison of the X-ray detection performance of two types of organic thin film transistors realized starting from solutions of two organic small molecules, diF-TES-ADT (5,11-bis(triethylsilylethynyl)anthradithiophene) and diF-TEG-ADT (5,11-bis(triethylgermylethynyl)anthradithiophene), belonging to the class of the substituted heteroacenes. In the structure of diF-TES-ADT there are two identical functional groups containing a silicon atom and in the structure of diF-TEG-ADT the same functional group contains a germanium atom. The germanium atom has a higher atomic number  $Z$  in comparison with silicon, for this reason a higher sensitivity should be expected for the device realized with diF-TEG-ADT. Within this work several devices were realized starting from solutions in chlorobenzene of the two molecules at three concentrations in weight (wt.0.5%. wt.1.2%, wt.2%). The solutions at wt.0.5% were deposited by means

of two deposition techniques, drop-casting and spin-coating, whereas the other ones were deposited only by spin-coating. The best performance as X-ray detector and the highest sensitivity were obtained with the devices realized from a solution of diF-TEG-ADT at wt.1.2% deposited by spin-coating.

In this thesis, the first chapter describes the properties of organic semiconducting materials, starting from their fundamental constituent: the carbon atom. Next, a description of the electrical behaviour of the organic semiconductor is reported and subsequently a paragraph is dedicated to the Organic Field Effect Transistors (OFETs), focusing on the organic small molecules most used for such application. The chapter finishes with an overview of the results reported in the literature in this field. The second chapter reports a description of the X-ray detectors, at first in general, and subsequently with a focus over the organic detectors. Finally, it reports a description of the results reported in the literature about the X-ray detectors realized with organic materials or hybrid organic/inorganic materials. In chapter 3 the experimental setups, the procedure of realization of the devices and the characterization carried out are presented. The subsequent chapter 4 illustrates the results obtained during this work.

# 1. Organic Electronics

Organic semiconducting materials are carbon-based materials. Its fundamental constituents, in addition to carbon, are hydrogen and other elements like oxygen, nitrogen, halogens, etc. The ground state of atomic carbon is formed by six electrons, two in 1s orbital, two in 2s orbital, and two in two of three 2p<sub>x</sub>, 2p<sub>y</sub>, and 2p<sub>z</sub> orbitals [5]. The wave-like behaviour of an electron may be described, according to quantum mechanics, by a complex wave function depending on position and time  $\psi(r,t)$ . The square modulus of this wave function,  $|\psi(r,t)|^2$ , is equal to a probability density, and its integral over a certain volume V gives the probability of finding the electron in that volume at the instant of time t. The region of the space in which this probability is at least the 90% is called atomic orbital and its shape depends on how the wave function is mathematically defined. Each orbital has a maximum of two electrons and it is characterized by a different set of quantum numbers [6].

In configuration  $1s^2 2s^2 2p_x^1 2p_y^1$  carbon can make only two covalent bonds, but when one of the 2s electrons move into the empty 2p<sub>z</sub> orbital it makes four covalent bonds. In this case, new *hybrid orbitals* are formed from a linear combination of the 2s-orbital with the 2p-orbitals, that is named *hybridization*. When all 4 orbitals (one 2s and three 2p-orbitals) are involved in the hybridization, the resulting four equivalent orbitals, named  $sp^3$  orbitals, point into the 4 corners of a tetrahedron with an angle of 109,5° between them (Figure 1.1) [5].

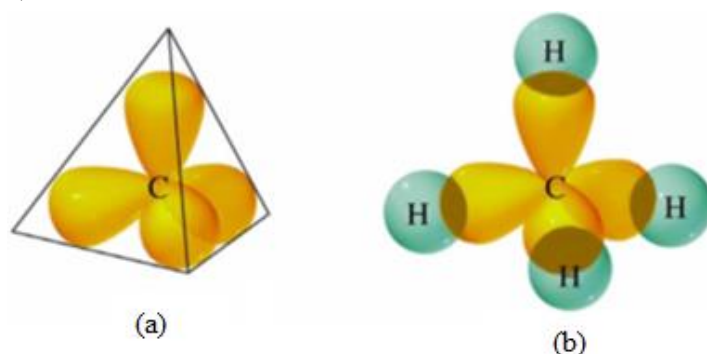


**Figure 1.1:** (a) Atomic carbon: the four  $sp^3$  orbitals are directed toward the corners of a tetrahedron. (b) The orbital structure of methane shows the overlap of the four  $sp^3$  orbitals of carbon with the s orbitals of four hydrogen atoms. Four  $\sigma$  (covalent) bonds between carbon and hydrogen are formed [7].

In more detail, hybridization is a mathematical process of linear combination of atomic orbitals of different type and similar energy within the same atom, that allows to achieve new hybridized isoenergetic orbital [8], more suitable for the description of molecule structure [9]. The number of bonds that a carbon atom makes is determined by the number of hybrid orbitals and remaining p-orbitals. In a chemical bond the electrons have equal probability to orbit around the first atom or around the second, so they cannot be assigned to atomic orbitals, but it is necessary to associate them with molecular orbitals, that are approximated as linear combination of atomic orbitals [5]. The bonds formed by s-orbitals or their hybrids and p-orbitals are called  $\sigma$ -bonds and the correspondent electrons are called  $\sigma$ -electrons [7].

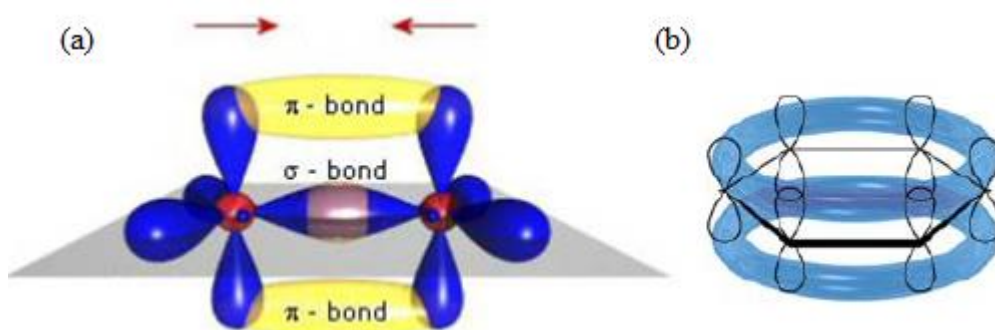


**Figure 1.2:** (a)  $\sigma$ -bond and  $\pi$ -bond [7]. (b) Aromatic ring: delocalization of  $\pi$  orbitals [10].

When one 2s-orbital combines with two of the three 2p-orbitals, three hybrid  $sp^2$ -orbitals lying on the same plane are formed. The unhybridized orbital ( $2p_z$ ), on the contrary, is standing perpendicular to them [7]. If two  $sp^2$ -orbitals, belonging to two different  $sp^2$  hybridized carbon atoms overlap, give rise to the so called  $\sigma$ -bond. When this bond is forming, also the unhybridized  $p_z$  orbitals start to interacting, and, as a result, they form the bond named  $\pi$ -bond (Figure 1.2a) [7].  $\sigma$ -bonds are very strong, and the respective electrons are not free to move, because they are too localized, thus they do not contribute to the charge transport mechanism. Therefore,  $\sigma$ -bonds form the skeleton of the structure, and moreover, are responsible for the geometrical properties of the resulting molecule. On the contrary,  $\pi$ -bonds are very weak and  $\pi$ -electrons are delocalized so they can freely move across the molecule, especially in presence of an electric field [7].

A class of molecule used in organic electronics is the one of the conducting polymers, whose key structure is a linear chain of conjugated units with alternate single and double bonds. In these macromolecules, the p-orbitals of the  $\pi$ -electrons overlap,

producing a reconfiguration of the arrangement of the electrons, that concerns the energy levels [7]. Another class of organic molecules used are the aromatic molecules, in which hybridized atom orbitals of carbon atoms are bounded by  $\sigma$ -bonds or  $\pi$ -bonds.  $\sigma$ -bonds are strong connection parallel to the molecular plane, whereas  $\pi$ -bonds are delocalized bonds that form molecular orbitals (Figure 1.2b) [10].

It is possible to separate the molecular energy levels into two categories:  $\pi$  and  $\pi^*$  bonding and anti-bonding respectively, which form a band-like structure (Figure 1.3). The occupied  $\pi$ -levels are equivalent to the valence band of inorganic semiconductors, whereas unoccupied  $\pi^*$ -levels are equivalent to the conduction band [7]. Two orbitals are very important: HOMO (Highest Occupied Molecular Orbital) and LUMO (Lowest Unoccupied Molecular Orbital). HOMO is the outer orbital occupied by electrons, and LUMO is the first unoccupied energy level [10].

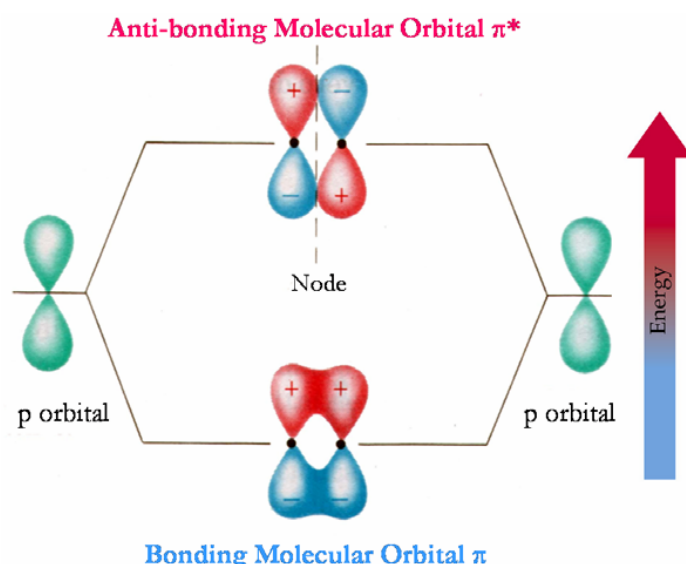


**Figure 1.3:**  $\pi$ -bonding and  $\pi^*$ anti-bonding molecular orbitals [7].

The band gap given by the difference between energies of HOMO and LUMO for polymers is given by the equation (1.1) [7]:

$$E_G = E_{\text{LUMO}} - E_{\text{HOMO}} = \frac{(N+1)^2 h^2}{8m_e (Nd)^2} \approx \frac{h^2}{8m_e d^2 N} \quad \text{for large } N \quad (1.1)$$

Where  $h$  is the Planck Constant,  $m_e$  the electron mass,  $N$  the number of atoms of polymeric chain and  $d$  the distance between the atoms within the polymeric chain.

In an aromatic molecule, similarly to a polymeric chain, an increase of aromatic rings (a longer chain) is associated to a smaller energy gap between HOMO and LUMO [10].

## **1.1. Charge carrier transport in organic semiconductors**

Several models have been developed to explain the charge transport in organic semiconductors, but a universal theory that can describe charge transport in organic materials does not exist and transport properties are not fully explained [7].

Inorganic semiconductors are characterized by very strong covalent bonds. In these materials charge carriers move as highly delocalized plane waves in wide bands and, usually, their mobility is very high. In this case the scattering of the carriers, mainly on phonons, thermally induced lattice deformations, limits the charge transport. In the organic semiconductors, on the contrary, the weak intermolecular interaction forces, usually van der Waals interactions, make the vibrational energy of the molecules similar to the intermolecular bond energy at or above room temperature, therefore the mean atomic distance can be bigger than mean free path of charge carriers, and consequently, transport occurs by hopping of charges between localized states; in this case charge transport is phonon assisted [7]. Organic disordered materials have a gaussian DOS, whereas their inorganic counterpart is characterized by an exponential DOS. In the former ones the relaxation process of excess charges, created for injection or photoexcitation at an arbitrary energy, occurs through relaxation into lower-lying energy states in the band tail as time evolves. In this case, the energy of photoinjected charges will eventually reach a steady state value, named equilibration energy,  $\epsilon_\infty$ . and the excited charges will undergo energy relaxation, reaching eventually the equilibrium at the given time  $t_{rel}$ . After  $t_{rel}$  transport will be determined by thermal excitation from equilibration energy  $\epsilon_\infty$  to the transport energy  $\epsilon_t$  [11].

### 1.1.1. Mobility and dependence on temperature

Temperature plays an important role in the charge transport mechanism. In single crystals, where the charge transport is bandlike and impeded by scattering processes, the mobility decreases with temperature, with a power law behaviour described by the equation (1.2) [11]:

$$\mu \approx T^{-b} \quad (1.2)$$

$b \in [1, -3]$  [6]

On the contrary, in disordered materials, where conduction, instead of band transport, is due to hopping between localized states, which occurs with thermal activation that allows to overcome the energy barriers between localized states, the mobility increases strongly with the temperature (Arrhenius dependence) as described by the equation (1.3) [11]:

$$\mu_{\text{Arrhenius}} \approx \mu_{\infty} e^{-\frac{E_a}{kT}} \quad (1.3)$$

Where  $\mu_{\infty}$  is a temperature independent prefactor and  $E_a > 0$  the activation energy.

The Gaussian disorder model (GDM) provides another parametrization (equation (1.4)) of the temperature dependence for mobility, obtained from the results of theoretical simulations for transport [11]:

$$\mu_{\text{GDM}} \approx \mu_{\infty} e^{-\left(\frac{T_0}{T}\right)^2} \quad (1.4)$$

Where  $T_0$  is related to the DOS width and gives an indication about the amount of energy disorder.

### 1.1.2. Mobility and dependence on electric field

When charge transport is due to hopping between localized states, the application of an electric field  $\vec{E}$  lowers the activation barrier (Figure 1.4) for charge transfer between two localized states with different energies  $\varepsilon_i$  and  $\varepsilon_j$  separated by a distance  $\vec{r}_{ij}$ , of an amount

$-\vec{q}\vec{r}_{ij}\cdot\vec{E}$ , allowing to the charge carriers an easier access to shallower states. This fact, moreover, modifies their energy distribution [11]. The modification of mobility by an electric field can be modelled using a Poole-Frenkel mechanism, that describes the lowering of the thermal excitation barrier for a charge in a localized state characterized by a coulombic potential. This model provides an equation like the (1.5) [11]:

$$\mu_{PF} \propto e^{\gamma_{PF}\sqrt{E}} \quad (1.5)$$

Where  $\gamma_{PF}$  is the Poole-Frenkel temperature dependent factor.

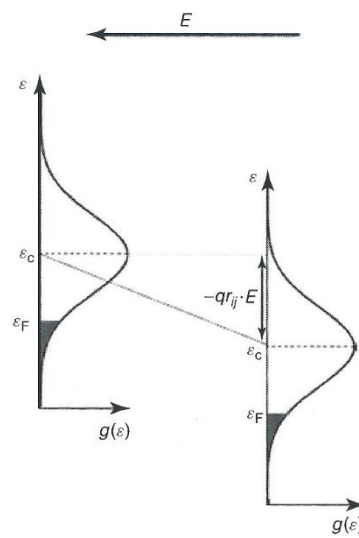


**Figure 1.4:** Hopping of a charge in presence of an electric field, that makes more states available to the charge. The shaded region represents the occupied states [11].

This  $\ln(\mu)\sim\sqrt{E}$  behaviour usually characterizes a conduction mechanism in which charge carriers must escape from charge trapping centers, but organic systems do not contain a sufficiently large number of this kind of traps, so Gartstein and Conwell [12] proposed, and showed, that for a wide range of electric fields, transport through a system in which the disorder is spatially correlated determines a Poole-Frenkel behaviour; fluctuations in the site energies caused by long-range interactions, as charge-dipole or dipole-dipole interactions with neighbouring molecules, can cause this correlation. Moreover, amorphous organic materials are characterized by a some degree of short

range order, therefore the resulting small correlations in position and conformation can increase the energetic correlation [11].

### 1.1.3. Charge injection into organic semiconductors

In addition of charge transport along the organic semiconductor, physical properties of organic devices can be strongly influenced by the metal/organic semiconductor interfaces, that can modify the amount of charge carriers injected to the channel. [7].

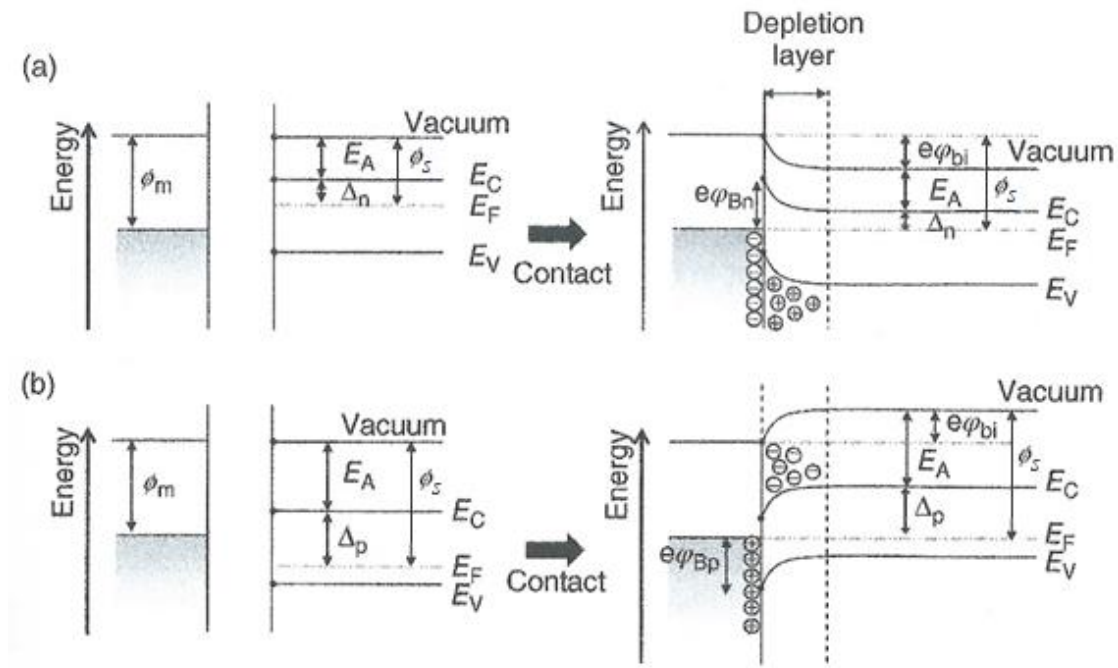


**Figure 1.5:** Metal-semiconductor interface in a n-type semiconductor (a) and in a p-type semiconductor (b) [5].

The metal inorganic semiconductor junction is called Schottky junction. In Figure 1.5a is explained the case of an ideal, neutral n-type semiconductor with valence band energy  $E_v$  and conduction band energy  $E_c$ , that is put into contact with a neutral metal of high workfunction  $\Phi_m$  ( $\Phi_s < \Phi_m$ , where  $\Phi_s$  is the semiconductor workfunction). Before the contact, the Fermi energy of n-type semiconductor is at an energy  $\Delta_n$  below the conduction band edge, characterized by an electron affinity  $E_A$ . When the contact from metal and semiconductor is made, electrons start to diffuse from semiconductor into the metal and they finish to flush when thermal equilibrium is reached, and the Fermi levels lined up. As a result, metal has additional negative charge that is lacking in the

semiconductor; this negative excess charge at the metal surface implies the collection of an equal and opposite charge in the region of the semiconductor next to the interface to form a depletion layer. The Figure 1.5 show the potential drop  $\phi_{bi}$  in the semiconductor layer adjacent to the interface, associated with a built-in field, consequently formed. At the interface, the work function of the metal, the semiconductor ionization potential (IE) and the electron affinity are unaltered with respect to the vacuum level [5]. A p-type-semiconductor metal Schottky junction has an analogous behaviour. In this case a Schottky barrier is formed when  $\Phi_s > \Phi_m$  (Figure 1.5b). When the semiconductor is organic the conduction and valence band are equivalent respectively to the LUMO and HOMO levels (Figure 1.6) [7].

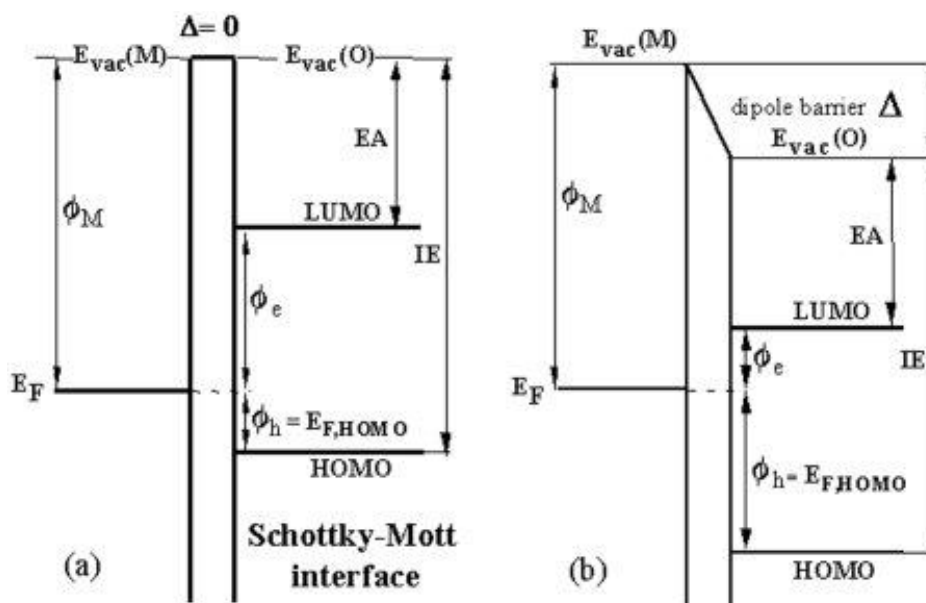


**Figure 1.6:** Metal-organic semiconductor interface: energy diagram without dipole barrier (a) and with a dipole barrier  $\Delta$  (b). IE is the ionization energy,  $E_A$  the electron affinity of the organic semiconductor,  $\Phi_e$  the electron barrier,  $\Phi_h$  the hole barriers,  $E_{vac}(O)$  the organic semiconductor vacuum level and  $E_{vac}(M)$  the metal vacuum level [13].

Gold has a relatively high work function ( $\Phi_{gold}=5.1$  eV), therefore it forms a low hole injection barrier with the most organic semiconductor, and for this reason it is used for the realization of p-type organic transistors [7].

However, several factors can modify the Mott-Schottky type of band bending, like the formation of surface dipoles [7] and traps (mostly produced during contact fabrication) [14] at the interface between the metal and the organic semiconductor.

## 1.2. Organic field effect transistors

The field effect transistor (FET) is a 3-terminal device used in several electrical circuits [15]. Organic transistors are characterized by a thin film or a single crystal made of an organic semiconductor as active layer [6]. The Organic Field Effect Transistors are in general named OFETs. When the active layer is constituted of a thin film the acronym OTFT (Organic Thin Film Transistors) is used. The organic transistor can be imagined as a plane capacitor where the gate electrode constitutes one plate and the organic semiconductor constitutes the other plate. Two other electrodes characterize the transistor: the source and the drain, that are directly in contact with the semiconductor. All these elements have a thickness largely lower than one micrometer, therefore the device is constructed on a thicker, insulating substrate, that does not contribute to the electrical behaviour of the device itself [16]. In Figure 1.7 the three more popular organic transistor geometries are depicted.

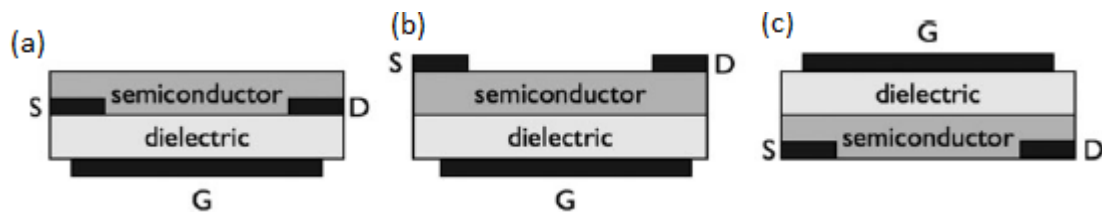


**Figure 1.7:** Organic-transistor geometries: bottom gate and bottom contacts (a), bottom gate and top contacts (b), top gate and bottom contacts (c). S indicates the source electrode, D the drain electrode and G the gate electrode [16].

The interest for OFETs and organic electronics has increased over the past few years. These devices are intensively studied for many applications such as displays, smart tags and sensors, because organic semiconductor allow to produce low cost devices on plastic substrates, potentially flexible [17], and they can be deposited over large areas, opening thus a new market segment [7].

In the OFETs, applying a voltage  $V_D$  between the source and drain, there is no intrinsic conduction, but only a flow of charges injected from the electrodes, because the density of thermally induced charge carriers is very low, especially in comparison with transistors realized with inorganic semiconductors [16].

If a gate voltage  $V_G$ , larger than the given threshold  $V_T$ , is applied, an equal amount of charge, but opposite in sign to the gate voltage, appears at both sides of the dielectric, and the conducting channel is formed. [16]. The density of charge carriers is uniform all along the channel if no voltage is applied to the drain. When a voltage  $V_D$  is applied to the drain the potential at a generic point of the channel is modified by an amount  $-V(x)$ , in a continuous way, from the source electrode ( $x=0$ ,  $V(x)=0$ ) to the drain electrode ( $x=L$ ,  $V(x)=V_D$ ), as depicted in Figure 1.8.  $L$  is the channel length.

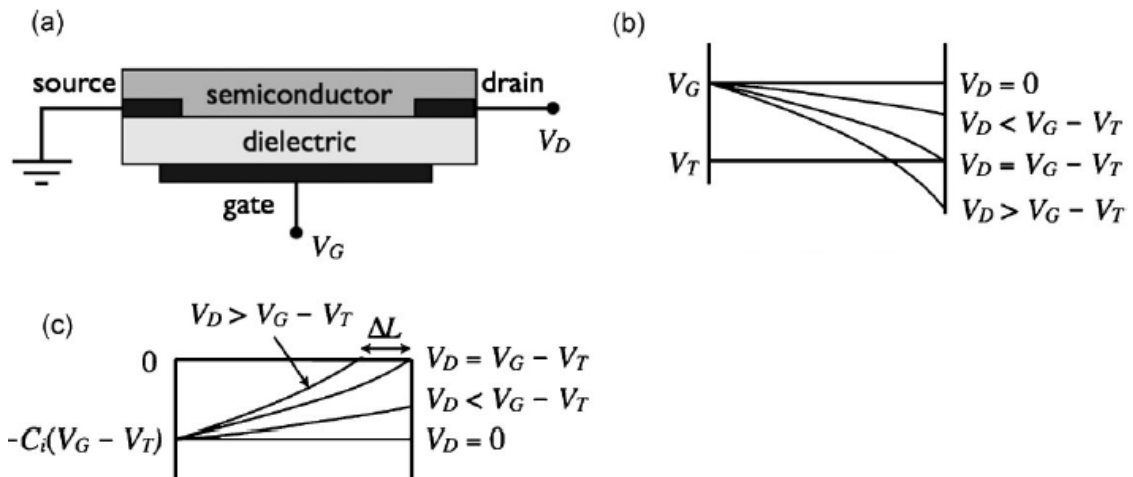


**Figure 1.8:** (a) Field-effect transistor and corresponding voltages. (b) Variation of the voltage along the channel on dependence of drain voltage  $V_D$ . (c) Variation of the charge in the conducting channel: when  $V_D=0$ , the charge is uniform, while when  $V_D=V_G-V_T$ , the charge drops to zero near the drain. When the drain voltage  $V_D$  overcomes this value a depletion zone, that is a void of charge carriers, is formed.  $\Delta L$  is the shortening of the channel. [16]

If, in addition to gate voltage  $V_G$  larger than the threshold voltage  $V_T$ , a small source drain voltage  $V_D$  (with  $V_D \ll -(V_G - V_T)$ ) is applied, the gate induced field is still almost uniformly distributed along the conducting channel. In this case the transistor is working in *linear regime*, and the current increases linearly in dependence on source drain voltage  $V_D$ . If  $V_D$  increases and becomes larger of  $V_G - V_T$  (that is  $V_D \geq (V_G - V_T)$ ), the gate field at the drain electrode is zero, and a depleted area with no induced free charge carriers is formed. This phenomenon is named pinch-off. When it is reached, the current flowing across the channel saturates, and an increase in the source drain voltage does not produce significant effects on the measured current. This regime is called *saturation regime* [7]. The saturation region and the linear region in an output characteristic are

depicted in Figure 1.9. The equations describing the OFET drain current ((1.6) for the linear regime and (1.7) for the saturation regime) are the following [11]:

$$(I_D)_{lin} = \frac{W}{L} \mu C_i \left( V_G - V_T - \frac{V_D}{2} \right) V_D \quad (\text{linear regime}) \quad (1.6)$$

$$(I_D)_{sat} = \frac{W}{2L} \mu C_i (V_G - V_T)^2 \quad (\text{saturation regime}) \quad (1.7)$$

Where  $W$  is the channel width,  $\mu$  is the field-effect mobility of the semiconductor,  $L$  the channel length and  $C_i$  the capacitance per unit area of insulator layer.

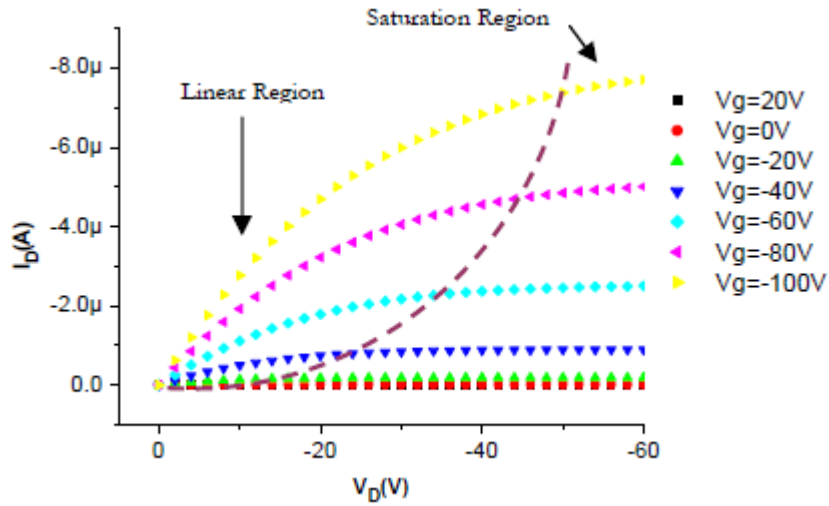


**Figure 1.9:** Output characteristic of an OFET. Linear region and saturation region are indicated [7].

Mobility, threshold voltage and  $I_{on}/I_{off}$  ratio are three parameters required for estimating the quality of an organic transistor [16]. Mobility and Threshold voltage extraction is possible rewriting equations (1.7), obtaining the equation (1.8):

$$\sqrt{(I_D)_{sat}} = \sqrt{\frac{W}{2L} C_i \mu} (V_G - V_T) \quad (1.8)$$

The plot of the square root of the saturation current against gate voltage would result in a straight line. Mobility is then obtained using the equation (1.8), knowing the slope of the straight line, whereas threshold voltage is given by the extrapolation of the line to zero current. However this method has the disadvantage that in the saturation regime the density of charge varies considerably along the conducting channel (it is maximum

near the source and practically zero at the drain, see Figure 1.8c) [16]. Moreover, the mobility in organic semiconductors depends on several parameters, among which the density of charge carriers, as a result the mobility in saturation regime is not constant along the channel, and the calculated value only represents a mean value [16].

### **1.2.1. Organic small molecule for OFETs: soluble acenes and heteroacenes**

To date acenes are one of the most intensely investigated classes of organic semiconductors; for the fabrication of OFETs especially rubrene [18] and pentacene [19] are considered benchmark materials. The best performance registered for an organic transistor has been obtained with rubrene single crystals, that demonstrated a contact-free intrinsic mobility of  $40 \text{ cm}^2/(\text{Vs})$  [20] and a maximum transistor mobility of  $18 \text{ cm}^2/(\text{Vs})$  [20]. Moreover, single crystals allow to analyze more easily the effects of defects and impurities on the device characteristics, and to get measurements of intrinsic electrical properties [21]. On the contrary, the morphological and electrical properties of thin films are strongly related to the characteristics of the substrate on which they are deposited, making them not properly suitable for these analyses. Nonetheless, thin films are the most appropriate systems for applications in large area organic electronics [16].

Nevertheless, acenes have the disadvantage of poor solubility, which significantly limits the application of solution-based deposition process for device realization [11], for this reason pentacene is substituted with trialkylsilyl acetylene, yielding thus a soluble pentacene derivatives, that, moreover, allow to reach an improvement in stability. The functionalization process produces almost exclusively  $\pi$ -stacked materials, in which changes in crystal packing induced by the substitution of the silicon are useful in tuning materials for performance in transistors (planar electrode geometries) or in photovoltaic cells (stacked electrode geometry) [11]. In transistors, molecules with two-dimensional

stacking interactions, like TIPS-Pentacene (6,13-Bis(triisopropylsilylethynyl)pentacene, Figure 1.10), perform better.

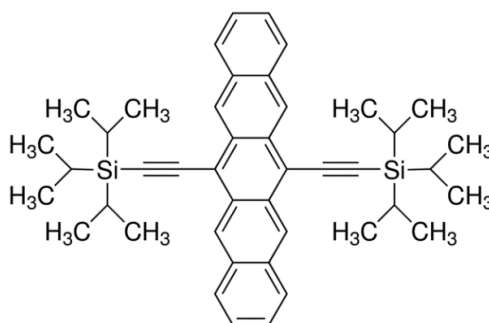


**Figure 1.10:** TIPS-Pentacene [11].

In small semiconducting molecules, charge transport is highly sensitive to intermolecular  $\pi$ -orbital overlap, and any its variations, for example induced by molecular packing, can result in variations in charge transport [22]. As already mentioned, in organic semiconductors, the dominant interactions are van der Waals and weak electrostatic (i.e. quadrupole) interactions. They are much weaker relative to ionic and covalent interactions and non-specific compared to hydrogen bonding, as a result polymorphism, defined as the ability for a compound to adopt multiple crystalline packing states, is predominant among organic molecules at near ambient conditions. Moreover, different polymorphs often have distinct physical properties such as the solubility, melting point, crystal habits, electronic, optical and mechanical properties, therefore it is important to control the polymorphism [22]. For example, in the case of TIPS-Pentacene, in thin film transistors realized by solution shearing, hole mobility was measured as  $8.1 \text{ cm}^2/(\text{Vs})$  in a nonequilibrium polymorph, whereas the equilibrium form was characterized by an hole average mobility of  $5.8 \cdot 10^{-2} \text{ cm}^2/(\text{Vs})$  [23]. A problem that may arise in the TIPS-Pentacene OTFTs is the hysteresis in the electrical characteristics. This phenomenon occurs because films formed of TIPS-Pentacene tend to consist of numerous small crystalline grains, and the boundaries between grains often fall within the channel of OTFTs devices, producing the hysteresis in the electrical characteristics. Its appearance is related to the width of the lath-shaped grains [24]: grains with width  $<4 \text{ }\mu\text{m}$  exhibit pronounced hysteresis and low mobility ( $<0.01 \text{ cm}^2/(\text{Vs})$ ) whereas grains width  $>6 \text{ }\mu\text{m}$  show minimal hysteresis and high mobility [11].

Another class of compound investigated for organic electronic applications are the silylethine-substituted heteroacenes. TES-ADT (5,11-Bis(triethylsilylethynyl)anthradithiophene) was the first molecule of this kind tested in device applications (Figure 1.11a). Nowadays TES-ADT exhibited a mobility of  $1.1 \text{ cm}^2/(\text{Vs})$  [25], measured in transistor configuration, realized by spin-coating.

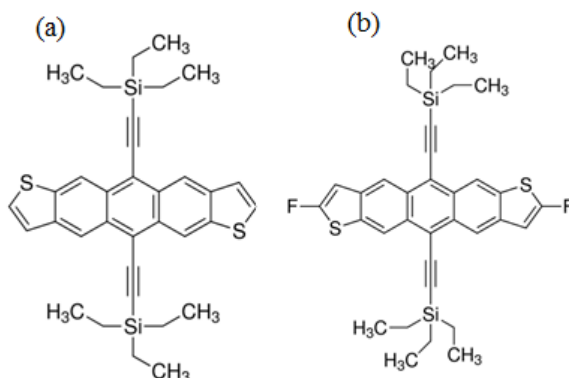


**Figure 1.11:** (a) TES-ADT (b) diF-TES-ADT [11].

Spin-coating of these materials yields, as for TIPS-Pentacene, amorphous films with very poor mobility, but the weaker interactions between molecules make this compound highly suitable to annealing techniques [11]. In order to enhance the interaction between molecules in ADTs (anthradithiophenes), partially halogenated derivatives were synthesized and analysed. Especially the fluorine-substituted derivatives, like diF-TES-ADT (2,8-difluoro-5,11-bis(triethylsilylethynyl)anthradithiophene, Figure 1.11b), proved to be particularly interesting, typically undergo rapid crystallization during film formation thanks to the improved noncovalent interactions imported by fluorine atoms. also when the deposition is realized by spin-coating [11].

An example of the use of diF-TES-ADT in transistors fabrication is reported in the paper *Azarova et al.* [26], that describes devices fabricated by spray-deposition, a simple and inexpensive method, easily scalable from laboratory-based samples to large-area electronics, that was carried out at room-temperature. Moreover, spray-deposition is more efficient than spin-coating, where, unlike spray-coating, most solution is wasted during spinning [26]. In this deposition technique the organic semiconductor solution is aerosolized under high pressure argon, and the droplets are collected on the device structure, consisting of heavily doped Silicon wafer used as substrate and gate electrode, and thermally grown  $\text{SiO}_2$  layer as the gate oxide.

The source and drain contacts of this device are made of Ti/Au, deposited by e-beam evaporation. Figure 1.12 shows the current-voltage characteristics of a transistor realized by this deposition technique, having channel length  $L=20\ \mu\text{m}$ , and channel width  $W=200\ \mu\text{m}$ . The drain current  $I_D$  increases with the negative gate-source voltage  $V_G$ , typical for a hole-transporting organic layer. The authors calculated for this device a mobility of  $0.2\ \text{cm}^2/(\text{Vs})$  and a threshold voltage of  $4.4\ \text{V}$  [26].

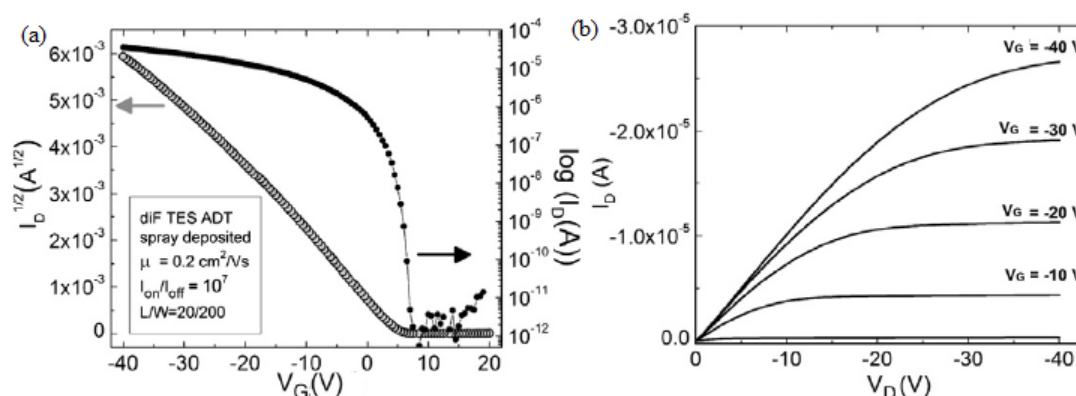


**Figure 1.12:** Electrical characteristics of a spray-deposited diF-TES ADT transistor presented in Azarova *et al.* [26] (a) Current-voltage characteristics ( $\log(I_D)$  vs.  $V_G$ ) in the saturation regime ( $V_D=-40\ \text{V}$ ). In the left axis is reported  $I_D^{1/2}$ . (b) Output characteristic. The dimensions of channel length ( $L$ ) and channel width ( $W$ ) are indicated [26].

Also in the work Rigas *et al.* [27] a spray deposition process was investigated, in order to fabricate high-quality organic single crystals based on various semiconducting small molecules on virtually any substrate. This technique, shown schematically in Figure 1.13 combines the advantages of antisolvent crystallization and solution shearing. The authors tested a variety of substrates, among which Si with native oxide, Si with a thermally grown  $230\ \text{nm}\ \text{SiO}_2$  and flexible polyethylene naphthalate. The devices, that were fabricated using top and bottom contact approach with TIPS-Pentacene OSSCs grown over the Si/SiO<sub>2</sub> substrates, produced good transistor-like behaviour, but not too high mobility values, up to  $0.4\ \text{cm}^2/(\text{Vs})$  in the linear regime, which indicates that further improvements of the this deposition technique are necessary [27].

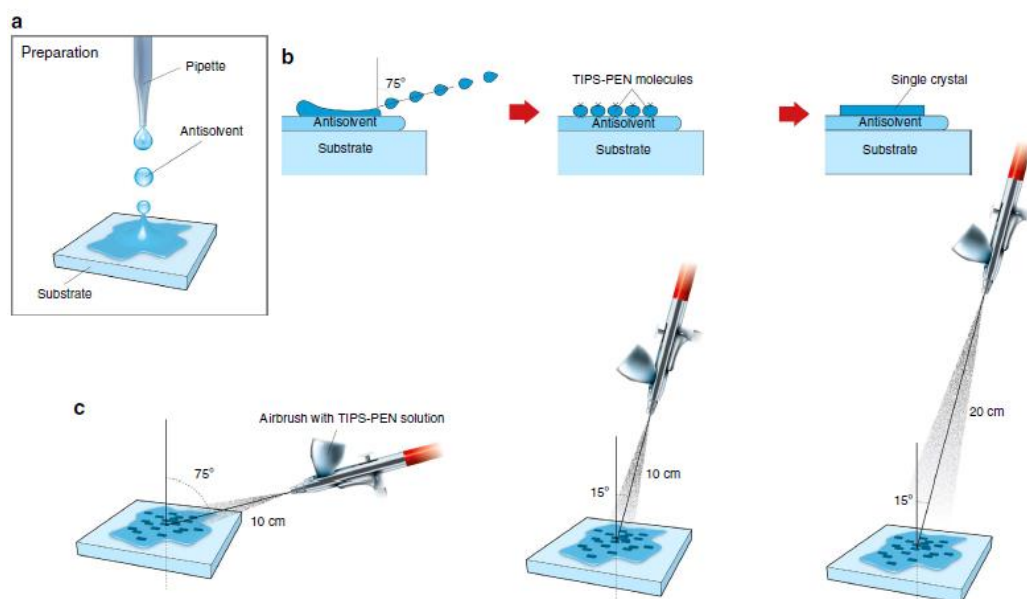


**Figure 1.13:** Schematic representation of the deposition technique showed in *Rigas et al.* [27]. (a) Deposition of antisolvent over the substrate. (b) Shearing mechanism for the droplets, generated by the airbrush, and subsequent formation of single crystals. (c) The shape and size of the crystals are influenced by airbrush position [27].

However, the best mobility for diF-TES-ADT results were obtained in *Subramanian et al* [28], depositing this molecule from solution by spin-coating, obtaining thus a mobility of  $1.5 \text{ cm}^2/(\text{Vs})$  [28].

In 2013 another heteroacenes, diF-TEG-ADT (2,8-difluorinated 5,11-bis(triethylgermylethynyl)anthradithiophene, Figure 1.14a) was used to fabricate a new type of transistor, as reported in *Mei et al.* [29]. diF-TEG-ADT is p-type (hole-transporting) semiconductive silylethine-substitued heteroacene in which Ge substitutes previously synthesized Si in diF-TES-ADT, in order to enhance molecular packing [30]. These organic field-effect transistors were fabricated by spin-coating under solvent rich atmosphere (SAC), drop-casting and spray-casting. The substrate is constituted by highly doped silicon, as gate electrode, and thermally grown  $\text{SiO}_2$  as gate dielectric, whereas the source and drain Au contacts have been defined photolithographically. The output characteristic for the device realized by drop-casting is reported in Figure 1.14b, while in Figure 1.14c is depicted the transfer characteristics in saturation regime ( $V_D = -40\text{V}$ ); for this class of devices the authors calculated a field-effect mobility  $\mu$  of  $5.4 \text{ cm}^2/(\text{Vs})$  [29]. In order to realize the devices by spin-coating, the authors dissolved diF-TEG ADT and poly(triarylamine) in tetralin and spin-casted this solution onto a

substrate with pre-patterned PFBT-treated Au source and drain electrode, and, in order to enhance the crystallization the as-spun films were annealed [29]. Finally, the authors fabricated spray-coated devices, in order to test the behaviour of diF-TEG-ADT with deposition technique applicable to large-area electronics. The mobilities for the transistors described in *Mei et al* [29] (realized by drop-casting, spin-coating and spray-casting) are reported in Table 1.1.

Material	$\mu_{\text{drop-cast}}$ ( $\text{cm}^2/(\text{Vs})$ )	$\mu_{\text{spin}}$ ( $\text{cm}^2/(\text{Vs})$ )	$\mu_{\text{spray}}$ ( $\text{cm}^2/(\text{Vs})$ )
diF-TEG-ADT	5.4	3.7	2.2

**Table 1.1:** Charge carrier mobilities of diF-TEG-ADT in devices fabricated and described in *Mei et al* [29].

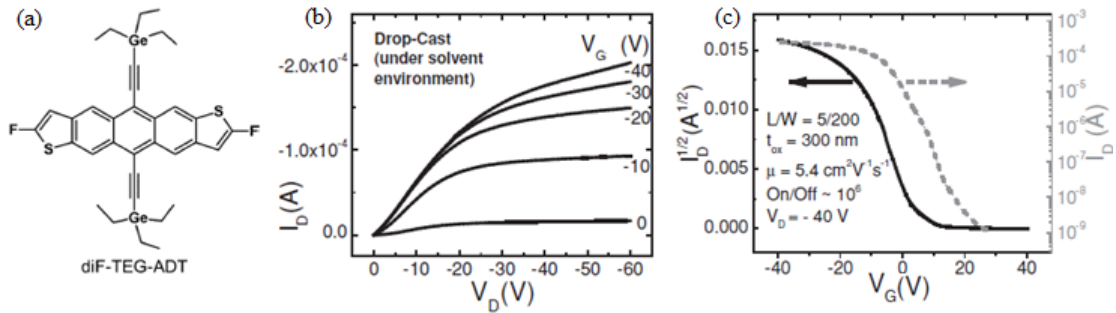


**Figure 1.14:** *Mei et al* [29]: (a) diF-TEG ADT. (b) Output and (c) transfer characteristics for a drop-casting under solvent environment device with  $L=5 \mu\text{m}$  and  $W = 200 \mu\text{m}$ . Transfer characteristic is measured in the saturation regime ( $V_D=-40 \text{ V}$ ). Right axis represents  $\log(I_D)$  vs  $V_G$ , while left axis represents  $I_D^{1/2}$  vs  $V_G$  [29].

Also the reference *Kim et al.* [30] presents a kind of device realized by spin-coating of a diF-TEG-ADT solution over a  $\text{SiO}_2$  substrate. Before the deposition the authors modified the Au source/drain electrodes by self-assembled monolayers (SAMs) of pentafluorobenzenethiol (PFBT) because of favoured nucleation through F-F, S-F reaction and of enhanced hole injection [30]. Electrical characterization of one of these diF-TEG-ADT OFET is depicted in Figure 1.15a. Transfer characteristics of these devices shows typical p-type field-effect behaviour, and the  $I_{\text{on}}/I_{\text{off}}$  ratio is high, in the order of  $10^6$ . In Figure 1.15b, the substantial increase in  $\mu$  with  $|V_G - V_T|$  indicates that the charge transport is affected by trap states and/or intrinsic disorder, that the authors mainly attributed to the grain boundaries shown in Figure 1.15c. The authors preferred,

to extract mobility, use the transmission-line method (TLM), that provides an indication of the intrinsic properties, instead of the saturation-regime square-root  $I_D$  method that has some limitations. The value of  $\mu$  has been calculated as  $0.3 \text{ cm}^2/(\text{Vs})$  [30].

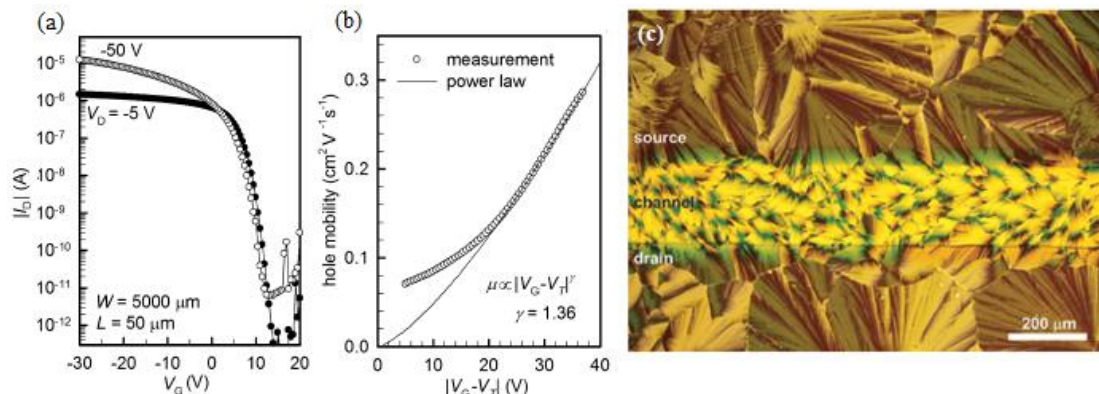


**Figure 1.15:** Kim *et al.* (a) Transfer characteristics of a diF-TEG-ADT OFET.  $W$  indicates the channel width, and  $L$  the channel length. (b)  $V_G$ -dependent hole mobility extracted from the TLM analysis. The solid line is the power-law mobility drawn for comparison. (c) Polarized optical microscope image over a large area, that covers the transistor channel and the adjacent SAM-treated Au electrode regions. [30]

Another interesting deposition technique applied to TIPS-Pentacene, diF-TES-ADT, 2,7-C8-BTBT (dioctyl[1]benzothieno[3,2-b][1]benzothiophene), and DT-TTF (dithiophene-tetrathiafulvalene), was presented in 2016 in *Terminiño et al.* [31]. This process, named BAMS (bar-assisted meniscus shearing, Figure 1.16), starts with the preparation of solutions of the mentioned semiconductors with PS (Polystyrene) in chlorobenzene. Subsequently a smooth cylindrical bar positioned  $\approx 300 \mu\text{m}$  above cleaned Si/SiO<sub>2</sub> substrates with prefabricated gold electrodes, is employed to cast the film. In particular a certain volume of the blend solution is deposited between the bar and the substrate, thus a confined meniscus is formed. Then the solution is sheared, therefore the meniscus is displaced, and by convective self-assembly a thin film is formed. This procedure contemplates its realization under ambient conditions. In order to remove any solvent traces, after solution casting the devices are left under vacuum for a certain period of time [32].

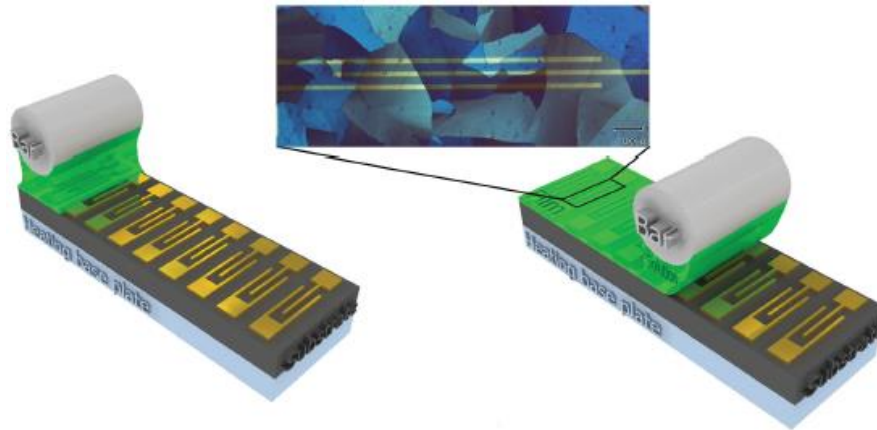


**Figure 1.16:** Illustration of the BAMS deposition technique. The inset shows an optical polarized microscopy image exhibiting the formation of large crystalline domains [32].

The polarized optical microscopy images of the films prepared during the work presented in *Termino et al* [31] show uniform crystalline domains (Figure 1.17). In particular, TIPS-Pentacene, diF-TES-ADT, and C8-BTBT form spherulitic films with no preferential orientation while, DT-TTF films, on the contrary, are formed by long domains (several millimeter) grown along the shearing direction. Moreover, the sample characterization by X-ray powder diffraction, indicates an high degree of crystallinity [31].

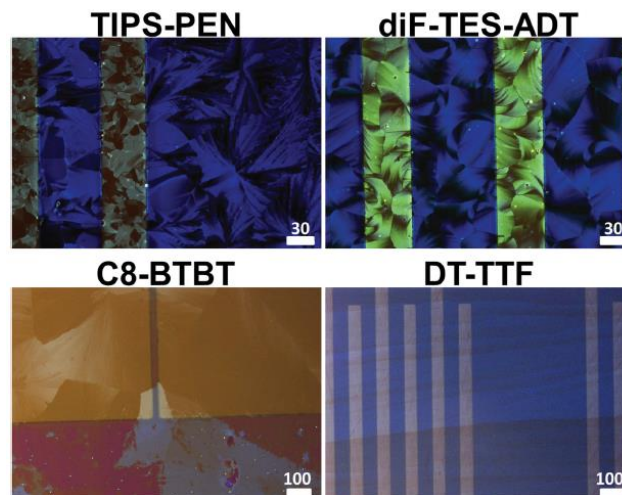


**Figure 1.17:** *Termino et al* [31]: Optical polarized microscopy images of thin films of the four organic semiconductors.

The authors characterized these devices electrically under ambient conditions. Their output characteristics are shown in Figure 1.18. TIPS-Pentacene devices exhibited a

small hysteresis between the forward and reverse gate voltage and drain voltage ( $V_D$ ), however these transistors are characterized by a low average threshold voltage ( $V_T = -0.9V$ ) and a high average field-effect mobility ( $\mu = 1.6 \text{ cm}^2/(Vs)$ ), extracted in saturation regime. Similar values are exhibited by diF-TES-ADT based devices:  $\mu = 1.3 \text{ cm}^2/(Vs)$  and  $V_T = +0.8 V$ . C8-BTBT transistors showed instead an average field-effect mobility of  $0.26 \text{ cm}^2/(Vs)$  and an average threshold voltage of  $V_T = -29 V$ . Finally, DT-TTF based devices are characterized by an average field-effect mobility of  $0.13 \text{ cm}^2/(Vs)$ , and  $+3.9 V$  as average threshold voltage.

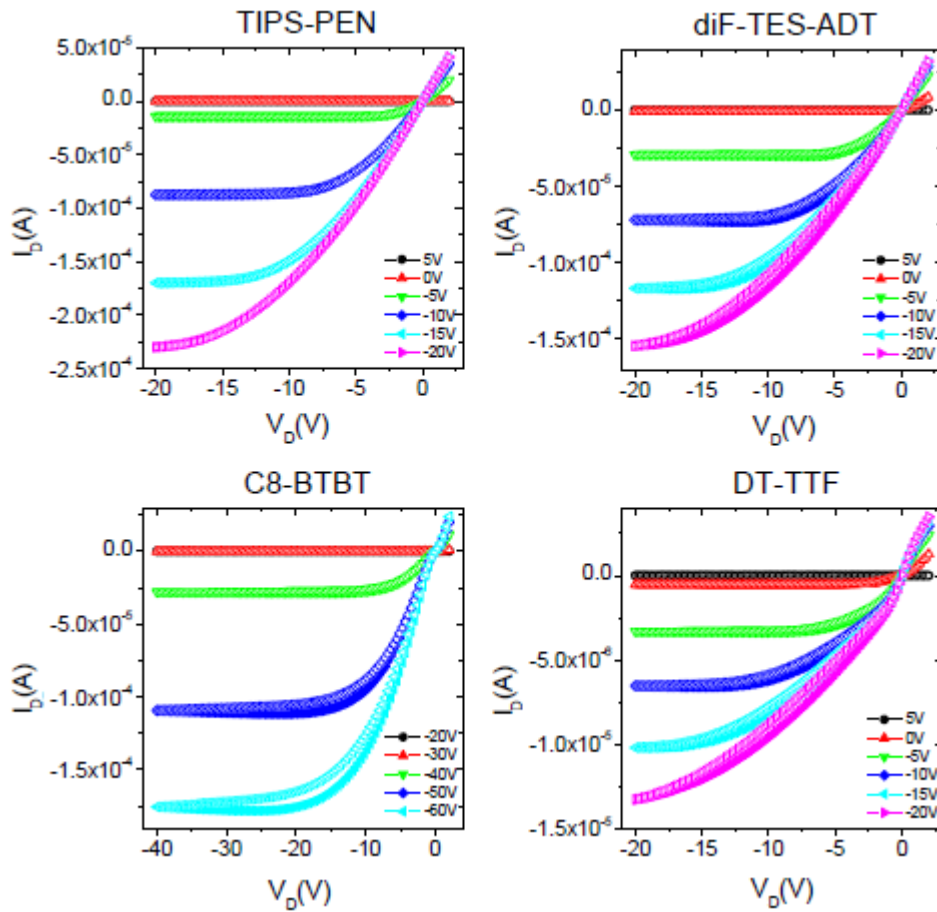


**Figure 1.18:** *Terminiño et al*: Output characteristics of typical devices fabricated with TIPS-PEN, diF-TES-ADT, C8-BTBT and DT-TTF films by BAMS deposition technique.  $I_D$  is the drain current and the voltage indicated in the plots are the  $V_G$  voltage at which the device was polarized [31].

Another example of OTFT, realized by drop-casting, mainly for direct detection of X-rays, was reported in the article *Lai et al.* [33], and it is presented in the following chapter in detail, since it is the device structure employed in the present work.

## 2. Ionizing radiation detection

Any ionizing radiation detector operates in a manner determined by the way in which the radiation that have to be detected interacts with the material of the detector. The four major categories of ionizing radiation are [34]:

-Heavy charged particles (charged particulate radiations)

-Fast electrons (charged particulate radiations)

-Neutrons (uncharged radiation)

-X-rays and  $\gamma$ -rays (uncharged radiations)

The charged particulate radiations continuously interact through the Coulomb force with the electrons present in any medium which they cross. The uncharged radiations, or indirectly ionizing radiations, on the contrary, are not subjects to the Coulomb force, but they must first undergo an interaction, often involving the nucleus of constituent atoms, that in a single encounter radically changes the properties of incident radiation. In all cases of practical interest, this kind of interaction determines the partial or full transfer of energy of the incident radiation to charged particle products of nuclear reactions, or to the electrons or the nuclei belonging to the constituent atoms. The interaction may not occur within the detector; in this case these radiations pass through the detector volume and they are not detected [34].

X and  $\gamma$ -rays can transfer all or part of its energy to electrons within the medium through several processes, among which, the three most important are described in the following paragraphs. On the contrary, the neutrons involved in an interaction may produce a secondary heavy charged particle, which then serves as the basis of an eventual detector signal [34].

## 2.1. Ionizing radiation interaction with matter

A large number of interaction mechanisms are known for X-rays and  $\gamma$ -rays in matter, but only three major types have an important role in radiation measurements. They are *photoelectric absorption*, *Compton scattering* and *pair production* [10]. These interactions, that have energy-dependent occurrence probability, lead to the partial or complete transfer of the incident photon energy to the electron energy. As a consequence of one of these interactions, the photon may be scattered through a significant angle or may disappear entirely [34].

### 2.1.1. Photoelectric absorption

In the photoelectric absorption process a photon has an interaction with an absorber atom. As a result of this interaction the photon completely disappears and a photoelectron having energy  $E_e$  is ejected by one of the bound shells of the absorber atom.  $E_e$  is given by the equation (2.1) [34]:

$$E_e = h\nu - E_b \quad (2.1)$$

Where  $h$  is the Planck constant,  $\nu$  the frequency of the incident photon and  $E_b$  the binding energy of the photoelectron. After the interaction, the absorber atom has a vacancy in one of its bound shells, that is can be quickly filled by means of the capture of a free electron from the medium and/or rearrangement of electron belonging to the other shells of the atom. As a result of these processes, one or more characteristic X-rays may also be generated. These X-rays are in most cases reabsorbed close to the original site through the photoelectric absorption, but they can also migrate and escape from detector, thus influencing its response. The photoelectric absorption process is predominant for  $\gamma$ -rays and X-rays of relatively low energy and for absorber materials of high atomic number  $Z$ . For this reason there is a preponderance of high  $Z$  materials in  $\gamma$ -ray and X-ray shields [34]. A single analytic expression for the probability of photoelectric absorption per atom  $\tau_{ph}$  over all ranges of  $E_{ph}$  and  $Z$  does not exist, but a rough approximation is given by the equation (2.2) [34]:

$$\tau_{\text{ph}} = \text{constant} \times \frac{Z^n}{E_{\text{ph}}^{3.5}} \quad (2.2)$$

Where  $Z$  is the atomic number and  $E_{\text{ph}}$  the incident photon energy.

Over the photon energy region of interest, the exponent  $n$  varies between 4 and 5. As indicated by the equation (2.2), the probability of photoelectric absorption is strongly  $Z$  dependent. Finally, the photoelectric absorption plays the main role in the mechanism of absorption occurring in X-ray detectors for diagnostic, medical or imaging applications [10].

### 2.1.2. Compton scattering

The interaction process known as Compton scattering occurs between a photon incident over an absorbing material and an electron belonging to the absorbing material itself. In this process, shown in Figure 2.1, the incoming photon transfers a portion of its energy to the *recoil* electron, and it is deflected through an angle  $\theta$  with respect to its original direction. The energy transferred from the photon to the electron can vary from zero to a large fraction of the  $\gamma$ -ray energy, because all angles of scattering are possible, even if they are not equally probable. It is possible to derive the analytical expression (2.3) that relates the energy transfer and the scattering angle simply by writing simultaneous equations for the conservations of momentum and energy. Using the symbols defined in Figure 2.1 it can be write as [34]:

$$h\nu' = \frac{h\nu}{1 + \frac{h\nu}{m_0c^2(1-\cos\theta)}} \quad (2.3)$$

Where  $m_0c^2$  indicates the rest-mass energy of electron (0.511 MeV).

The probability of Compton scattering per atom is a function of the number of electrons available as scattering targets, and it increases linearly with  $Z$ . Finally, the angular distribution of scattered  $\gamma$ -rays is given by the *Klein-Nishina-formula* [34].

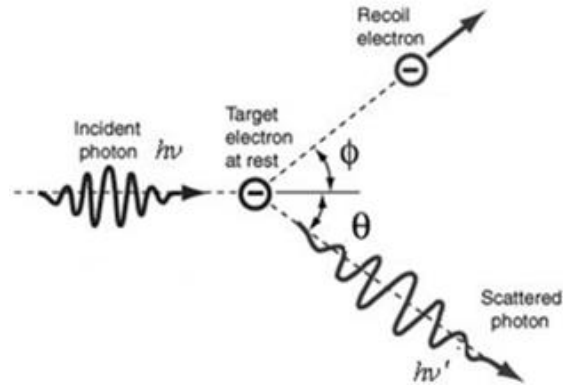


**Figure 2.1:** Compton effect [34].

### 2.1.3. Pair Production

Pair production is possible if the  $\gamma$ -ray exceeds twice the rest-mass energy of the electron. In this absorption process, the incident photon disappears, and it is replaced by a positron-electron pair. If the impinging photon has an energy larger of 1.02 MeV, that is the energy required to create the pair, its excess energy goes into kinetic energy of the positron and of the electron. After the pair production, the positron annihilates, and then two annihilations photons, that have an important effect on the response of  $\gamma$ -ray detectors, are normally produced as secondary products of interaction. As already mentioned above, the process of pair production is energetically possible if the  $\gamma$ -ray exceed twice the rest-mass energy of the electron, but its probability remains very low until the photon energy is close to several MeV, therefore pair production is mainly confined to high energy  $\gamma$ -rays [34]. The magnitude of the probability of pair productions per nucleus varies approximately as the square of the atomic number-Z. However, no simple expression that describe the probability of this process exists. The Figure 2.2 reports the plot of the relative importance of the three processes described, for different absorber materials and photon energies.

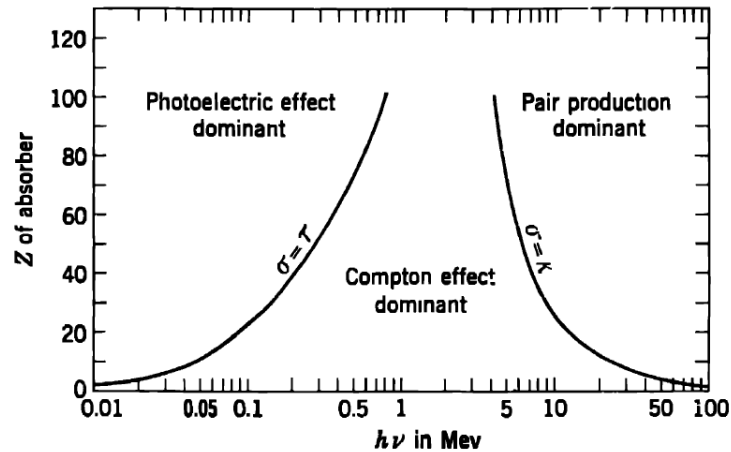


**Figure 2.2:** Relative importance of the three major types of  $\gamma$ -ray and X-ray interaction described in this chapter. The lines indicate the limits in which the adjacent effects have equal probability [35].

## 2.2. Simplified detector model

It is possible to describe a simplified model for a generic detector in which a single particle or quantum radiation undergoes an interaction through one of the mechanisms discussed in the previous paragraphs [34].

In almost all detectors, the net result of the radiation interaction is the appearance of a given amount of electric charge within the detector active volume. This simplified model assumes that a charge  $Q$  appears within the detector at time  $t=0$  s as a result of the interaction of a single particle or quantum of radiation. Then, this charge  $Q$  must be collected in order to form the basic electrical signal. Often, an electric field within the detector is applied to induce the charges created by the radiation to flow at the opposite directions. The time required to collect the charge is different for each detector type, and it depends on the mobility of the charge carriers within the detector active volume and on the average distance that the charge carriers travel to arrive at the collection electrodes. For example, in ion chambers the collection time can reach few milliseconds, whereas in detectors based on semiconductor diodes its value is of a few nanoseconds. The charge  $Q$ , generated in a specific interaction is simply equal to the time integral over the duration of the current described by the equation (2.4) [34]:

$$\int_0^{t_c} I(t) dt = Q \quad (2.4)$$

Where  $t_c$  is the charge collection time. The Figure 2.3 presents one example for the time dependence of the current [34].

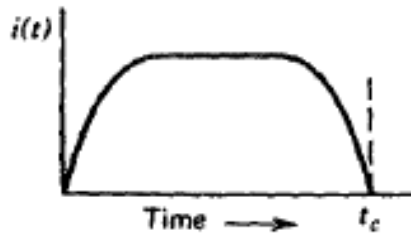


**Figure 2.3:** time dependence for the detector current [34].

This simplified model contemplates that only one interaction happens at given time, but in any real situation many quanta of radiation will interact over a period of time [34].

Radiation detectors can work in three general modes of operation: pulse mode, current mode and mean square voltage mode. Pulse mode is particularly useful to record each individual quantum of radiation that interacts in the detector. Since the energy deposited in the detector is directly related to  $Q$ , normally the time integral of each burst of current or the total charge  $Q$  is recorded. A sequence of current bursts is depicted in Figure 2.4. All the detectors that have to measure the energy of individual radiation operate in pulse mode [34].

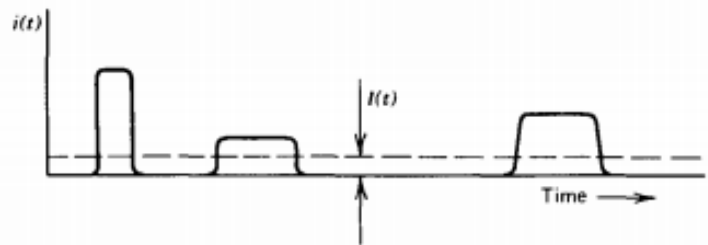


**Figure 2.4:** Recorded signal by a current-measuring device, during a sequence of events [34].

In current mode, the measuring device has a fixed response time  $T$ . Therefore, the recorded signal from a sequence of events is a time dependent current given by the equation (2.5):

$$I(t) = \frac{1}{T} \int_{t-T}^t I(t') dt' \quad (2.5)$$

The response time  $T$  is typically long compared with the average time that separates the current pulses generated by the incident radiation. Therefore, the detector averages many of the fluctuations in the intervals between individual radiations interactions and it records an average current that depends on the product of the charge per interaction and the interaction rate. In current mode this time average of the individual current bursts is the basic signal [34]. Finally, in the mean square voltage mode of operation the mean square signal, proportional to the square of the charge  $Q$  produced in each event, is recorded. This mode of operation is most useful when the measurements are carried out in mixed radiation environments, in which the charge produced by one type of radiation is very different than the one produced by the second type [34].

### **2.3. Detection of X-rays and $\gamma$ -rays**

Two different categories of functional materials are used to detect the high energy photons (X-rays and  $\gamma$ -rays): scintillators and semiconductors. In both type of detectors, the high-energy photon causes primary excitations and ionization processes, which, interacting at a second stage within the active volume of the detector, produce electron-hole pairs (excitons) that are transduced into an output signal. This final operation occurs following different pathways in scintillator and semiconductor-based detectors [36]. In a scintillator, the excitons transfer their energy to luminescent centers, often intentionally introduced, that then release this energy radiatively. The resulting photons, typically in the visible wavelength range, are collected by a photodiode or a coupled photo-multiplier tube (PMT), which provide an electrical signal dependent on the incident radiation beam [36]. The visible photons emitted from the scintillator propagates isotropically from the point of generation, thus determining optical crosstalk between pixels in flat-panel detectors, which limits the optical resolution. The resolution in flat-panel detectors is determined by the Modulation Transfer Function (MTF), which, for a given spatial frequency, evaluates the detector ability to transfer the input signal modulation in relation to its output. [37].

In a semiconductor detector, in order to dissociate the electron-hole pairs and to sweep the holes and electrons to the negative and positive electrodes respectively, an electric

field is applied. Then, the resulting photocurrent is recorded as the signal associated to the high-energy radiation particles. The direct conversion of ionizing radiation into an electrical signal within the same material, that characterizes the semiconductor-based detectors, allows to achieve better signal-to-noise ratios and device responses time, in comparison with the indirect detection. The both types of detectors require materials characterized by high purity, to minimize exciton trapping, high stopping power, to achieve a high absorption efficiency of the incident radiation, good transparency and good uniformity, in order to reduce scattering. Moreover, the ability to grow these materials into a large size, that allows to increase the interaction volume, constitutes an advantage [36]. A good semiconductor used for detections, is also characterized by [36]:

- High resistivity ( $>10^9 \Omega \cdot \text{cm}$ ) and low leakage current. It is possible to achieve the necessary high resistivity with high band-gap ( $>1.5 \text{ eV}$ ) and low intrinsic carrier concentration.
- A small enough band-gap ( $<5 \text{ eV}$ ), in order to have a small electron-hole ionization energy. In this way, the number of electron-hole pairs generated is reasonable large and therefore the signal-to-noise ratio is low.
- High atomic number  $Z$  and large interaction volume, in order to obtain an efficient radiation-atomic interaction.
- High intrinsic  $\mu\tau$  product, where  $\mu$  is the carrier mobility and  $\tau$  is carrier lifetime.
- Electrodes must not produce defects, impurities or barriers to the charge collection process, and they must apply a uniform electric field trough the device, in order to avoid material polarization effects, which may have effect on the time response of the detector.
- Surfaces must be highly resistive and stable over time, in order to avoid increases in the surface leakage currents that may occur over the lifetime of the detector.

## 2.4. Organic direct ionizing radiation detectors

The first studies about organic direct ionizing radiation detectors started in 2007, with conjugated-polymer-based thin film devices [1]. To date, a good number of direct detectors based on organic semiconductors have been reported. They are based on thin films and single crystal of small molecule, and on organic semiconducting polymers [13] [29] [32] [35]. A description of these works is reports in the following paragraphs. A disadvantage of semiconducting polymers is given by the fact that many polymer-based direct detectors use the measurement of the resistivity (conductivity) of the polymeric semiconductor to evaluate the radiation intensity, which increases (decreases) upon device exposure to the ionizing radiation, in dependence of material degradation. Therefore these devices cannot perform for prolonged periods, and consequently are characterized by a very short operative lifetime [36].

However, as already mentioned in the previous chapter, organic  $\pi$ -conjugated small molecules and polymers are interesting emerging novel material, because they can be deposited by low-cost methods, also at room temperature and over large areas [36].

### 2.4.1. Organic Direct Detectors based on Thin Films

A result about flexible detector based on TIPS-Pentacene deposited by drop-casting over an interdigitated structure (Figure 2.5a), and operating at low bias voltage is reported in the article *Basiricò et al.* [17]. In Figure 2.5 the photocurrent response of this device to the irradiation is depicted. The authors retained that the photocurrent simply due to the charge collection,  $I_{cc}$ , would be  $<2$  pA, because of the low photon absorption of the organic semiconductor. The acquired photocurrent, nevertheless, is about two orders of magnitude bigger (Figure 2.5b), therefore other processes are involved in the generation of such a large photocurrent.

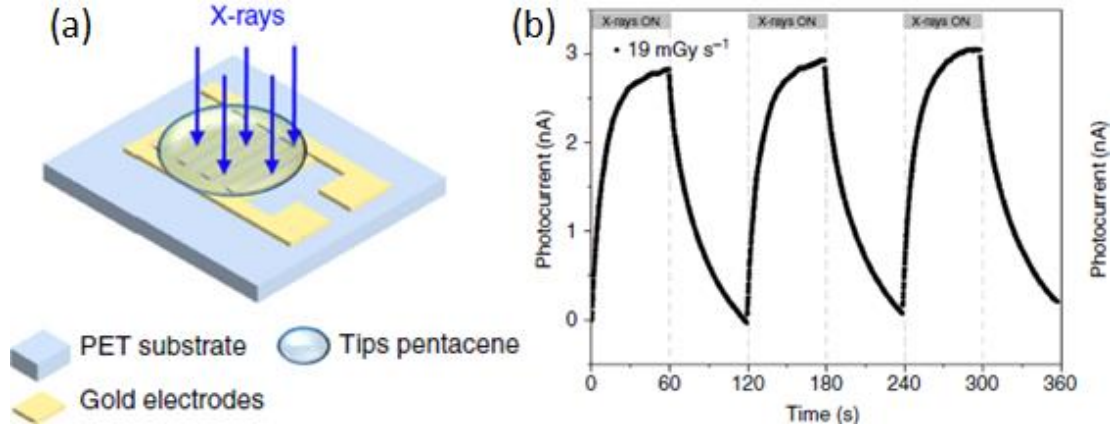


**Figure 2.5:** *Basiricò et al.* (a) Schematic view of the device. The interdigitated structure is clearly visible (b) X-ray-induced photocurrent signal of TIPS-Pentacene based detector, polarized at 0.2 V, upon three on/off cycles of a monochromatic synchrotron X-ray beam at 17 keV [17].

The authors ascribe this increase in conductivity to a photoconductive gain, that arises because X-rays generate electron-hole pairs. Electrons remain trapped at the native defects (electron traps) while holes are collected by the electrodes. To maintain charge neutrality in the material multiple holes are emitted to compensate the trapped negative charge, thus enhancing the collected current signal. The amplified photocurrent, given by the photoconductive gain is describe by the equation (2.6):

$$\Delta I_{PG} = G I_{CC} \quad (2.6)$$

where  $G$  is the photoconductive gain [38].

In the context of this work the authors measured hole mobility in TIPS-pentacene OTFT, before and during an X-rays irradiation, and they observed that it exhibited no significant differences [17], consequently they propose that when this kind of device is exposed to an X-ray beam, additional free carriers are generated and accumulate in the organic thin film. The gold electrodes of this detectors form ohmic contacts with TIPS-Pentacene (the work function of gold,  $\phi_{Au} = (4.7 \div 5.2)$  eV [39], is generally considered matching to HOMO level of TIPS-pentacene that is 5.3 eV [40]), then an increase in carrier concentration  $\rho_x$  determines an increase of current  $\Delta I_{PG}$ , described by the equation (2.7) [17]:

$$\Delta I_{PG} = W h \rho_x \mu E \quad (2.7)$$

Where  $E$  is the electric field and  $W$  the active width of the interdigitated structure [41]. Differences in hole and electron transport in organic materials [42] are useful to derive a model for the increase in free carriers and its impact on X-ray induced photocurrent. This difference can arise from a difference in the charge carrier mobility between electrons and holes or from the presence of traps for one of the two type of charge carriers. In TIPS-Pentacene, hole mobility reaches very high values [19]. On the contrary, electrons are trapped very easily when a polar substrate, like PET [43], is employed and in presence of oxygen [44] [45], that characterizes the measurements carried out in ambient conditions, as in this case. The hypothesis of the authors is therefore that the X-ray generated electrons remain trapped and act as “doping centres”, while the X-ray generated holes drift along the electric field until they reach the collecting electrode. Mobile holes are then continuously re-injected from the injecting electrode, to guarantee charge neutrality. As a result, for each electron-hole pair created more than one hole contributes to the photocurrent, and this fact, that is a sort of “doping” process, leads ultimately to a photoconductive gain [17].

In order to model the experimental saw-tooth shape of the X-ray induced photocurrent, due to an on/off switching X-ray beam (Figure 2.5b), the authors considered the variation of photo-generated carrier concentration  $\rho_x$  in time given by (2.8):

$$\frac{\partial \rho_x(t)}{\partial t} = \frac{\phi n q}{A h} - \frac{\rho_x(t)}{\tau_r(\rho_x)} \quad (2.8)$$

The first term in equation (2.8) describes the accumulation of carriers, while the second one describes the recombination of carriers and contains the free carrier lifetime  $\tau_r(\rho_x)$ , that in this paper is approximated by the phenomenological equation (2.9):

$$\tau_r(\rho_x) = \frac{\alpha}{\gamma} \left[ \alpha \ln \left( \frac{\rho_0}{\rho_x} \right) \right]^{\frac{1-\gamma}{\gamma}} \quad (2.9)$$

Where  $\alpha$ ,  $\gamma$  and  $\rho_0$  are material-specific constants that describe respectively the characteristic time-scale, the dispersion of trap states, and a reference carrier density. Equation (2.9) models satisfactorily the observed stretched exponential recovery after exposure, while the combined of equations (2.8) and (2.9) fully describe the dynamics of carrier photogeneration and recombination, and the emerging photocurrent during and after X-ray exposure (Figure 2.7a). Experimentally, the sensitivity was determined

differentiating the photocurrent data in function of dose rate. Its highest found value is 180 nC/Gy ( $72000 \text{ nC/mGy/cm}^{-3}$ ), obtained for low dose-rates and long exposure times. The model reported above allows also to describe the dose rate dependence of the photocurrent, which determines the detector sensitivity, and is in excellent agreement with the results presented in the paper [17].

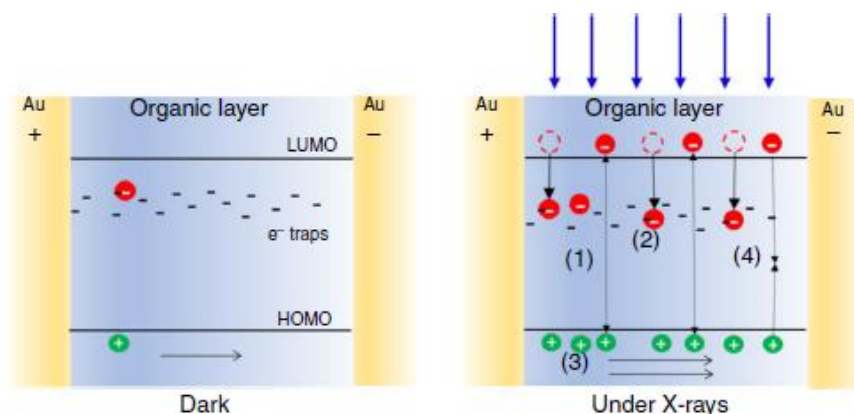


**Figure 2.6:** *Basiricò et al* [17]. Modulation of the conductivity induced by X-rays in TIPS-Pentacene thin films. (Left) When the device is not exposed to X-rays the conductivity is due to the intrinsic carriers. (Right) (1) Under X-ray irradiation additional holes and electrons are generated. After generation, holes drift along the electric field until they reach the collecting electrode. (2) On the contrary, the electrons remain trapped in deep trap states within the organic material. (3) Holes are continuously emitted from the injecting electrode to maintain the charge neutrality. (4) Recombination process, that counterbalances the charge photogeneration in the steady-state [17].

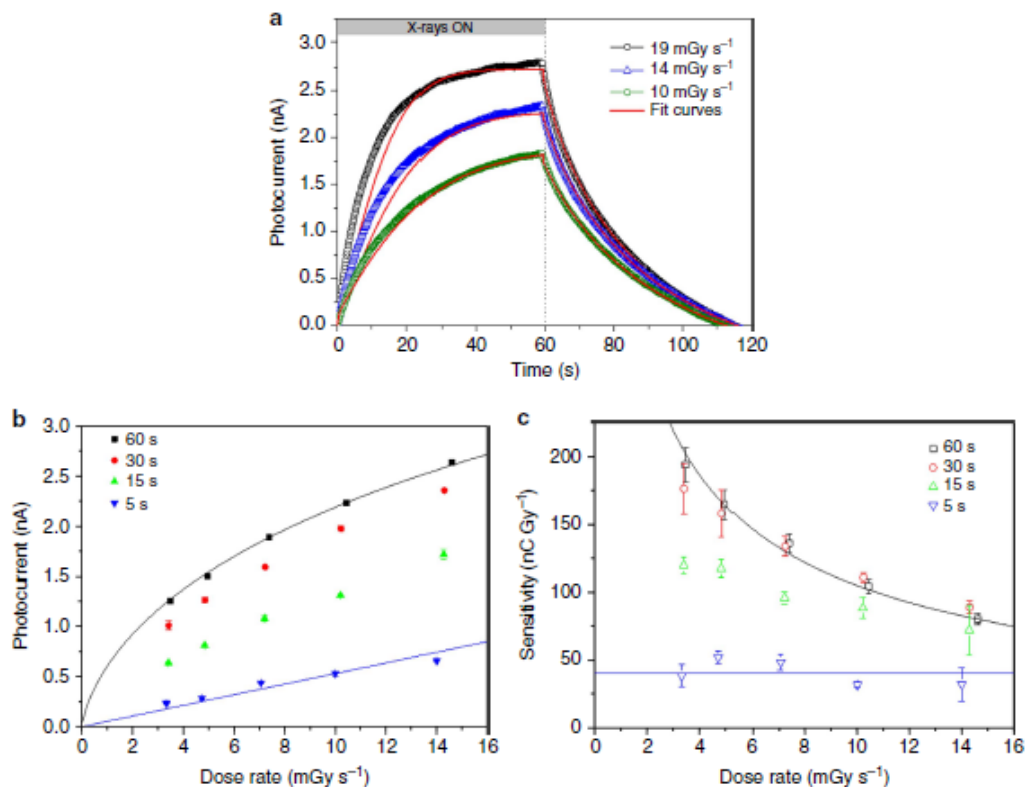


**Figure 2.7:** *Basiricò et al.* [17]. (a) Dynamic response of the detector under three different dose rates of radiation: experimental and simulated curves. The device was exposed for 60 s to a synchrotron 17 keV X-ray beam, and polarized at 0.2 V. (b) Photocurrent versus Dose rate plot (scattered points) recorded for different exposure times at the previous conditions. (c) Sensitivity values, calculated differentiating the photocurrent data in function of dose rate, versus dose rate, for different time exposures to the radiation. The solid lines drawn in these plots is the fit of the data, according to the analytical model described above. [17].

The authors evaluated also the mechanical flexibility of the system, characterizing the detectors in a bent configuration with a bending radius of 0.3 cm, that is conformable to the human body curves. The X-ray induced photocurrent was acquired before bending, during bending and after bending, with the substrate restored to a flat conformation. The measurement performed during the first bending evidenced a drop of the X-ray-induced photocurrent of about 50%. On the contrary, between following repetitive measurements on bent and relaxed devices, no significant differences in photocurrent are noticed. Finally, the authors realized an X-ray detection system based on a 2x2 pixelated matrix of organic thin film. The measurements carried out on this device indicate good discrimination between pixels when they are selectively irradiated, making possible the employment of this device for imaging application [17].

TIPS-Pentacene was also the base for a novel type of direct thin film detector based on organic transistor, presented in 2017 in *Lai et al* [33]. The main advantage of this type of sensor is the possibility of tune detection ability acting on the transistor polarization conditions. Moreover, it is possible to integrate the transistor-based sensors in electronic systems, like amplifiers and logic stages, which provide an easy readout of the signals. [33]. Typically, the OFET-based ionizing radiation detectors have relatively high biasing voltages (about a few tens of volts), that limited their development, but the device presented in *Lai et al.* [33] overcomes this restriction, becoming the first X-ray direct detector based on a low voltage OFET fabricated on a flexible plastic substrate. The transistor structure, based on 175  $\mu\text{m}$  thick, biaxially oriented polyethylene terephthalate (PET) substrate, is explained on detail in the chapter 3, because it is the same used in this work. The semiconductor layer is a polycrystalline film of TIPS-Pentacene, deposited by drop-casting from a solution in toluene, having concentration of wt.0.5% [33]. In Figure 2.8 a typical output and a typical transfer characteristic curves obtained in *Lai et al* [33] are depicted; they show that the ideal device features, such as significant field-effect modulation, good current saturation, and negligible contact resistance effect are obtained. Moreover, it is noteworthy that drain-to-source and gate-to-source voltages are in the range of 3V, indicating thus that this transistor can work at low voltage. Anyway, a hysteresis and a leakage current are present in the transfer characteristics, but they are very low (the leakage current is about a tens of pA). Finally, the authors calculated mobility values up to  $0.1 \text{ cm}^2/(\text{Vs})$  and a threshold voltage of  $0.4\text{V}$  [33].

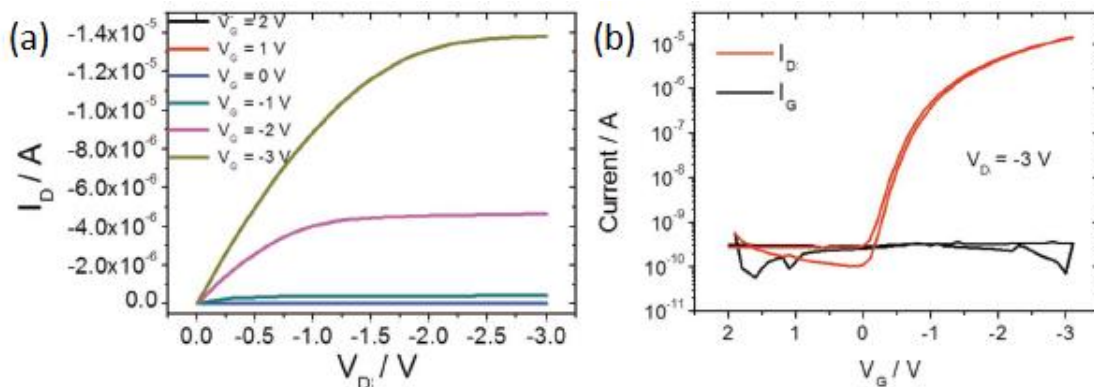


**Figure 2.8:** (a) Typical output and (b) transfer characteristic curves of the devices presented in *Lai et al.* [33].

Real-time responses of the device, in terms of drain-to-source current ( $I_D$ ) variation, under X-ray beams having different dose rates, are reported in Figure 2.9a and b, in linear regime ( $V_D = -0.25$  V,  $V_G = -2$  V), and in saturation regime ( $V_D = -4$  V,  $V_G = -2$  V), respectively.

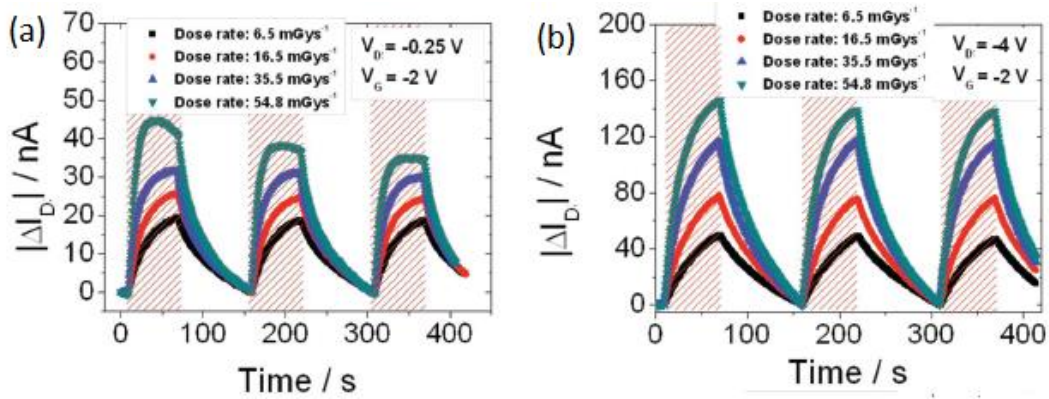


**Figure 2.9:** Typical response of the low voltage transistor presented in *Lai et al.*[33] to different dose rates in (a) linear and (b) saturation regimes, as variation in the drain-to-source current. In both cases, the device was subjected to three X-ray consecutive exposures, each one with a duration of 60 s (highlighted by the red-dashed rectangles) [33].

For both operating regimes, the output current increases with the applied dose-rate for tens of seconds, and the same slow dynamic occurs for the relaxation after X-ray exposure. The device response to X-rays is characterized by similar amplitude and dynamics for each subsequent exposure, and therefore by a good reproducibility. On the contrary, the maximum current variation is generally lower in linear regime. A small variation of the leakage current under X-rays, negligible with respect to  $I_D$  variations (respectively few tens of pA and up to 140 nA for 54.8 mGy/s dose rate exposure) is, observed and it can be explained with the photoemission at the aluminium gate electrode [33]. Indeed, the X-rays can easily pass through both TIPS-pentacene and Parylene C layers, characterized by a low X-ray absorbance typical of organic materials, thus reaching the aluminium oxide and the underlying aluminium gate electrode. X-rays are then absorbed by the aluminium in these layers, determining a photoemission of charge carriers, which contributes to leakage current. The observed X-ray photocurrent can be attributed to a photoconductive gain mechanism, whereas the transient behaviour can be ascribed to stretched exponential recovery, caused by the slow relaxation time constant of trapped charge carriers [33]. The authors derived an interpretation of photoconductive gain according to the model developed in *Basiricò et al.* [17] for a low voltage

photoresistors using TIPS-Pentacene as photoconductive layer and reported above. This photoconductive gain is given by the equation (2.10):

$$G = \tau_r(\rho) / \tau_t \quad (2.10)$$

where  $\tau_r(\rho)$ , that is the charge carrier lifetime, is a function of the charge carrier density in the channel ( $\rho$ ), according to the equation (2.9), and  $\tau_t$  is the charge carrier transit time. The authors calculated from experimental data a value of photoconductive gain significantly bigger than the one obtained in *Basiricò et al* for the two terminals TIPS-pentacene-based device. Since in the transistor the TIPS-pentacene layer is integrated in a metal–insulator–semiconductor structure, additional effect related to the gate potential are present and they can be invoked for explain the larger value of the gain obtained [33]: when  $V_G$  increases, becoming more negative, the charge density in the transistor channel increases, enhancing the efficiency of both electron conduction and holes accumulation. Also the contact resistance decreases, because holes are more easily injected from the electrodes. Moreover, with over-threshold conditions, the charge carrier lifetime  $\tau_t$  decreases, further contributing to the enhancement of  $G$  (equation 2.10). The highest sensitivity, defined as the first derivative of the current amplitude with respect to the dose rate, for this transistor was obtained for  $V_G = -3$  V in saturation regime, and it was 1200 nC/Gy ( $\approx 5220 \mu\text{C}/\text{mGy}/\text{cm}^3$ ), a value comparable to or larger than the sensitivity values of most up-to-date hybrid organic/inorganic X-ray detectors. [37] [46] [4]. In order to span the device working regime from the OFF state ( $V_G < V_T$ ) to the ON state ( $V_G > V_T$ ), the authors maintained polarized the transistor at a constant drain-to-source voltage drop ( $V_D = -3$  V in saturation regime, and  $V_D = -0.25$  V in linear regime), and varied the  $V_G$  value. Figure 2.10a and b shows the acquired X-ray-induced photocurrent signal ( $I_D$  variation,  $|\Delta I_D|$ ), reported as a function of the dose rate for different  $V_G$  values in linear and saturation regimes. It is noteworthy that in both cases  $\Delta I_D$  under X-rays is negligible, independently from the dose rate of the impinging radiation, if the gate-to-source voltage has a value of 0 V. Therefore, when the device is in under-threshold conditions, X-ray response can be inhibited. This feature represents a significant advantage of this transistor-based detector, especially with respect to two-terminal devices [33].

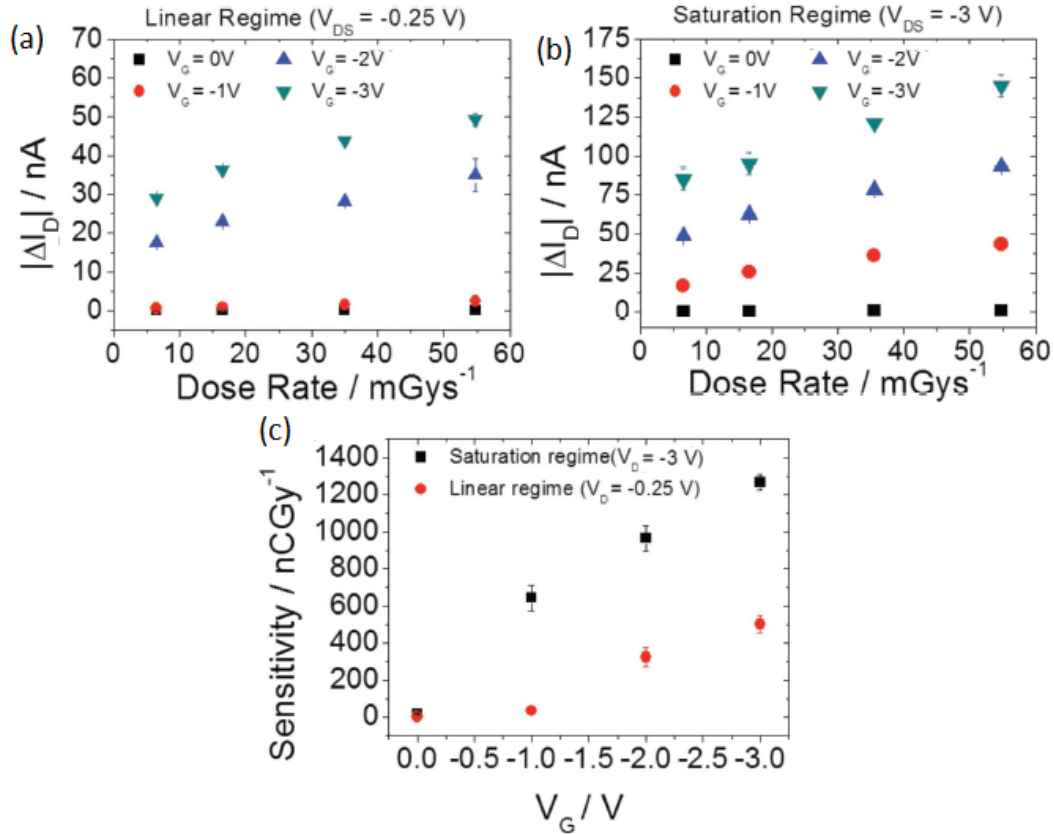


**Figure 2.10** *Lai et al.* [33]. Average device response to X-rays as a function of dose-rate in: (a) linear regime, (b) saturation regime. (c) Sensitivity reported as a function of the gate-to-source voltage in saturation regime and linear regime [33].

In both regimes, increasing the negative value of  $V_G$ , the transistor progressively turns on, and the response to the different dose rates progressively enhances. However, to obtain a significant increase of the response, larger over-threshold conditions are needed in linear regime. As already mentioned, the sensitivity reaches the higher values when the transistor channel is completely formed, that is when the gate voltage sets the transistor in the ON state. The interpretation proposed above for the gate-effect over the photoconductive gain, can also explain the lower sensitivity obtained, for a given  $V_G$  value, in the linear regime as reported in Figure 2.10c. Indeed, the influence of the injection resistance in the linear regime is bigger than in the saturation regime.

Polymers are been proposed as direct X-ray detectors in *Boroumand et al* [1]. Since they are characterized by low mobility [47], to use these material as detectors, the active volume must be kept rather thin in order to extract a useful current signal. On the other hand, it is however necessary to use a thicker detection layer, in order to achieve a sufficient interaction volume [1]. The authors tested the MEH-PPV (poly[1-methoxy-4-

(2-ethylhexyloxy)-phenylenevinylene] and PFO (poly(9,9-dioctylfluorene)) polymers. Given the conditions described above, in this kind of detector high electric field strengths are needed to maximize the displacement current from the drifting charge carriers, therefore an high quality rectifying junction with low reverse bias leakage current is required [1]. PFO device showed a sensitivity of 480 nC/mGy/cm<sup>3</sup> at -50 V, while the MEH-PPV device reached a sensitivity of 200 nC/mGy/cm<sup>3</sup> at -10 V [1]. The PTAA poly(triarylamine) polymer was studied for X-ray detection in *Intaniwet et al* [48] in 2009. Figure 2.11 reports the recorded X-ray induced photocurrents in a PTAA diode, after the subtraction of the device dark current, as function of the applied voltage for various dose-rates; The inset shows the X-ray photocurrent as a function of the dose rate, recorded when the devices was polarized with a reverse bias of 300 V. The photocurrent presents an initial growth in the photocurrent at low dose rates, followed by a region of linear response above  $\approx 2.5$  mGy/s. Here the sensitivity is about 0.3 nC/mGy.

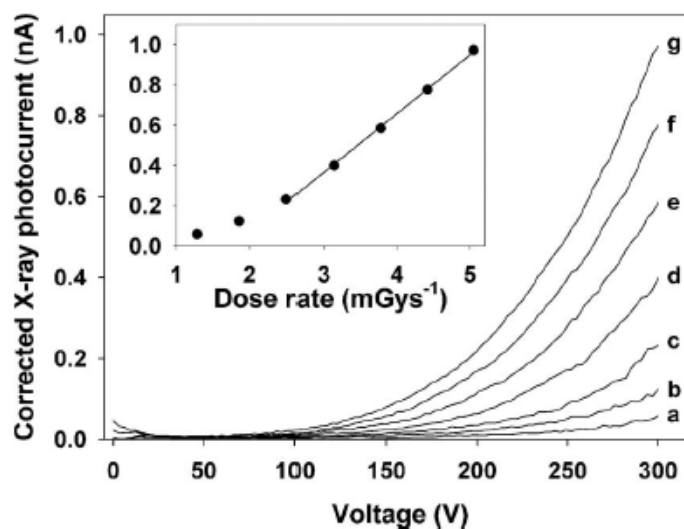


**Figure 2.11:** *Intaniwet et al* [48] PTAA diode: corrected X-ray photocurrent vs applied voltage at increasing dose rates when the device is reverse-biased. Dose rates: a= 1.28 mGy/s, b= 1.86 mGy/s, c=2.50 mGy/s, d=3.14 mGy/s, e=3.78 mGy/s, f=4.42 mGy/s, and g=5.05 mGy/s. Inset: corrected X-ray photocurrent vs X-ray dose rate, recorded at -300 V applied operating voltage [48].

An hybrid device, constituted by TIPS-Pentacene in a blend with PTAA in diode configuration, was tested as direct X-ray detector in *Intaniwet et al.* [49] in 2011. Five solution with PTAA:TIPS-Pentacene molar ratios of 1:1, 1:10, 1:17 and 1:25 were used to fabricate, by spin-coating, the devices. The mobility, measured by TOF technique, increases with TIPS-Pentacene concentration, with a maximum of  $2.2 \cdot 10^{-5} \text{ cm}^2/(\text{Vs})$  in the sample with 1:25 molar ratio. The authors ascribe this trend to a shift of charge transport domination from PTAA to TIPS-Pentacene, when the TIPS-Pentacene phase occupies a greater volume [49]. Figure 2.12 shows dynamic photocurrent responses for the devices having molar ratio until 1:17, biased at 40 V. This plot demonstrates that the X-ray induced photocurrent increases proportionally to the increasing of the X-ray dose rate, and that for all applied dose rates and operational voltages, the X-ray photocurrent increases with concentration of TIPS-Pentacene. The maximum sensitivity, reached in the 1:17 device is  $457 \text{ nC/mGy/cm}^3$ .

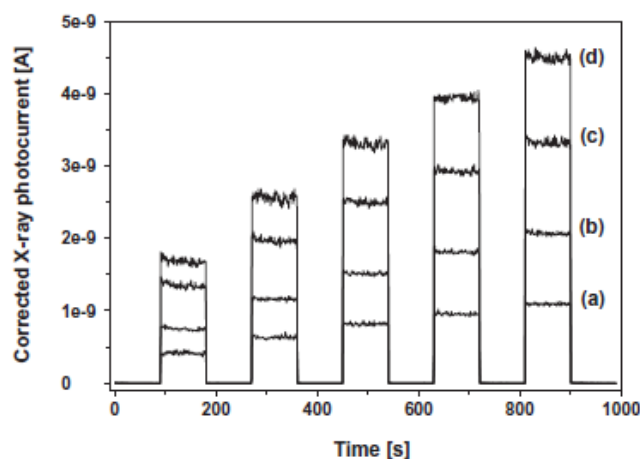


**Figure 2.12.** *Intaniwet et al* [49]: Response of an ITO/PTAA-based/Al sensors with an active layer ( $10 \mu\text{m}$  thick) of pure PTAA (a), and PTAA blended with TIPS-pentacene in a molar ratio of 1:1 (b), 1:10 (c), and 1:17 (d), when operated at 40 V. The devices were irradiated by 17.5 keV X-ray beams having dose rate from left to right of: 13 mGy/s, 27 mGy/s, 40 mGy/s, 54 mGy/s and 66 mGy/s [49].

## 2.4.2. Organic direct detectors based on Organic Semiconducting Single Cristal (OSSC)

Not only thin film detectors are fabricated and tested as X-ray detector, indeed in 2012 in *Fraboni et al* [50] two device based on two solution grown OSSCs, platelet-shaped 4HCB (4-hydroxycyanobenzene) and needle-like shape NTI (1,8-naphthaleneimide), shown in Figure 2.13, were investigated.

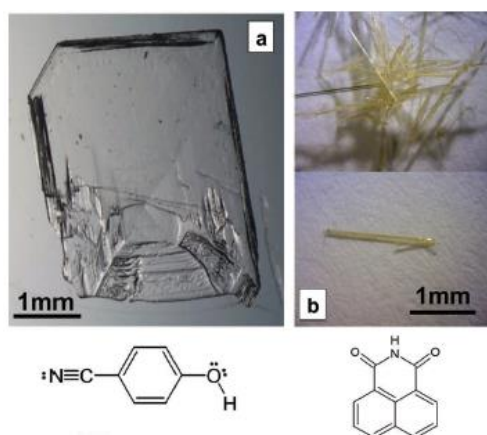


**Figure 2.13:** 4HCB (a) and NTI (b) single crystals: Optical microscopy images and molecular structure [50].

In the 4HCB crystal the authors evaluated an average mobility values for the two planar axes  $a$  and  $b$  of  $5 \cdot 10^{-2} \text{ cm}^2/(\text{Vs})$  and  $5 \cdot 10^{-3} \text{ cm}^2/(\text{Vs})$ , respectively, and of  $5 \cdot 10^{-6} \text{ cm}^2/(\text{Vs})$  for the vertical axis  $c$ . (see Figure 2.14).

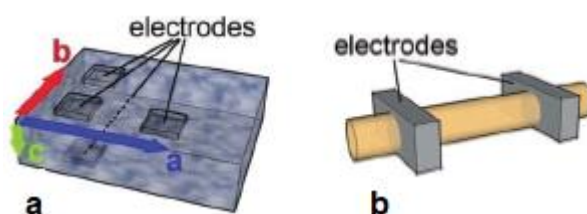


**Figure 2.14:** *Fraboni et al* [50]. Electrical contacts in a 4HCB crystal along the three crystallographic axes  $a$ ,  $b$ , and  $c$  (a), and in a NTI crystal (b) [50].

For both crystals, the normalized X-ray induced photocurrent, defined as  $(I_{\text{on}} - I_{\text{off}})/I_{\text{off}}$  (where  $I_{\text{on}}$  is the photogenerated current and  $I_{\text{off}}$  the dark current), presents a maximum at low voltages (in both planar axes in the case of 4HCB), therefore these devices may

be operated at voltages as low as 50 V, with low power consumption. The response for increasing X-ray dose rates is linear and fast (70 ms, a very good value for organic electronic devices), and no appreciable current drift or hysteresis are observed under repeated X-ray beam on/off cycles. Finally, the authors calculated a sensitivity, defined as  $S=\Delta I/D$ , where D is the dose-rate, of 0.05 nC/mGy on the planar axes of 4HCB crystals, and a similar value for NTI crystal, along its axis of growth [50].

Another paper about OSSCs was presented in in 2014 (*Fraboni et al* [36]). This work regards two detectors based respectively on 4HCB and DNN (1,5-dinitronaphthalene) single crystal, the latter characterized by a needles geometry (Figure 2.15). [51][50][49]



**Figure 2.15:** DNN organic single crystals: Optical microscopy image in transmission mode [36].

It is possible to grow the both types of crystals from widely available solvents/non-solvents techniques, and their size can be controlled by varying some parameters in the starting solutions, thus reaching sizes of tens of mm<sup>3</sup> [36]. Table 2.1 shows carrier mobilities measured by SCLC (Space Charge Limited Current) analysis reported in the literature [52] [53] [54] for a 4HCB crystal along the three crystallographic axes, and the mobility measured by the authors for a DNN crystal along its axis of growth, that is the only one crystallographic direction electrically accessed, because of its needle-like shape. This axis corresponds with the higher  $\pi$ -orbital overlap direction [55].

Crystal	$\mu\text{SCLC (cm}^2/(\text{Vs}))$
4HCB <i>a</i> axis	$(1.0\pm 0.5)\cdot 10^{-1}$
4HCB <i>b</i> axis	$(4\pm 2)\cdot 10^{-2}$
4HCB <i>c</i> axis	$(2.0\pm 0.5)\cdot 10^{-5}$
DNN	$(2.2\pm 0.8)\cdot 10^{-3}$

**Table 2.1:** Carrier mobility values reported in the literature [52] [53] [54] for a 4HCB crystal along the three crystallographic axes, and measured in *Fraboni et al* [36] for a DNN crystal along the axis of growth [36].

In Figure 2.16 the current-voltage and current–time curves measured for a DNN crystal exposed to an X-ray beam having a dose-rate of 140 mGy/s are reported. It is possible to notice an increase in the current, measured as a function of the applied voltage, under the X-ray beam, due to the photo-induced generation of charge carriers. This sharp response was obtained with applied voltages as low as 2V, thus confirming the possibility to work at low voltage for these devices. Moreover, another good result was obtained for the “off” current, that after the exposure to X-rays does not show significant hysteresis or degradation effects. As shown in Figure 2.16c, the crystal response for an increasing X-ray dose-rate is linear for each tested bias voltage, confirming the results obtained in 2012 in *Fraboni et al* [50]. The DNN-based detector sensitivity, defined as  $S=\Delta I/D$ , where *D* is the dose-rate, is 6 nC/mGy at 10 V [36]. In the 4HCB crystals, unlike DNN crystals, is possible to investigate the photo-response along all three crystallographic directions. The measured mobility values, reported in table 2.1, suggest that the tighter  $\pi$ -stacking axes are the two planar axes, characterized by a good mobility, whereas the vertical axis, that possesses a much smaller mobility, has a poorer  $\pi$ -stacking degree. Nevertheless, in the 4HCB crystals, the X-ray induced photocurrent response is smaller along the planar axes, and this also occurs for the sensitivity, that, when the device is polarized at 10V has a value of 7 nC/Gy along the planar axes, and 24 nC/Gy along the vertical one. Moreover, it is possible to notice that the sensitivity obtained along the main  $\pi$ -stacking axis for DNN and 4HCB crystals are comparable.

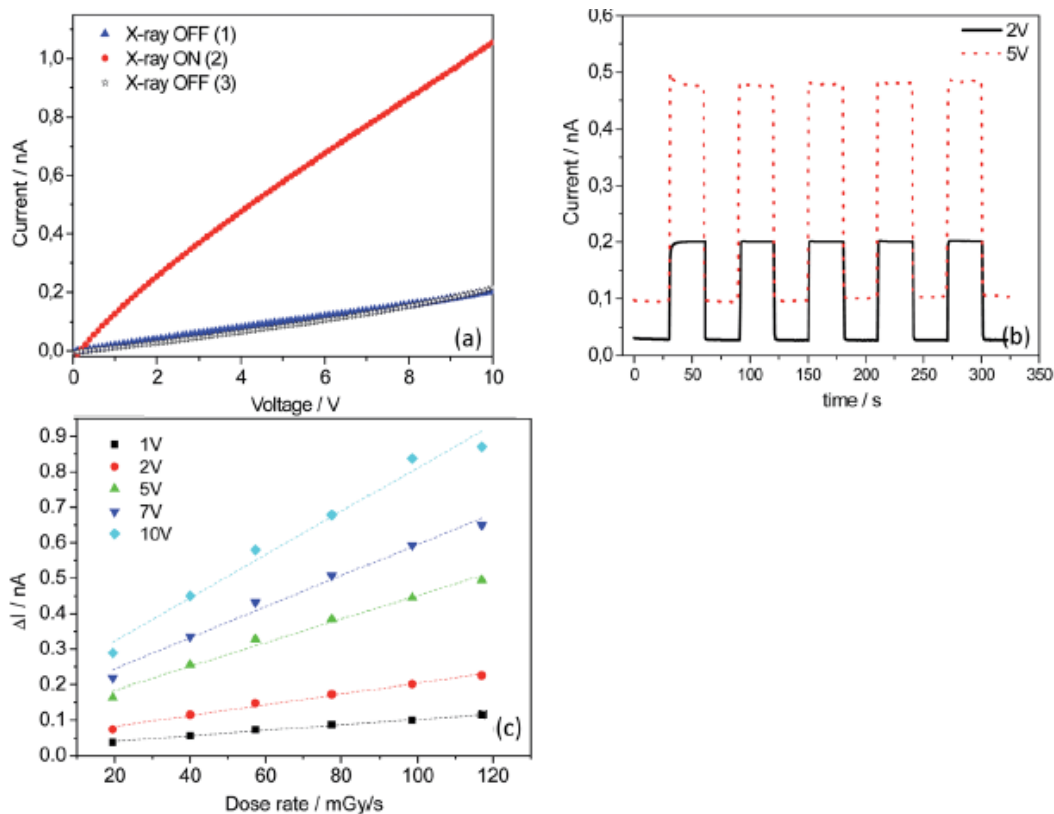


**Figure 2.16:** Fraboni *et al* [36]: (a) Current–voltage curves of a DNN crystal. under X-ray irradiation at 117 mGy/s (red circles), before the irradiation (blue solid triangles), and after the irradiation (black empty stars). (b) Current–time curves of the DNN-based detector recorded turning on and off the X-ray beam, for two different applied bias voltages (2V and 5V). (c) Detector sensitivity for different bias voltages [36].

Therefore, the planar electrode configuration is less performing, independently of the crystal shape (needle-like or platelet). The authors retain that the better electrical transport properties along crystal axes with strong  $\pi$ -stacking may limit the sensitivity of the crystals to X-rays, because of the higher off currents. Moreover, as indicated in Figure 2.17a and b, in the vertical geometry the whole electrode area can actively collect the induced charge carriers, whereas in the planar geometry the collection is possible only in a thin region around the electrode edge. Finally, the  $\pi$ -electrons at the crystal surface have a high polarizability, probably further enhanced by the direct exposure to X-rays, that may cause the ionization of organic molecules. Therefore, an interaction with polar environment molecules (water, etc.) becomes possible. When these molecules are adsorbed at the surface, can affect the trapping states and the carrier density distribution in the first monolayer below the surface.

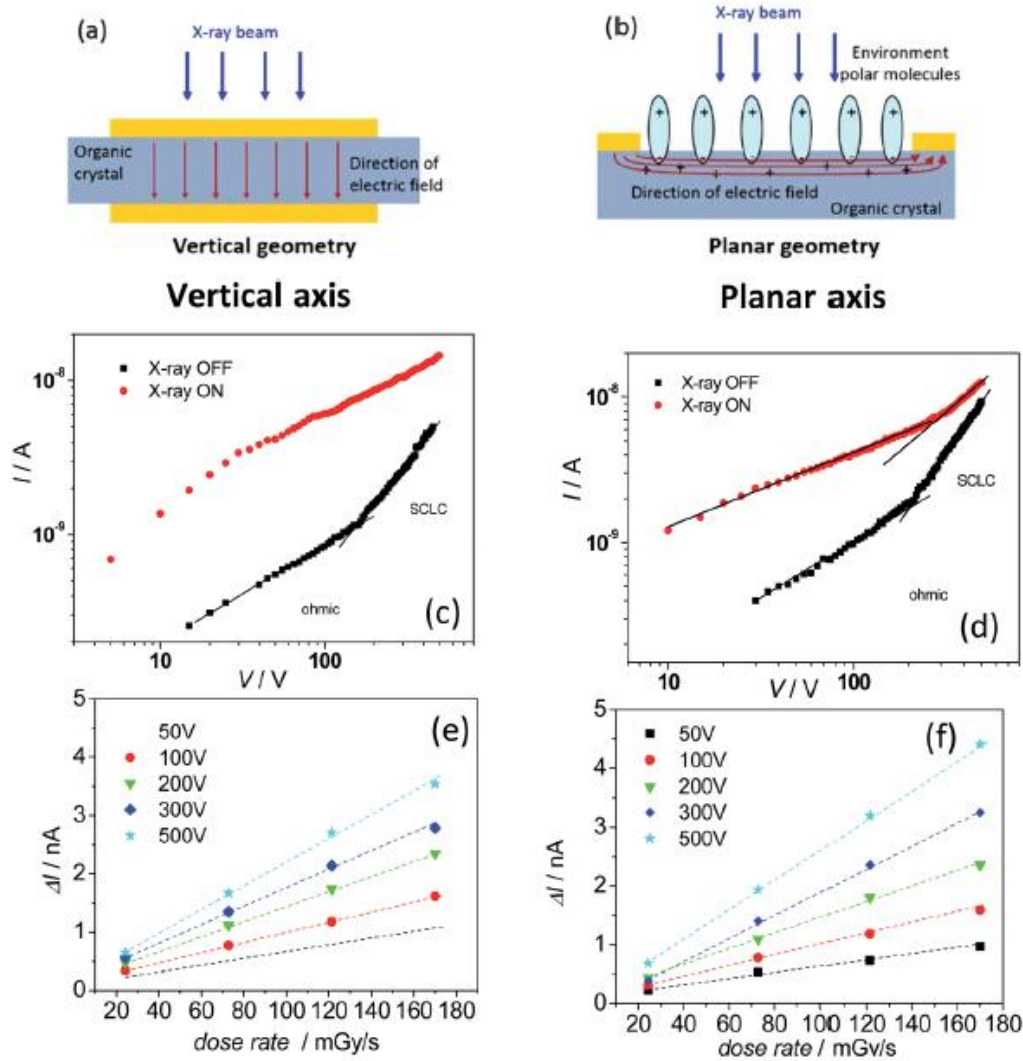


**Figure 2.17:** Fraboni *et al* [36] Electric field distribution in the vertical (a) and planar (b) geometries in 4HCB crystals. (c) (d) Current–voltage curves for the two axes under an X-ray beam having dose-rate of 170 mGy/s and in the dark. In both plots, the lack of the ohmic - SCLC transition under irradiation is indicated. (e) (f) X-ray-induced photocurrent ( $I_{\text{on}}-I_{\text{off}}$ ) as a function of the dose-rate at different bias voltages, along the two axes [36].

In another work, Ciavatti *et al* [56], 4HCB was investigated as low-voltage and bendable X-ray direct detectors. In all the three tested configurations, S1, S2, and S3 (see Figure 2.18), this OSSC, when irradiated by an X-ray beam, demonstrated a response linear with the dose-rates, for different bias voltages in the range 10V-500V. The maximum obtained sensitivity, defined as  $(I_{\text{on}}-I_{\text{off}})/(\text{dose-rate})$ , is 175 nC/Gy at 500 V, in configuration S2.

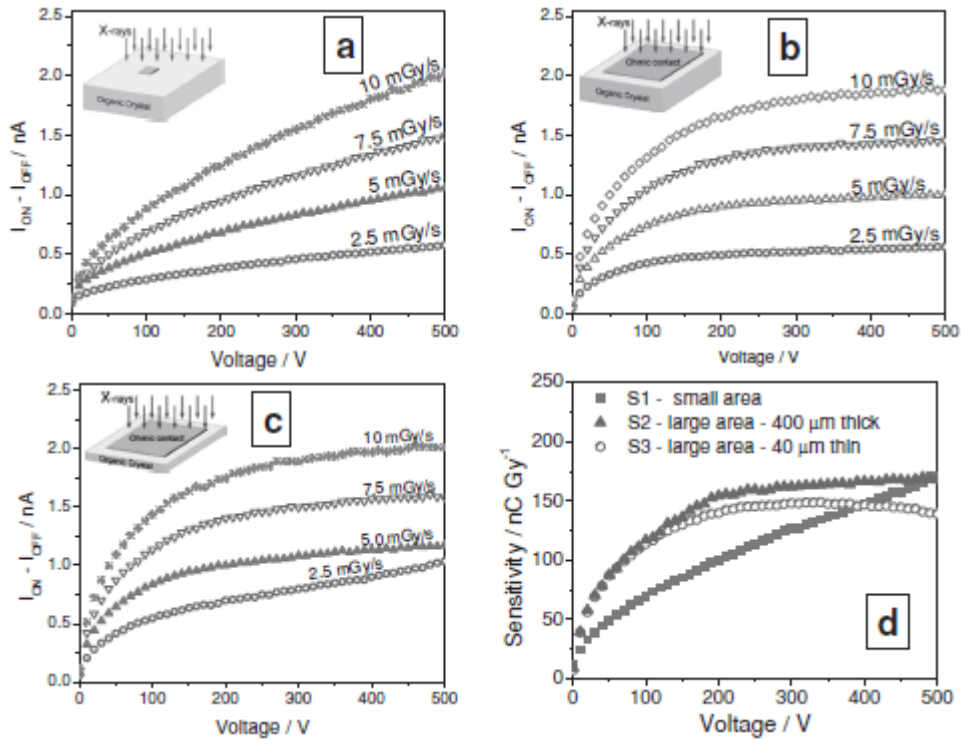


**Figure 2.18:** Ciavatti *et al* [56]. Current–voltage characteristics, measured along the vertical axis, of 4HCB organic crystals irradiated by an X-ray beam: (a) thick (400  $\mu\text{m}$ ) crystal having small top contact area (0.15  $\text{mm}^2$ ). (b) thick (400  $\mu\text{m}$ ) crystal having large area contact (2  $\text{mm}^2$ ). (c) thin (40  $\mu\text{m}$ ) crystal having large area contact (2  $\text{mm}^2$ ). (d) Sensitivity as function of the applied voltage bias for the crystals with the three configurations [56].

Figure 2.18d reports the sensitivities of the crystals in the three configurations as a function of the applied bias voltage. It is possible to notice that thick (400  $\mu\text{m}$ ) and thin (40  $\mu\text{m}$ ) crystals having large area electrodes (S2, S3) have comparable sensitivities and reach saturation at voltages  $<150$  V, whereas the devices in configuration S1 (small contact area) reach the sensitivity to which the other samples saturate only when biased at 500 V. These 4HCB-based detectors can detect a minimum X-ray dose rate of 50  $\mu\text{Gy/s}$ , in line with the typical values for diagnostic medical applications (dose rates around 25  $\mu\text{Gy/s}$  [57]). Finally, the authors realized a bendable OSSC-based detector onto a plastic substrate with interdigitated electrodes, as shown in Figure 2.19.

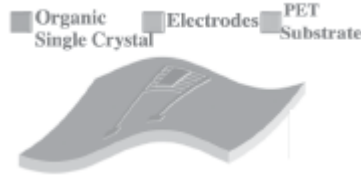


**Figure 2.19:** (a) Schematic view of the flexible X-ray detector realized onto a plastic substrate with interdigitated electrodes [56].

The repeated bending procedure did not alter the electrical performance of the device, thus supporting the feasibility for bendable X-ray detectors based on organic single crystals [56]. Moreover, OSSCs showed an high radiation hardness, with respect other organic X-ray detector [36] [50].

## 2.5. Detector based on alternative materials: perovskites

Organolead trihalide perovskites (OTPs) emerged as a new generation of photovoltaic material, reaching high power conversion efficiencies (around 20%), and thanks to their high-Z elements Pb, I and Br OTPs are also investigated for radiation detection. [58]. In the paper *Wei et al.* [58] a 2-mm-thick MAPbBr<sub>3</sub> single-crystal device was studied (MA indicates methylammonium). The authors fabricated two crystals: one grown with PbBr<sub>2</sub>/MABr molar ratios of 1.0 (MAPbBr<sub>3</sub>-MR1.0) and one grown with PbBr<sub>2</sub>/MABr molar ratios of 0.8 (MAPbBr<sub>3</sub>-MR0.8). For the MAPbBr<sub>3</sub>-MR0.8 single crystal the authors calculated a hole mobility of 217 cm<sup>2</sup>/(Vs), and for the MAPbBr<sub>3</sub>-MR1.0 single crystal a hole mobility of 206 cm<sup>2</sup>/(Vs). The lowest dose rate detectable by the MAPbBr<sub>3</sub>-MR0.8 device is of 0.5 μGy<sub>air</sub>/s, and the sensitivity is of 400 μC/Gy<sub>air</sub>/cm<sup>3</sup> (Figure 2.20) [58].

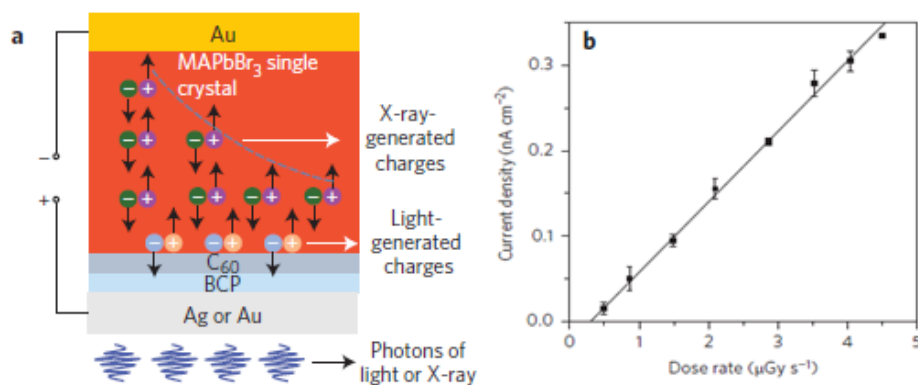


**Figure 2.20.** Wei *et al* [58]. (a) Single crystal OTP radiation detector. (b) MAPbBr<sub>3</sub>-MR0.8 device: X-ray-induced photocurrent as a function of dose-rate. [58].

In another paper, Yakunin *et al* [46], MAPbI<sub>3</sub> was investigated as X-ray direct detector in both photovoltaic (p-i-n junction) and photoconductive device architectures. These devices in solar cells configuration take full advantage of the high optical absorbance of the MAPbI<sub>3</sub> in the visible and near-infrared spectral regions. Moreover, they are characterized by a long exciton diffusion lengths, and by a high carrier mobility, with respect than the other common solution-processed semiconductors [46]. In the devices realized in photovoltaic configuration, the X-ray-induced photocurrent density has a linear dependence on the dose-rate of the X-ray beam. (fig 2.21b) and the maximum specific sensitivity reached is of 25  $\mu\text{C}/\text{mGy}/\text{cm}^3$ . Similar results were obtained also for the photoconducting devices.

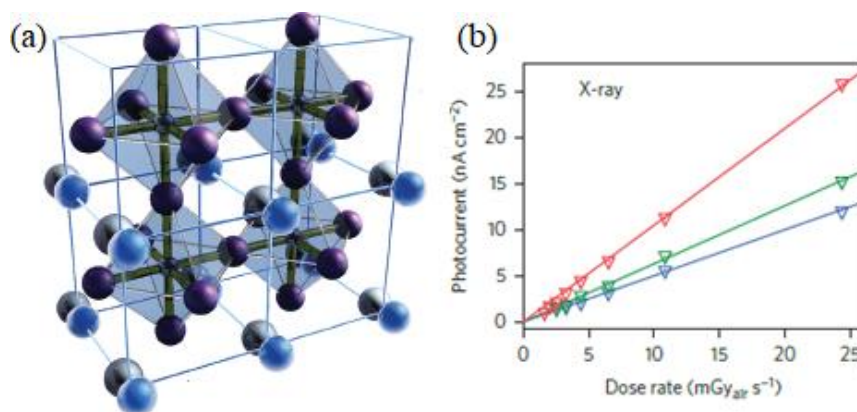


**Figure 2.21:** Yakunin *et al.* [46] (a) Crystal structure of the perovskite. Blue spheres indicate the methylammonium, black spheres the iodine, and in the centres of the octahedrons there is the lead. (b) Averaged short-circuit X-ray photocurrent as function of dose rate in a photovoltaic device. The blue triangles corresponds to the layer with thickness of (260±60) nm, the green triangles corresponds to the layer with thickness of (360±80) nm and red triangles correspond to the layer with thickness of (600±120) nm [46].

Single crystals of semiconducting hybrid lead halide perovskites (MAPbI<sub>3</sub>, FAPbI<sub>3</sub> and I-treated MAPbBr<sub>3</sub>, where FA is formamidinium) were studied in 2016 (*Yakunin et al* [59]). The devices realized with this kind of perovskites was characterized as X-ray and  $\gamma$ -ray detector, thus showing that perovskites can serve also as  $\gamma$ -ray-detecting materials. Regarding X-ray radiation, the sensitivity of MAPbI<sub>3</sub> devices to soft X-ray photons (Cu K $\alpha$ , 8 keV), was evaluated as 0.65  $\mu\text{C}/\text{mGy}_{\text{air}}/\text{cm}^2$ . The penetration depth of X-ray radiation in these detectors is 30  $\mu\text{m}$ , therefore the specific sensitivity is  $\sim 220 \mu\text{C}/\text{mGy}_{\text{air}}/\text{cm}^3$  [59].

## 2.6. Hybrid organic/inorganic ionizing radiation detectors

An interesting solution to improve the X-ray detection sensitivity in organic detectors was proposed in 2014 in *Han et al.* [4]. The authors used single-walled carbon nanotubes (SWNTs) in order to enhanced X-ray detection sensitivity [4]. The active layer of the device was realized by a composite of SWNT and SY polymer (“Super Yellow”) coated onto a PET substrate.

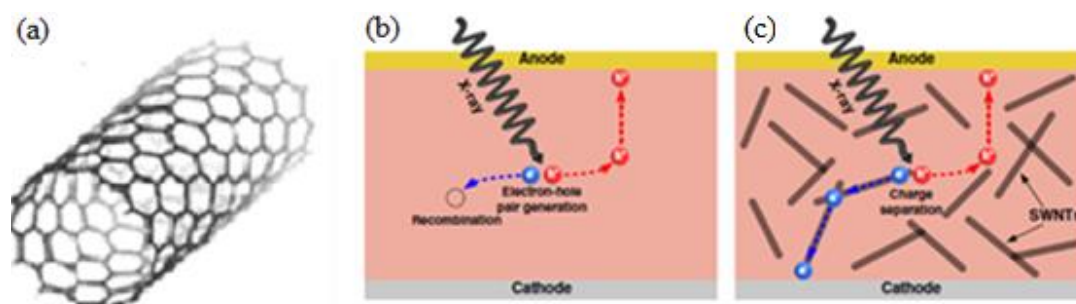


**Figure 2.22:** (a) A single walled carbon nanotubes [60]. (b) X-ray induced charge separation in pure p-type polymer device (b), and in a SWNT enriched polymer composite device presented in *Han et al.* [4].

Charge separation mechanism in the devices presented in *Han et al.* [4] is reported in Figure 2.22c. The p-type conjugated polymers have low electron mobility and high recombination rate, consequently when they are used as active layer in X-ray detectors produce a low photocurrent. In presence of SWNTs in the active layer, charge separation can easily occur at the polymer-SWNT interface [4]. After the separation, the holes

move into the polymer and electrons move into the SWNTs, characterized by a greater electron affinity compared to the polymer [61]. As a result of this effective charge separation, the X-ray induced photocurrent and the sensitivity of these devices increase (Figure 2.23). The maximum sensitivity was founded in the sample with the SWNTs concentration of wt.0.01%, which is the largest tested. When this device is biased at -150V its value is  $38.9 \mu\text{C}/\text{mGy}/\text{cm}^3$ , whereas the sensitivity of the sample without SNWTs is  $12.5 \mu\text{C}/\text{mGy}/\text{cm}^3$  [4]. This confirms that SWNTs improves the performance of the polymer-based X-ray detectors. Moreover, the polymers are composed of cross linked molecules, and SWNTs have exceptional mechanical properties, therefore this detector is also characterized by mechanical flexibility [4].

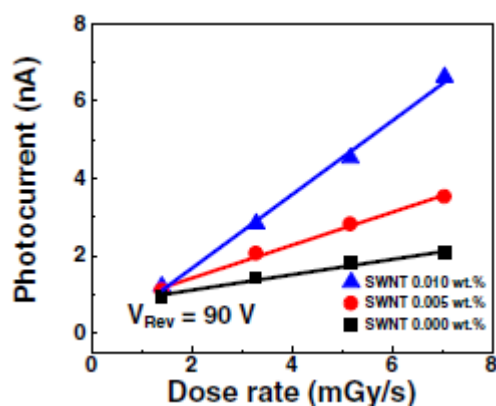


**Figure 2.23:** Photocurrents of devices presented in *Han et al* [4] with two different SWNT concentrations as a function of applied X-ray dose rate under a reverse bias voltages of 90 V. [4].

Instead of SNWTs, in *Intaniwet et al.* [2] the use of heavy metallic oxide nanoparticles in order to enhance sensitivity in semiconducting polymer-based X-ray detectors is proposed. In this case the authors took advantage of high atomic number Z bismuth oxide ( $\text{Bi}_2\text{O}_3$ ) nanoparticles (NPs), that have a higher absorption cross section, with respect to the conjugates polymers, characterized by low atomic number Z [2]. More specifically the authors realized samples constituted by the PTAA semiconducting polymer and ( $\text{Bi}_2\text{O}_3$ ) nanoparticles at various concentration. The Figure 2.24a shows the theoretical attenuation quantum efficiency (defined as  $1 - I/I_0$ , where  $I_0$  and  $I$  are the incident and transmitted radiation intensities) of a  $20 \mu\text{m}$  PTAA film, as a function of

the percentage weight concentrations of  $\text{Bi}_2\text{O}_3$  nanoparticles. It is possible to notice that it increases with the concentration of  $\text{Bi}_2\text{O}_3$  nanoparticles.

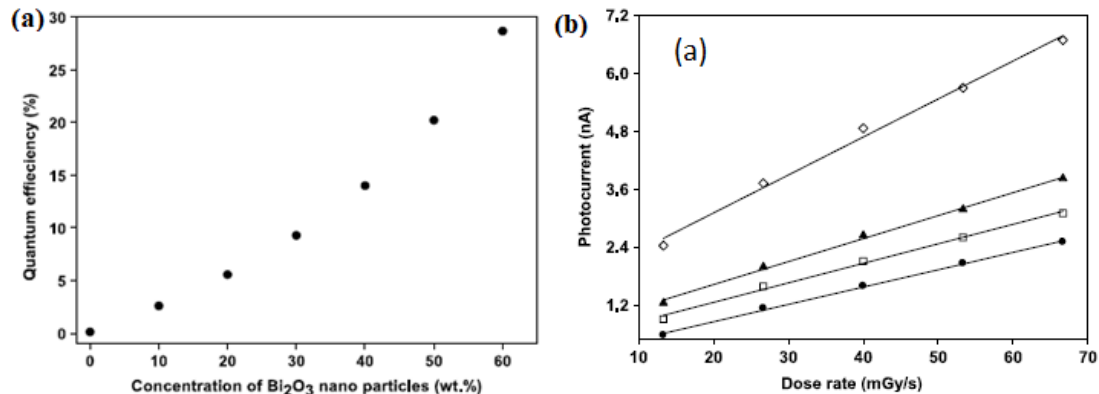


**Figure 2.24:** (a) Theoretical quantum efficiency of a 20 μm PTAA film, as a function of the percentage weight concentrations of  $\text{Bi}_2\text{O}_3$  nanoparticles. (b) X-ray induced photocurrent as a function of dose rate at an applied voltage of -150 V in the devices presented in *Intaniwet et al.* [2]. Circles indicate the pure PTAA device, squares the  $\text{Bi}_2\text{O}_3$  wt.20% device, triangles the  $\text{Bi}_2\text{O}_3$  wt.40% device and rhombus the  $\text{Bi}_2\text{O}_3$  wt.60% device [2].

As shown in Figure 2.24b, the induced X-ray photocurrent increases with the concentration of the  $\text{Bi}_2\text{O}_3$  nanoparticles present in the polymer matrix. Regarding the sensitivity, the authors observed an increase of about 2.5 times, from 78 nC/mGy/cm<sup>3</sup> in the pure PTAA device to 200 nC/mGy/cm<sup>3</sup> in the  $\text{Bi}_2\text{O}_3$  wt.60% device. (at a bias voltage of -200V) [2]. Therefore, they concluded that the high-Z nanoparticles act as X-ray absorbers, producing secondary, lower energy X-ray and electron showers, that are more likely to interact directly with the polymer. Alternatively they can become charged, inducing the formation of charge on the polymer in a typical semiconductor acceptor/donor method [2].

Also in *Mills et. al* [3] nanoparticles are studied in order to enhanced X-ray detection sensitivity in semiconducting polymer. This work concerns the comparison of 5 μm thick semiconducting poly([9,9-dioctylfluorenyl-2,7-diyl]-co-bithiophene) (F8T2) diodes containing two type of nanoparticles (NPs) respectively: metallic tantalum and electrically insulating bismuth oxide. Figure 2.25a shows the theoretical attenuation quantum efficiency of 17.5 keV X-rays on 5 μm thick F8T2 films, as a function of concentration of the two nanoparticles.

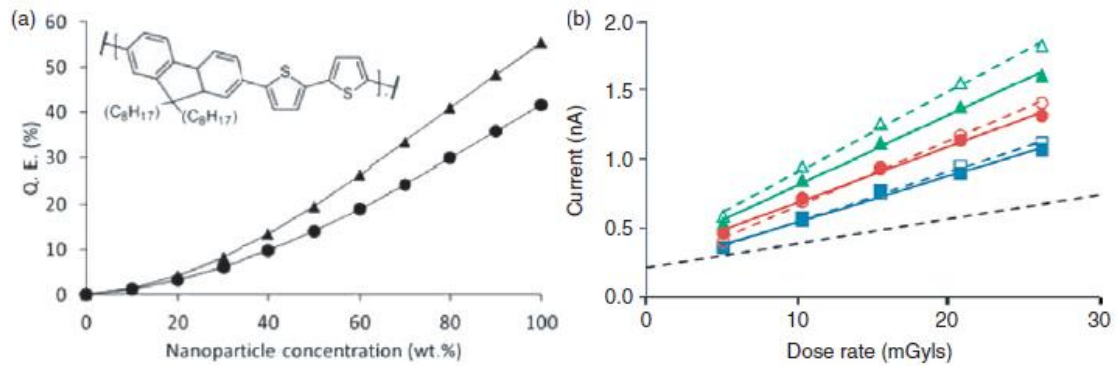


**Figure 2.25.** (a) Theoretical Quantum efficiency of 5  $\mu\text{m}$  F8T2 films incorporating Bi<sub>2</sub>O<sub>3</sub> (●) and Ta (▲) nanoparticles as a function of NPs concentration. In the inset the chemical structure of F8T2 is drawn. (b) Induced photocurrent in F8T2 devices, presented in *Mills et. al* [3], having Al top electrodes (open symbols) and Au top electrodes (solid symbols), and incorporating Bi<sub>2</sub>O<sub>3</sub> NPs at concentration of wt.30 % (■), wt%.42 (●), and wt%.57 (▲), irradiated with 17.5 keV Mo K $\alpha$  X-rays [3].

The Figure 2.25b reports the photocurrent produced by F8T2 diodes containing Bi<sub>2</sub>O<sub>3</sub> nanoparticles at 4 concentrations and having different top electrodes ([Al] or [Au]), when they are irradiated with 17.5 keV X-rays. The induced photocurrent increases with the concentration of added Bi<sub>2</sub>O<sub>3</sub>. The sensitivity of the pristine F8T2 devices with Al top contacts is 141 nC/mGy/cm<sup>3</sup>. The devices containing Bi<sub>2</sub>O<sub>3</sub> NPs at wt.57% reached a sensitivity of 468 nC/mGy/cm<sup>3</sup> (Al top contacts), while the devices containing Ta NPs at wt.30% (the major concentration of Ta NPs reported) has a sensitivity of 439 nC/mGy/cm<sup>3</sup> (Al top contacts) [3].

Finally, about the alternative materials, is possible to found the work presented in 2015 in *Büchle et al* [37]: a detector realized by including terbium-doped gadolinium oxysulfide (GOS:Tb) scintillator particles into an organic photodetector matrix, in order to create a quasi-direct X-ray detector. Nowadays most common flat-panel X-ray detectors for medical imaging are constituted by a scintillator that converts X-ray photons into light and a photodetector array realized with amorphous silicon [37]. Organic photodiodes (OPDs) have been proposed for this application, because they are characterized by the advantage of organic semiconducting materials. OPD technology is based on a bulk heterojunction (BHJ), constituted by an interpenetrating donor-acceptor network of an electron conductor, such as phenyl-C61-butyric acid methyl ester (PCBM), and a hole conductor, such as poly(3-hexylthiophene-2,5-diyl) (P3HT) [62]. In these structure, when a photon is absorbed, a Frenkel exciton is generated, and

then it travels to the donor-acceptor interface, where it splits into a hole and an electron, that reach their respective electrodes through the donor and acceptor percolation paths, thus enabling photodetection [37]. An improvement can be achieved if appropriate nanoparticles, that can sensitize the absorption spectrum of pure P3HT:PCBM blends from the near-infrared to the X-ray region, are included in this blends. In this article, for this purpose, the authors used scintillating terbium-doped gadolinium oxysulfide (GOS:Tb) X-ray absorbers. The optimum volume ratio between BHJ constituents and nanoparticles depends on the absorption properties of the BHJ and the emission properties of the nanoparticle. A core-shell model allows to find the ideal volume ratio between X-ray converting GOS:Tb cores and photon-absorbing BHJ shells. Assuming that GOS:Tb particles are characterized by an average diameter of 1.8  $\mu\text{m}$ , the ideal volume ratio is 67% [37]. If nanoparticles have a concentration below this “golden filling factor” the X-ray absorption and the generation of charge carriers are limited, whereas a nanoparticles concentration above the golden filling factor perturbs the extraction of photogenerated charge carriers [37]. From the plot in Figure 2.27 is possible to notice that for low filling ratios the authors obtained an increase of the sensitivity with the fraction of GOS:Tb, which is due to increased X-ray absorption. When the device is polarized at 0 V the sensitivity has a maximum for GOS:Tb fraction of vol.60%, that is close to the golden filling factor. At higher GOS:Tb contents, the sensitivity at this bias decreased, because the charge transport in remaining BHJ degrades. If a bias voltage larger of 0 V is applied, the sensitivity in the devices having GOS:Tb fractions above the golden filling factor increases dramatically. The authors justify this phenomenon with a photoconductive gain mechanism. The GOS:Tb 50%vol device at -10 V/ $\mu\text{m}$ , has an X-ray sensitivity of 576000 nC/mGy/cm<sup>3</sup>. This value is slightly larger than the one obtained in a-Se direct converter at an electrical field of 10 V/ $\mu\text{m}$  [63].

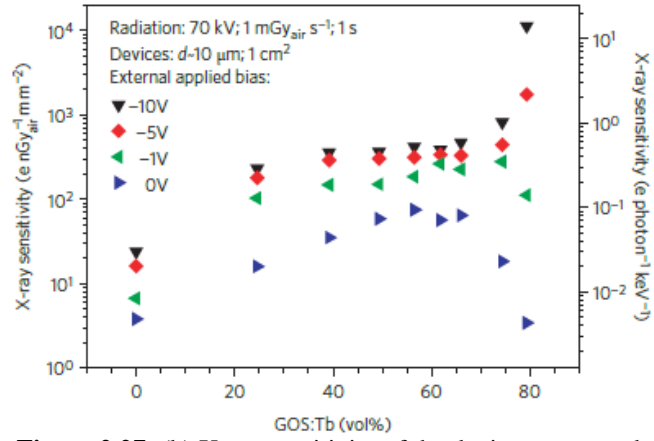


**Figure 2.27:** (b) X-ray sensitivity of the devices presented in Büchele *et al* [37], having different concentration of GOS:Tb particles, irradiated with a spectrum of 70 kV bremsstrahlung and dose rate of 1 mGy<sub>air</sub>/s at different external bias [37].

### 3. Materials and methods

The samples investigated in this work are organic thin film transistor realized by drop-casting and spin-coating, from solutions of diF-TEG-ADT and diF-TES-ADT (Figure 3.1) in chlorobenzene. The OTFTs structure are provided by the Department of Electrical and Electronic Engineering of the University of Cagliari, following the procedure described by *Cosseddu et al.* [64] except for the deposition of semiconductor. The tested molecules, diF-TES-ADT and diF-TEG-ADT, have been synthesized and provided by Professor J. Anthony, University of Kentucky

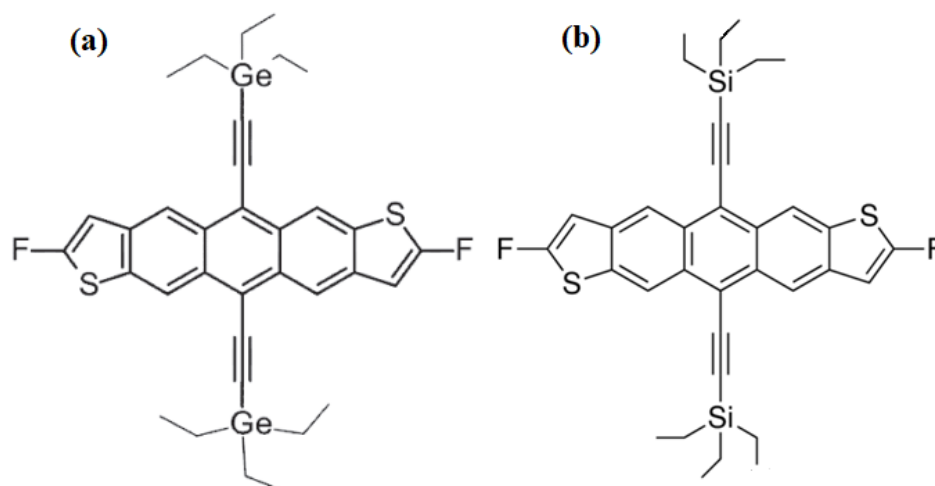


**Figure 3.1:** diF-TEG-ADT [29] (a) and diF-TES-ADT [11] (b).

At first, 4 devices per molecule were fabricated by drop-casting, in order to evaluate the suitability of this deposition technique to fabricate transistors as X-ray detectors. Subsequently, the other samples were fabricated by spin-coating. More precisely, by this deposition technique, 21 devices were realized with solutions having three different concentrations in weight (wt.0.5%, wt.1.2% and wt.2%) of diF-TES-ADT, and 18 were realized with solutions having the same three different concentrations in weight of diF-TEG-ADT. The transistors were characterized electrically acquiring output and transfer curves. Subsequently they were exposed to 4 on/off X-ray irradiation cycles, at 4 different dose-rates (see following paragraphs for further details). After the irradiation the output and transfer characteristics were again acquired. Finally, the characteristics electrical parameter (threshold voltage  $V_T$ , mobility  $\mu$  and  $I_{on}/I_{off}$  ratio) and the

sensitivity under X-rays were extracted. The characterized devices were photographed by means of the optical microscope (OPTIKA microscope ZSM 2)

### 3.1. Devices preparation

Solutions of the two molecules (respectively diF-TES-ADT and diF-TEG-ADT), at various concentration in weight (wt.1.2%, wt.0.5%, wt.2%) were prepared and deposited, at first by drop-casting and then by spin-coating, over a 175  $\mu\text{m}$  thick, OTFT structure (Figure 3.2).

This OTFT structure, presented in schematic view in Figure 3.2 and 3.3, is fabricated over a PET substrate in configuration bottom gate-bottom contacts, following the procedure described in [64]. The gate electrode is constituted by an aluminium layer of 100 nm thick, over which is deposited the dielectric layer, formed by a combination of Parylene C and aluminium oxide ( $\text{Al}_2\text{O}_3$ ). This combination allows to obtain, thanks to  $\text{Al}_2\text{O}_3$ , a high gate capacitance and, thanks to Parylene C, an efficient barrier to the gate current leakage. Moreover, Parylene C ensures an optimal interface with the organic semiconductors [64]. The reached gate capacitance is of 18  $\text{nF}/\text{cm}^2$  [33]. The source and drain electrodes are constituted by an 80 nm thick gold layer, and they are characterized by an interdigitated geometry (Figure 3.3). Width and length channel of the device were measured in a previous work by an optical microscope (OPTIKA microscope ZSM 2), obtaining  $W = (50.000 \pm 0.002) \text{ mm}$  and  $L = (45 \pm 2) \mu\text{m}$  [33].

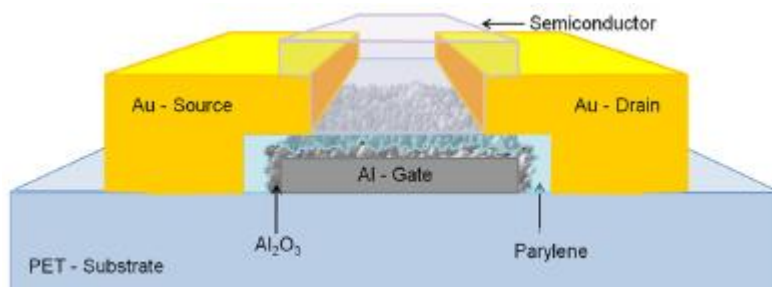


**Figure 3.2:** View in section of a channel of the interdigitated structure belonging to the OTFT structure realized by the group of Prof. Cosseddu [64].

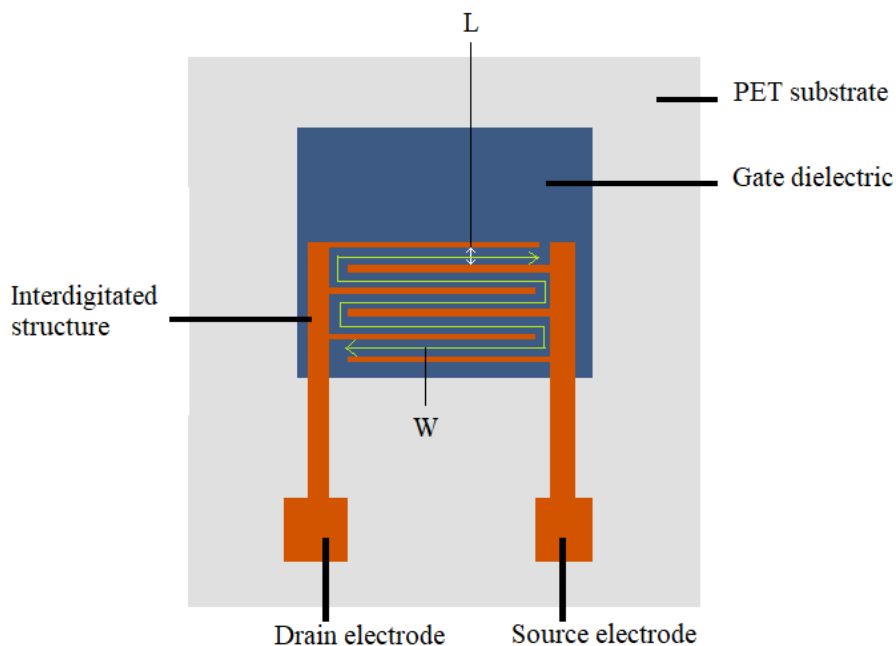


**Figure 3.3:** Schematic top view of the OTFT structure realized by the group of Prof. Cosseddu. It is possible to notice the interdigitated geometry of the source and drain electrodes.  $W$  and  $L$  are indicated. In order to contact the gate electrode, it is necessary to scratch the gate dielectric.

### 3.1.1. Fabrication of drop-casted samples

Four devices per molecule type were realized by drop-casting. The two starting solutions in chlorobenzene were both at concentrations of 0.5% in weight. In order to achieve a homogeneous solution, after the addition of the solvents in the vial containing the solute, they were stirred and heated at 100°C for 1 hour. After that, 4  $\mu\text{L}$  of the solution were drop-casted over each substrate described above, heated at 90°C. Immediately after the deposition the substrates were covered, in order to slow the crystallization. The devices were then shielded from the visible light and annealed for 2 h at 90°C and finally measured.

### 3.1.2. Fabrication of spin-coated samples

Because of the poor results obtained with the devices fabricated by drop-casting, another batch of samples was realized by spin-coating, using the procedure suggested in Ref. [65]. The fabrication started from the preparation of solutions in chlorobenzene of the two molecules at concentrations of 0.5%, 1.2% and 2% in weight. In the previous deposition it was possible to determine that the solutions appeared homogeneous just after few minutes, therefore in this case they were stirred at room temperature for a period of ten minutes, after which they were spin-coated over the OTFT structure mentioned above. The spin-coating was realized by 6806 spin coater (Speciality Coating Systems USA, Figure 3.4) at 1000 rpm for 60 s with an acceleration time of 1 s. After the deposition, the samples, shielded from visible light, were put under vacuum ( $\approx 0.1$  mbar) for 24 hours, in order to remove any trace of solvent, and then analysed.



**Figure 3.4:** 6806 spin coater (Speciality Coating Systems, USA).

## 3.2. Electrical characterization

Electrical characterization was performed using dual channel Keithley 2614B SourceMeter (Figure 3.5) and a custom made Labview software. Tables 3.1 and 3.2 reports respectively the voltage and the current measurement accuracies of this SourceMeter, as a function of the range of measurement used and of the measurement

itself, at a temperature of  $(23\pm 5)^{\circ}\text{C}$  [66]. In both cases, if the measurements are carried out at a different temperature is possible to obtain the accuracy applying the equation (3.1) [66]:

$$A(T) = \frac{(0.15 \cdot A(T_0))}{T} \quad (3.1)$$

Where  $A(T)$  is the accuracy at temperature  $T$  and  $A(T_0)$  is the accuracy at temperature  $T_0 = (23\pm 5)^{\circ}\text{C}$ .

Voltage measurement accuracy of Keithley 2614B SourceMeter	
Range	Accuracy at $T_0 = (23\pm 5)^{\circ}\text{C}$ (% of reading + a constant value)
100 mV	0.015% + 150 $\mu\text{V}$
1 V	0.015% + 200 $\mu\text{V}$
6 V	0.015% + 1 mV
40 V	0.015% + 8 mV

**Table 3.1:** Voltage measurement accuracy of Keithley 2614B SourceMeter [66]

Current measurement accuracy of Keithley 2614B SourceMeter	
Range	Accuracy at $T_0 = (23\pm 5)^{\circ}\text{C}$ (% of reading + a constant value)
100 nA	0.05% + 100 pA
1 $\mu\text{A}$	0.025% + 500 pA
10 $\mu\text{A}$	0.025% + 1.5 nA
100 $\mu\text{A}$	0.02% + 25 nA
1 mA	0.02% + 200 nA

**Table 3.2:** Current measurement accuracy of Keithley 2614B SourceMeter [66]

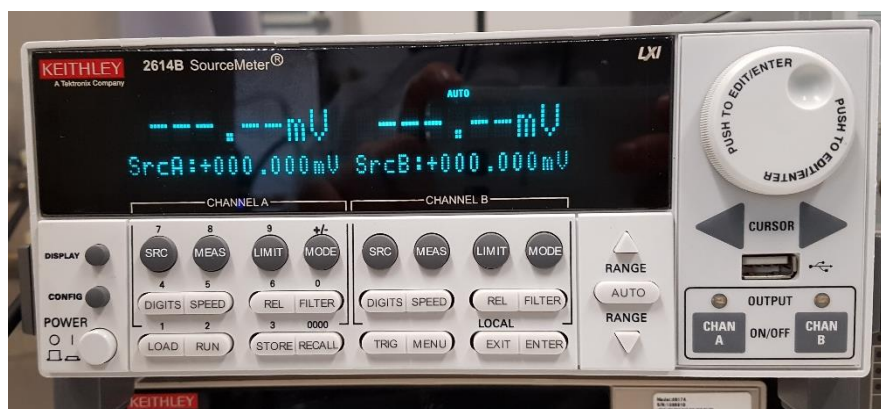


**Figure 3.5:** SourceMeter Keithley 2614B. Front Panel.

The measurements were carried out keeping the device in dark in a metal Faraday cage (visible in Figure 3.7), in order to avoid light-induced photogeneration and reduce electrical noise in the organic semiconductor. The schematic view of the samples and of the connection realized in order to characterize electrically these devices are reported in Figure 3.6. The source, drain and gate electrodes have been connected respectively with three BNC connectors in the edge of Faraday Cage, in their turn connected with the SourceMeter. Output and transfer characteristics were acquired before and after the X-ray irradiation, in order to evaluate the behaviour of the device before and after the irradiation. In the devices realized by drop-casting the transfer curves were acquired polarizing the devices with a drain-to-source voltage  $V_D$  of -5V for saturation regime, and -0.2V for linear regime, and sweeping the gate-to-source voltage  $V_G$  from 5V to -5V (forward and reverse). Among the devices realized by drop casting, only in one sample  $V_G$  swept from 3V to -3V. For the device realized by drop-casting, however is not possible to individuate a saturation region, because their drain current  $I_D$  did not saturate.

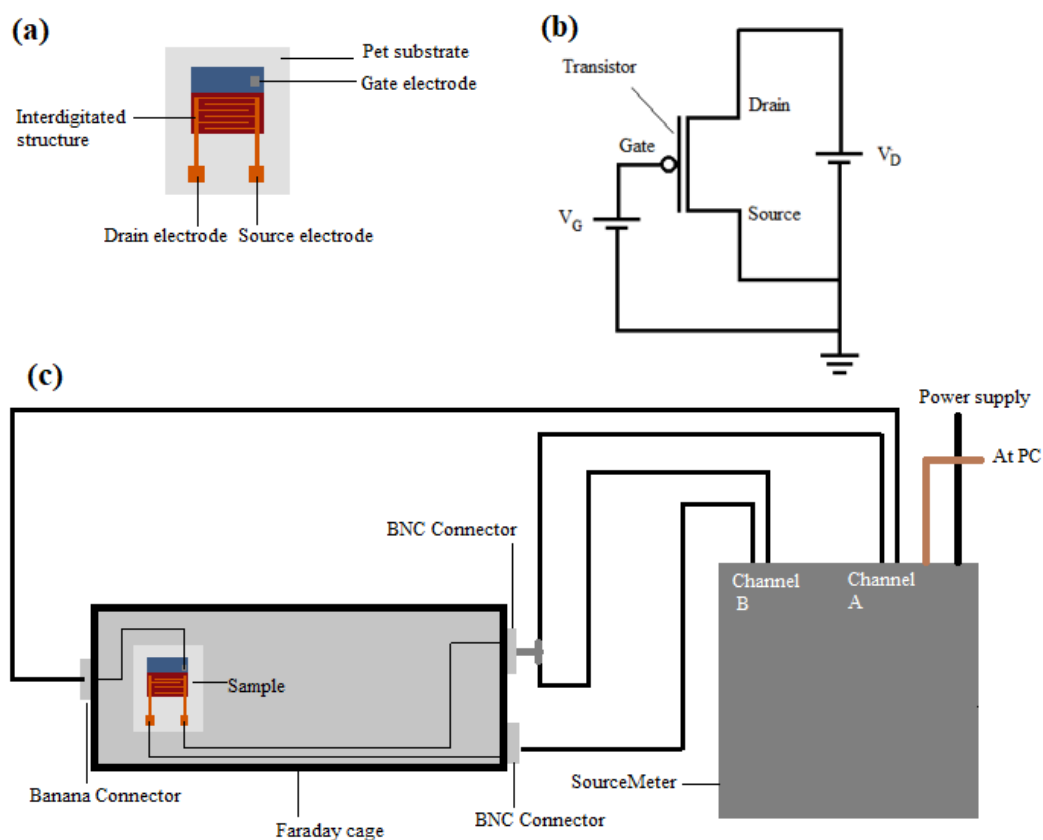


**Figure 3.6:** (a) Schematic view of one device. (b) Electric diagram of the connections realized in order to characterize the devices, represented by the transistor. (c) Schematic view of the experimental setup for electrical characterization. The Faraday cage is shown open.

In order to acquire the Output curve,  $V_G$  was maintained fixed respectively at 5V, 3V, 1V, 0V, -1V, -3V, -5V, while  $V_D$  swept from 0V to -5V. All these measurements were acquired with a delay time of 500 ms and a step of 0.1V. In the devices realized by spin-coating the transfer characteristics were acquired sweeping  $V_G$  from 0V to -3V (forward and reverse) and applying a drain-to-source voltage of -0.2V for linear region and of -3V for saturation region. Output characteristic was acquired fixing the gate-to-source voltage respectively at 5V, 3V, 1V, 0V, -1V, -2V, -3V, -5V, and sweeping  $V_D$  from 0V to -4V. In some initial measurements  $V_G$  was fixed at additional other value, however inside of the range indicated. Also these measurements were acquired with a delay time of 500 ms and a step of 0.1V.

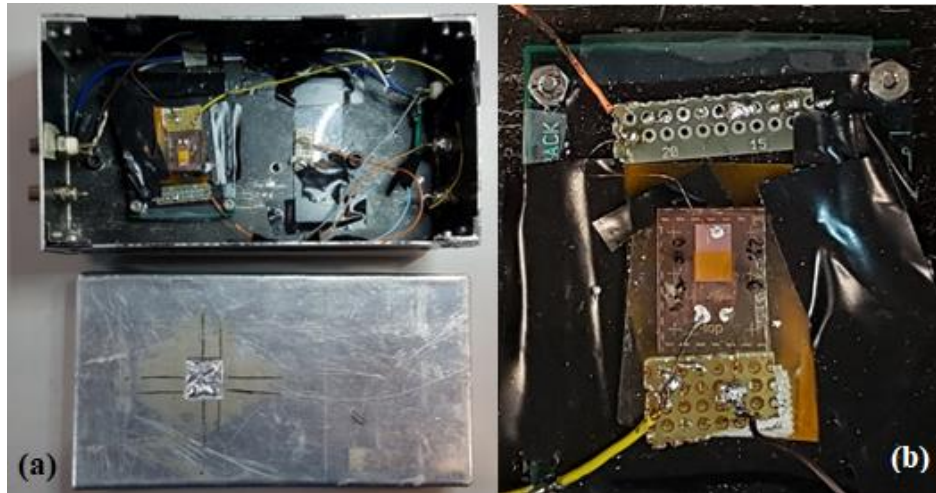


**Figure 3.7:** (a) The Faraday cage open with the sample is installed. (b) The sample inside the Faraday cage

### 3.3. X-Ray photoresponse characterization

The devices characterization under X-rays was performed using the dual channel Keithley 2614B SourceMeter and the custom made Labview software, already used for electrical characterization, with the same electrical connections described in the paragraph 3.2 and depicted in Figure 3.6. In addition, the metal Faraday cage was placed within a shielded area, containing also the X-ray tube (Figure 3.8 and 3.9). The X-ray tube is equipped with a shutter, that can be opened from the control unit manually or automatically, also by setting on/off cycles.

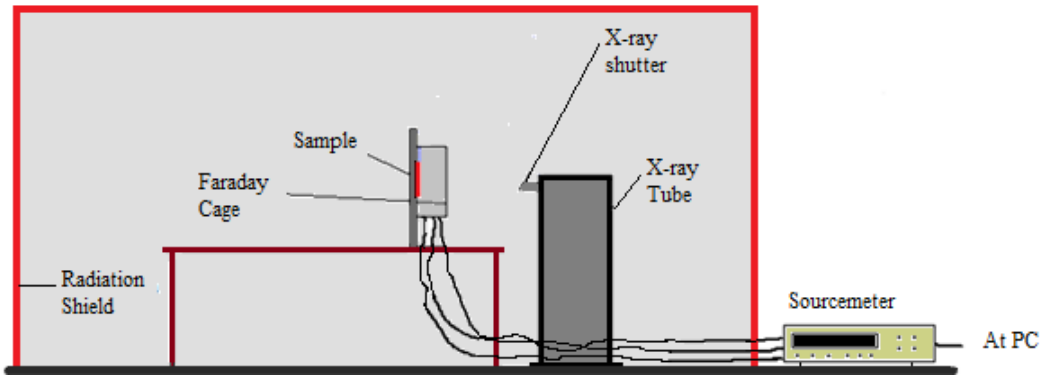


**Figure 3.8:** Schematic view of the experimental setup for characterization under X-ray.

In Figure 3.9 is reported a picture of the experimental setup, within the shielded area. It is possible to notice the Faraday cage with its connection cables and the X-ray tube.

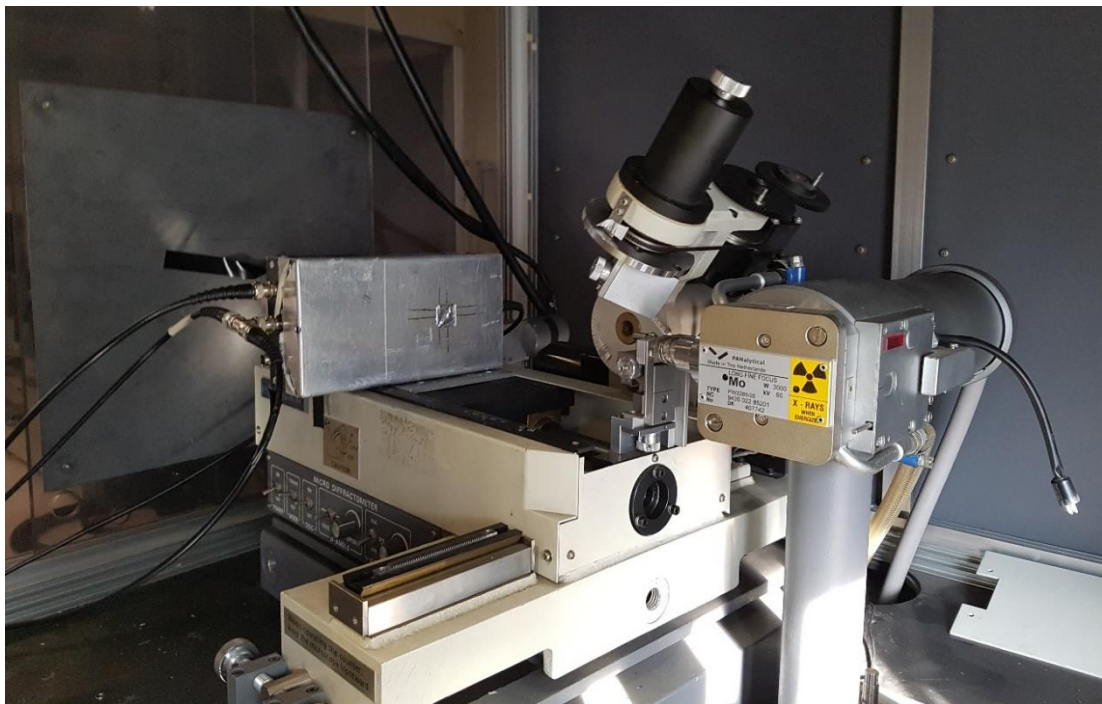


**Figure 3.9:** Picture of the experimental setup for sample characterization under X-ray.

The X-ray tube is a Mo-tube ( $K_{\alpha}=17.5$  keV [67], model PANalytical2 PW 2285/20), which operates at a voltage of 35 kV and at the current defined by the user in the range 5 mA ÷ 30 mA. Its spectrum is reported in Figure 3.10.

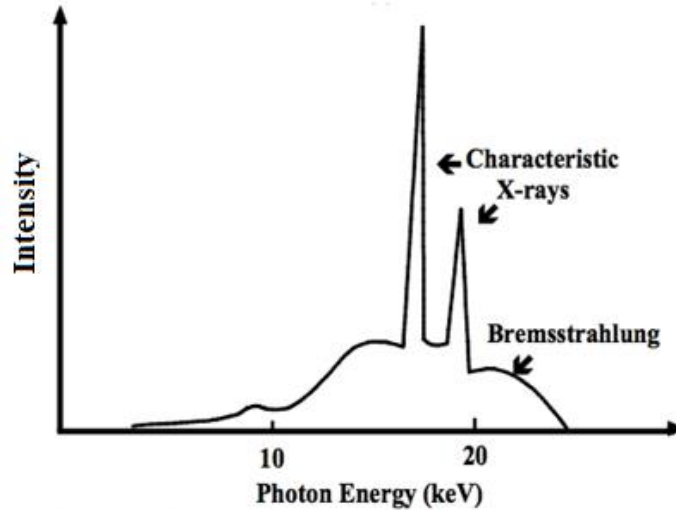


Figure 3.10: Spectrum of Mo-target X-ray tube [68].

The X-ray Mo-tube was fixed at the distance of 33 cm from the studied device, that was irradiated with X-ray beams having different dose-rate, varying from 30 mGy/s to 5 mGy/s (30 mGy/s, 20 mGy/s, 10 mGy/s and 5 mGy/s). For each dose-rate the drain current of the transistor ( $I_D$ ) was acquired during a cycle of four irradiation of 60 s, each one followed by 60 s without X-ray beam. For the transistors realized by spin-coating, this acquisition occurred when the devices were polarized in saturation regime ( $V_D=-3V$ ,  $V_G=-2$ ), where the X-ray induced photocurrent and the sensitivity resulted higher and the response was more reproducible. However, in case of a dark current too high, that covered the signal, these measurements were carried out at other polarization, that were then replicated in the devices in which a comparison of the results was necessary (for example, the samples realized from solutions of the two molecules at same concentration). On the contrary, the devices realized by drop-casting were characterized under X-rays when they were polarized in linear zone, at  $V_D=-0.5V$  and  $V_G=-1V$ , because only at this bias a response was observed. The Mo X-ray tube was previously calibrated on dose-rate employing the *Barracuda* radiation detector (RTI Group, Sweden, Figure 3.11). In this procedure (Figure 3.12a), the *Barracuda* probe was fixed at the radiation shield side, and the X-ray tube was powered at 35 kV and respectively 30 mA, 25 mA, 20 mA, 15 mA, 10 mA, 5 mA. For each current of the X-ray tube the corresponding dose-rate was measured. Then it was recalculated for the sample-tube distance by means of the equation (3.2):

$$D_r = D_{rp} \frac{r_p^2}{r_s^2} \quad (3.2)$$

Where  $D_r$  is the dose-rate impinging the sample,  $D_{rp}$  the dose-rate at *Barracuda* probe,  $r_p$  the distance *Barracuda* probe-X-ray tube and  $r_s$  the distance sample-X-ray tube.



**Figure 3.11:** *Barracuda* dose-rate detector. The probe is on the right side [69]

In order to have another detector which calibrates the X-ray tube, a Si-photodiode, that has a linear response to X-ray radiation, was calibrated by means of the *Barracuda* detector, measuring with the Keithley 2614B SourceMeter the photodiode current during irradiation at same condition of previous tube calibration and with an applied voltage of -2V. The photodiode was installed in the Faraday cage, and shielded from visible light. The experimental setup is reported in Figure 3.12b. A 5% error was associated to each value, in both calibrations. This relative percent error was estimated taking into account the statistical error, the SourceMeter error, and the distance measurements error.

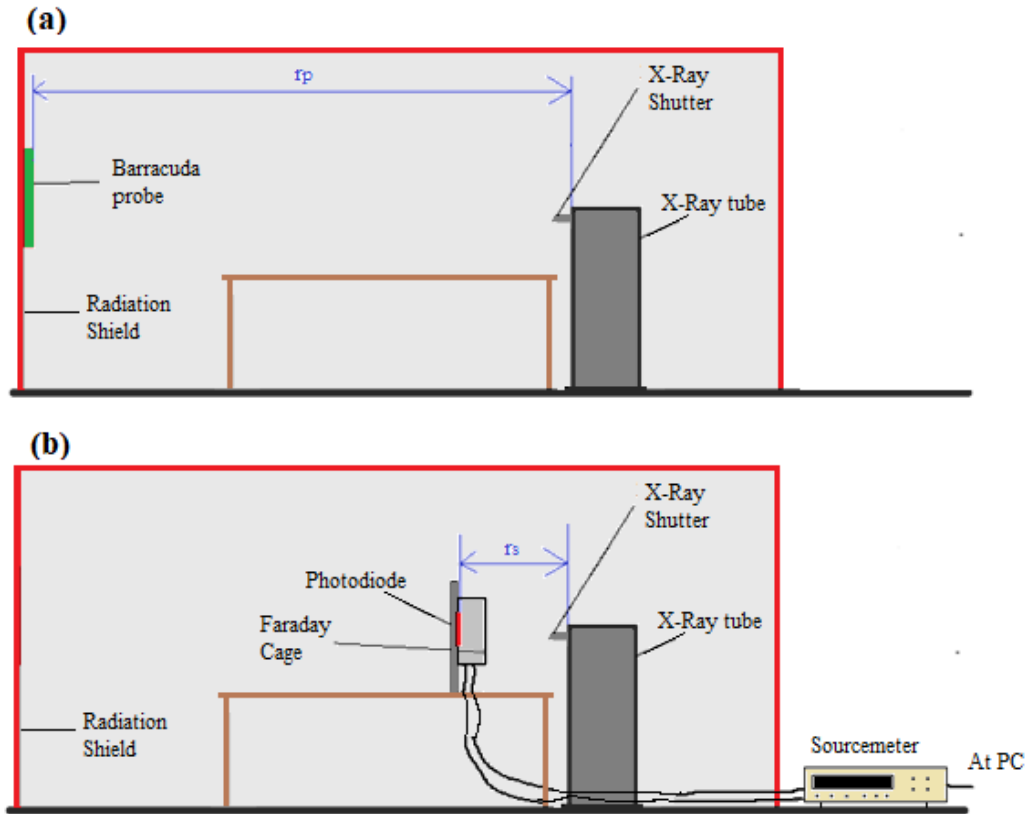


**Figure 3.12:** Experimental setup for the calibration of the X-ray tube (a), and the photodiode (b).

The tables 3.3a and b, and the plots in Figure 3.13 and 3.14 show the calibration results. In the case of the Mo-tube, the current  $I$  indicates the current of the X-ray tube, and in the plot this current is reported as a function of the dose-rate measured by the *Barracuda* probe rescaled for the sample-tube distance ( $D_{re}$ ). It is possible to notice that the relation between the tube current and the dose-rate generated is linear. In Table 3.3b and in the plot in Figure 3.14  $I_{ph}$  indicates the current of the photodiode (biased at -2V) and the dose-rate  $D_{re}$  is the one measured by the *Barracuda*, rescaled to the distance of the photodiode (that is the sample distance), with the equation (3.2). The results indicate that the photodiode has a linear X-ray irradiation response.

(a)

$I(\text{mA})$	$D_{re}(\text{mGy/s})$
30	$30 \pm 1$
25	$24 \pm 1$
20	$20 \pm 1$
15	$14.5 \pm 0.7$
10	$10.2 \pm 0.5$
5	$4.6 \pm 0.2$

(b)

$I_{ph}(\text{A})$	$D_{re}(\text{mGy/s})$
$7.00 \cdot 10^{-9}$	$30 \pm 1$
$5.90 \cdot 10^{-9}$	$24 \pm 1$
$4.59 \cdot 10^{-9}$	$20 \pm 1$
$3.51 \cdot 10^{-9}$	$14.5 \pm 0.7$
$2.40 \cdot 10^{-9}$	$10.2 \pm 0.5$
$1.19 \cdot 10^{-9}$	$4.6 \pm 0.2$

**Tables 3.3:** Calibration of Mo-tube (a) and of Si-photodiode (b).

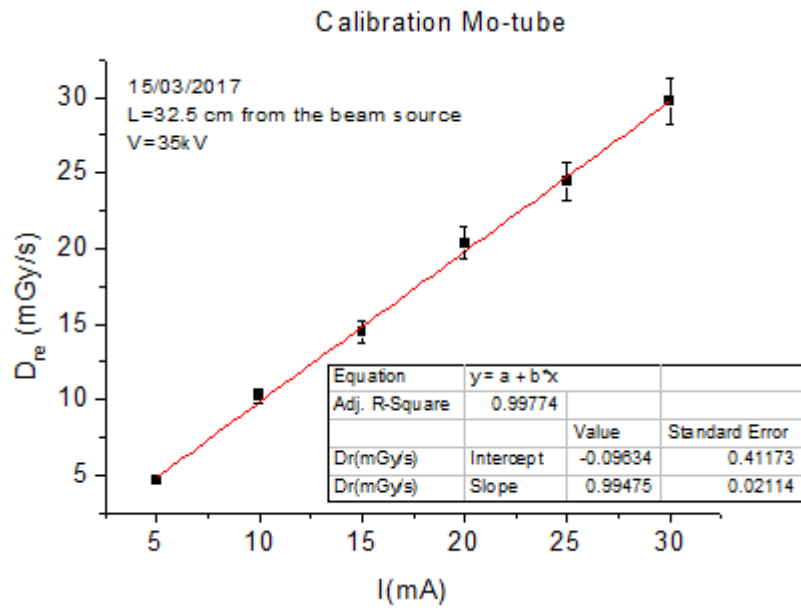


Figure 3.13: Calibration of Mo-tube.

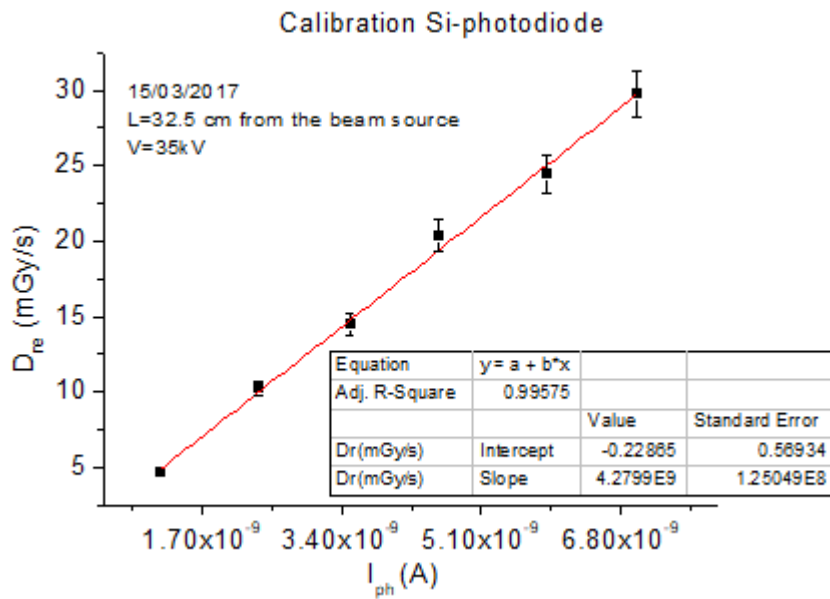


Figure 3.14: Calibration of Si-photodiode as X-ray detector

### 3.4. Data Analysis

Charge carrier mobility, transistor threshold voltage and  $I_{on}/I_{off}$  ratio were extracted in saturation regime, using equation (1.8) reported also below, that provides a plot of the square root of the saturation drain current  $(I_D)_{sat}$  vs gate voltage ( $V_G$ ), that results in a straight line (Figure 3.15). The following equation (3.3) is the (1.8):

$$\sqrt{(I_D)_{sat}} = \sqrt{\frac{W}{2L}} C_i \mu (V_G - V_T) \quad (3.3)$$

Knowing the slope of this line, the capacitance per unit area of dielectric layer  $C_i$  (18 nF/cm<sup>2</sup>), and the width and length channel of the transistor (respectively 50 mm and 45  $\mu$ m), it is possible to obtain the mobility, whereas the extrapolation of this line to zero current is the threshold voltage.

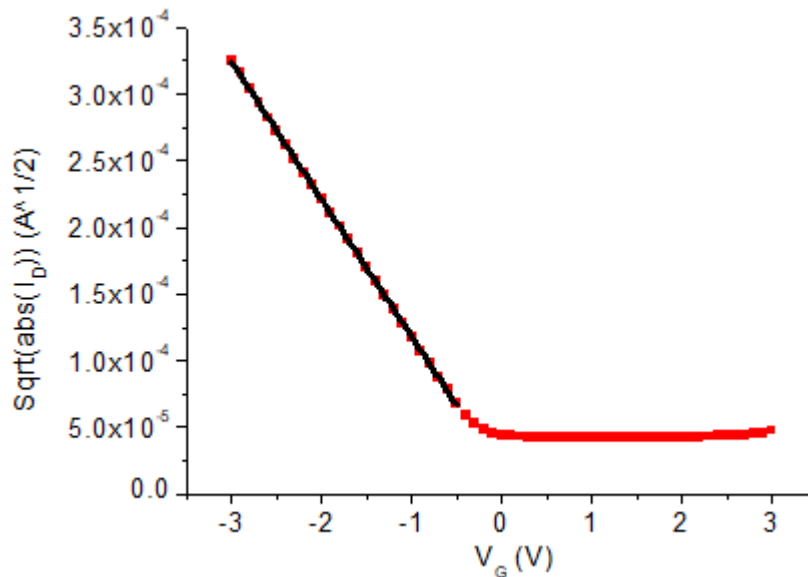


**Figure 3.15:** Square root of drain current reported as a function of  $V_G$  in saturation regime. The fit line that compares in this plot is the one obtained in the equation (3.3)

The  $I_{off}$  was assessed by fitting, in the transfer characteristic graph in saturation regime, the segment in which the device is in the off-state as a line. In this way, the  $I_{off}$  is the intercept of this fit line. In order to individuate more precisely the off-state, at the y-axis ( $I_D$ ) of the graph a logarithmic scale was applied. The  $I_{on}$  was instead evaluated as the

maximum (in absolute value) of the drain current reached by the device. These two values allow to find the  $I_{on}/I_{off}$  ratio.  $I_{on}$  and the fit line used to find  $I_{off}$  are depicted in Figure 3.16. Each parameter described above was calculated in forward curve, and, again, a 5% error was associated to them.

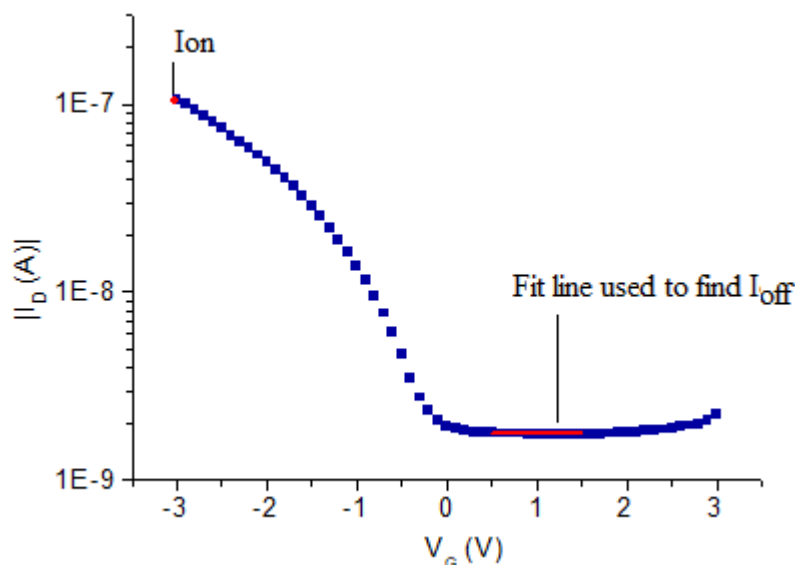


**Figure 3.16:** Calculation of  $I_{on}/I_{off}$  ratio. This plot shows the absolute value of the drain current as a function of the gate-to-source voltage.  $I_{on}$  and the fit line that allows to find  $I_{off}$  are indicated. The y-axis has a logarithmic scale.

The data acquired under X-ray irradiation were processed subtracting the dark current, in order to have a clear view of the photocurrent response. In almost all the devices analysed the dark current shows a drift that have an exponential decay behaviour, represented in the plot  $I_D$  vs time in figure 3.17a with black lines. Therefore, four points in the plot  $I_D$  vs time (Figure 3.17a) before any irradiation (approximately 0 s, 120 s, 240 s, 360 s) and one last point at the end of the cycle (about 480 s) were used to fit the dark current trend. In this way, it was possible to subtract the contribution of the dark current to the drain current  $I_D$ , obtaining thus the photocurrent (Figure 3.17b).

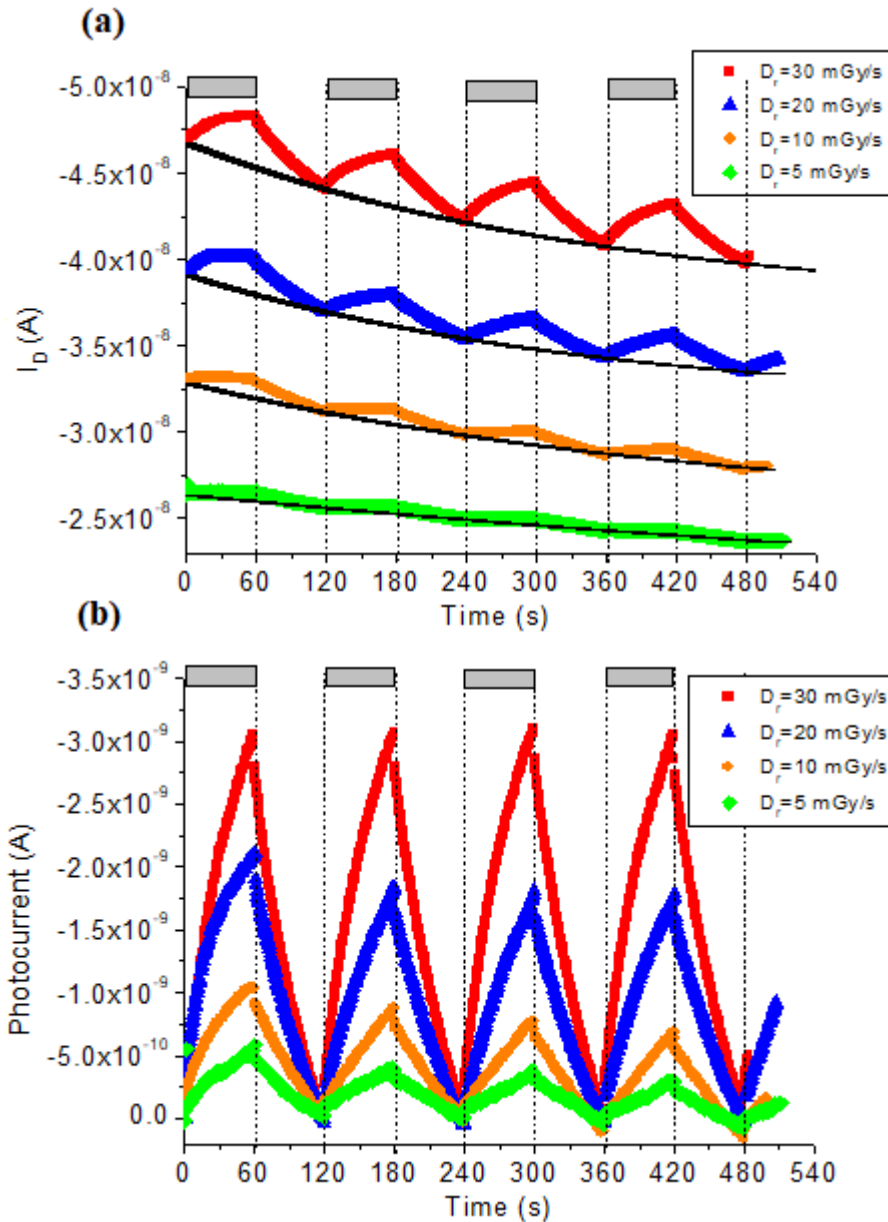


**Figure 3.17:** (a) Raw data acquired in photocurrent measurements. The black lines are the exponential fit of the dark current for each dose-rate, while the coloured lines represent the drain current  $I_D$  acquired during the measurements. (b) Photocurrent signal for each dose-rate  $D_r$  tested, obtained from the subtraction of the exponential contribution of the dark current to the drain current  $I_D$ . In both plots, the grey rectangles indicate the periods of time when the X-ray shutter is open and therefore the sample is irradiated.

The detector sensitivity was calculated as the slope of the linear fit found in the photocurrent vs dose-rate plot (Figure 3.18), and the error on the sensitivity corresponds to the error on the slope of the linear fit given by the software used to fit. For each dose-

rate, in the graph photocurrent vs dose-rate was reported the mean value of the photocurrent, obtained from the last three peaks of any irradiation cycle (the first peak normally is higher than the others), subtracting the current at starting point of the peak to the peak value. Finally, the sensitivity per unit volume (specific sensitivity) is calculated by dividing the sensitivity to the active area ( $L \times W$ ) and the thickness, the latter evaluated by AFM (Atomic Force Microscopy, model Park NX10 using PPP-NCHR tips) analysis by another member of the research group. For AFM thickness measurements, a 10% error was associated to each value. The sensitivity uncertainty is the statistic error calculated in fitting operation, whereas the specific sensitivity error was calculated by quadrature sum of initial uncertainty.

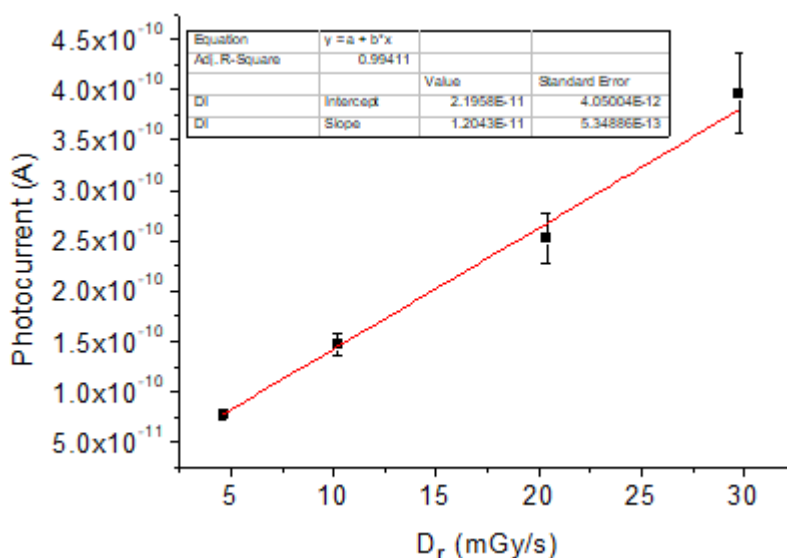


**Figure 3.18:** Example of sensitivity calculation: The slope of the straight line in the graph photocurrent vs dose-rate represents the sensitivity.

The error associated to the average values of the parameters presented in the following chapters is the maximum semi dispersion:

$$\Delta x = \frac{x_{\max} - x_{\min}}{2} \quad (3.4)$$

Where  $\Delta x$  is the error associated to the average value of the variable  $x$ . This choice was necessary because the devices of the same type that had a good response were at most 6, and their parameters were quite disperse. Therefore, it was not possible to imagine these distributions as gaussian and to assume the standard deviation as uncertainty.

## 4. Results and discussion

In this chapter, the results obtained employing the transistors realized with diF-TES-ADT and diF-TEG-ADT as X-ray detectors are presented and discussed. The paragraphs are subdivided referring to the deposition technique and the concentration of the starting solution. In the transfer characteristics plots the arrows indicate the direction of the scan (reverse or forward), and the drain current  $I_D$  is reported in logarithmic scale, therefore its absolute value is showed. In the plots photocurrent vs dose-rate ( $D_r$ ) the grey rectangles indicate the periods of time in which the shutter of the X-ray tube is open, and therefore the sample is irradiated. The plots of the leakage current in saturation regime, that is the current that flows across the gate electrode, which ideally should be zero, and the plots of the drain current  $I_D$  acquired under irradiation are reported in the appendix. The Table 4.1 shows the number of devices fabricated per molecule type, deposition technique and concentration of the starting solution.

Molecule	Deposition technique	C (wt %)	N° Samples
diF-TES-ADT	Drop-casting	0.5	4
diF-TEG-ADT	Drop-casting	0.5	4
diF-TES-ADT	Spin-coating	1.2	11
diF-TEG-ADT	Spin-coating	1.2	10
diF-TES-ADT	Spin-coating	0.5	7
diF-TEG-ADT	Spin-coating	0.5	2
diF-TES-ADT	Spin-coating	2	3
diF-TEG-ADT	Spin-coating	2	6

**Table 4.1:** Number of samples (N° Samples) fabricated per molecule type, deposition technique and concentration (C) of the starting solution.

## 4.1 Devices realized by drop-casting from solutions at wt.0.5%

### - Solution of diF-TES-ADT at wt.0.5%

Four samples of this kind were fabricated by drop-casting from a solution in chlorobenzene of diF-TES-ADT at wt.0.5%, but only two demonstrated to work properly under X-rays as detectors. In Figure 4.1 a picture of the active layer of a typical device of this kind is depicted. It is possible to notice the semiconductor deposited over the interdigitated structure.

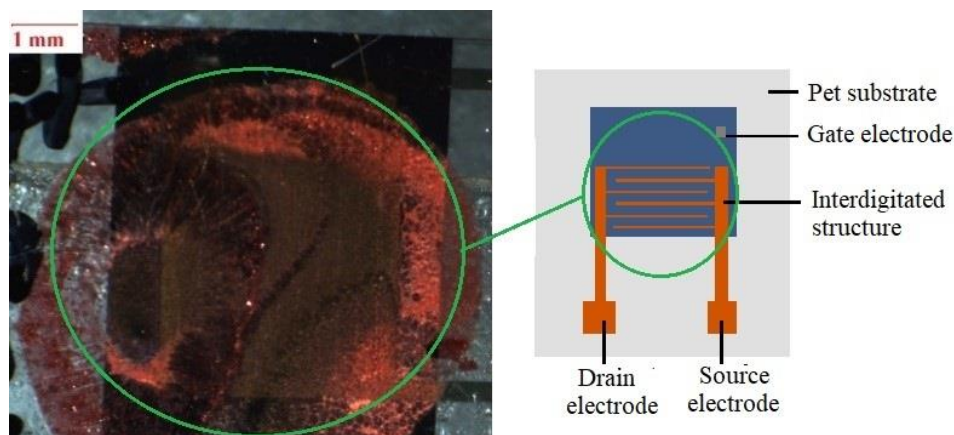


**Figure 4.1:** zoom over the active layer of a typical device realized by drop-casting from a solution of diF-TES-ADT at wt.0.5% in chlorobenzene. It is possible to notice the semiconductor deposited over the interdigitated structure. On the right a schematic view of the OTFT structure is shown.

The measurements indicate a quasi-transistor behaviour that does not allow to calculate characteristics parameters (mobility, threshold voltage and  $I_{on}/I_{off}$  ratio). The output characteristics (Figure 4.2c and d) indicate that these devices do not reach the saturation zone, however the maximum drain current acquired during a  $V_G$  scan at  $V_D = -5V$ , that should correspond to the saturation region (Figure 4.2b), is respectively about  $1 \cdot 10^{-5}$  A and  $8 \cdot 10^{-7}$  A and after X-ray exposition it does not change appreciably. Slightly lower values were obtained for the transfer curve in linear zone (Figure 4.2a). The leakage current observed is low ( $\approx 10^{-10}$  A, Figure A.1 in appendix).

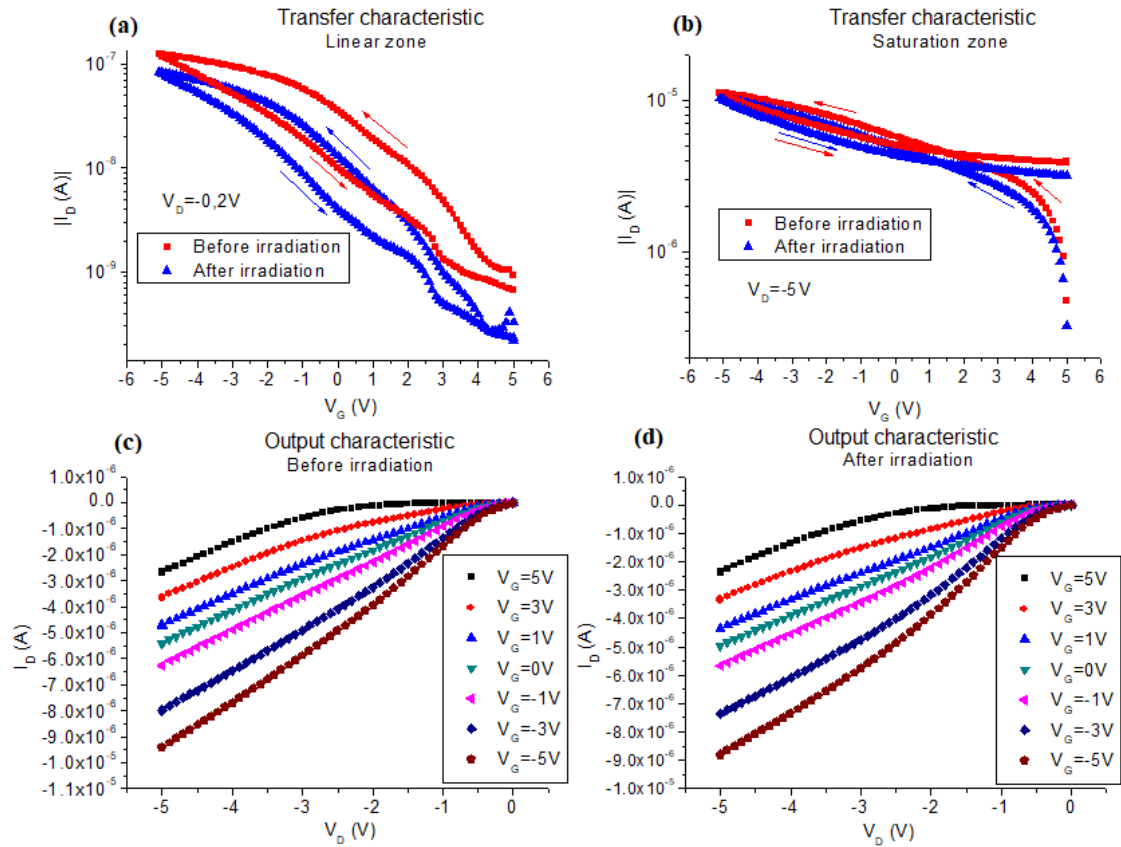


**Figure 4.2:** Electrical characterization of a typical device realized by drop-casting from a solution of diF-TES-ADT at wt.0.5% in chlorobenzene: (a) Transfer characteristic in linear regime (b) Transfer characteristic in the region that should be of saturation. (c) Output characteristic before the irradiation. (d) Output characteristic after the irradiation.

Although the transfer characteristics and output characteristics measurements are not optimal, the devices were characterized under X-ray irradiation, and the sensitivity was evaluated. One of the sample characterized, biased at  $V_D = -0.5V$  and  $V_G = -1V$ , that is the larger polarization at which a response is observed, shows a dark current of about  $10^{-8}$  A, whereas the signal has a value of about  $10^{-9}$  A. On the contrary, the second sample characterized at the same bias shows a better behaviour under X-rays, even if the peaks of photocurrent induced under irradiation are not very reproducible, as shown in Figure 4.3a. The dynamic of the response (Figure 4.3a) is faster for the doses-rate of 20 mGy/s and 30 mGy/s: in these two cases the drain current  $I_D$  saturates in roughly 20 s. The recovery appears similar for all the dose-rates and the signal shape is a not properly perfect sawtooth. The sensitivity of this sample reaches a value of  $(25 \pm 4)$  nC/Gy. In Figure 4.3b its linear zone as a function of the dose-rate is showed.

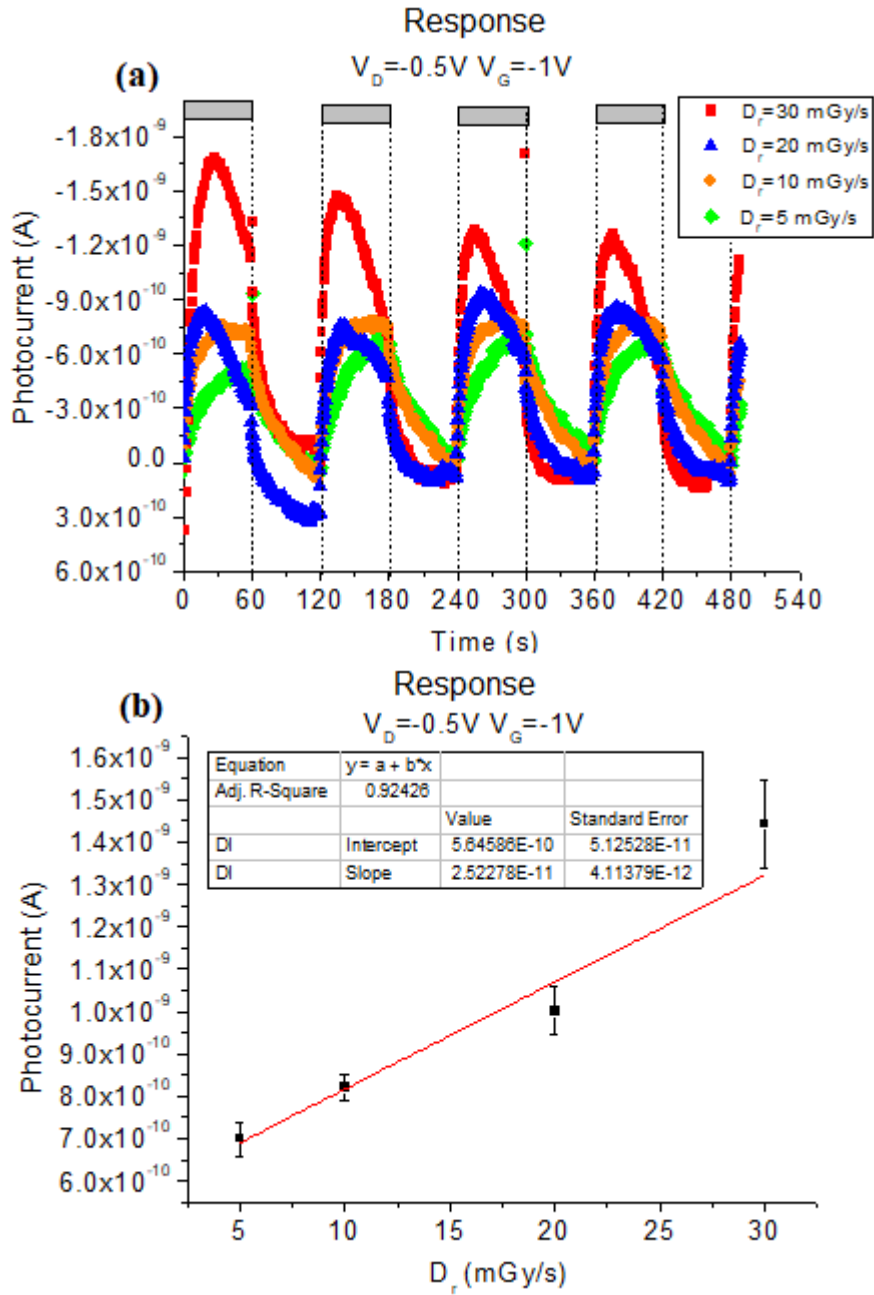


**Figure 4.3:** X-ray response of a typical device realized by drop-casting from a solution of diF-TES-ADT at wt.0.5% in chlorobenzene biased at  $V_D = -0.5V$  and  $V_G = -1V$ : (a) Photocurrent vs time plot for four X-ray irradiation cycles having different dose-rates. (b) Photocurrent vs dose-rate plot.

#### - Solution of diF-TEG-ADT at wt.0.5%

Four samples of this kind were fabricated by drop-casting from a solution in chlorobenzene of diF-TEG-ADT at wt.0.5%, but only two demonstrated to work under X-rays. In Figure 4.4 a picture of the interdigitated structure, covered by the semiconductor, of a typical device of this kind is depicted.

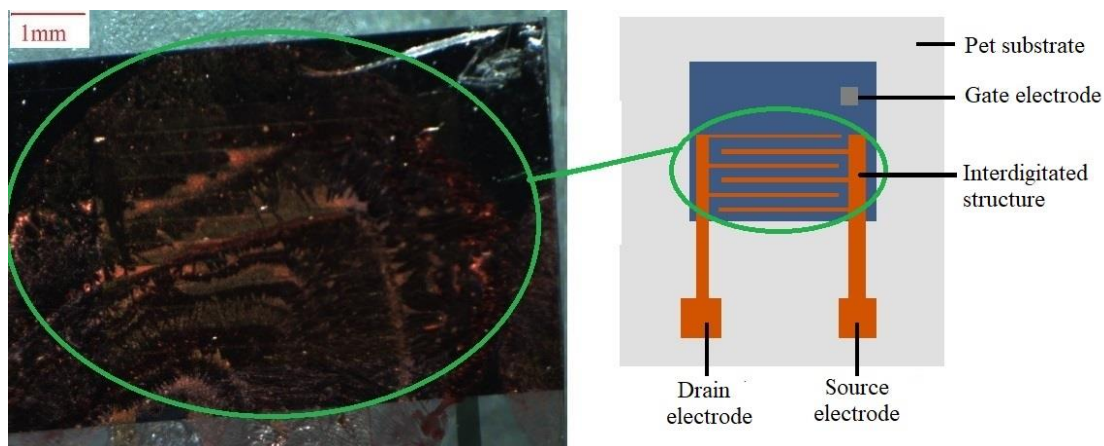


**Figure 4.4:** zoom over the active layer of a typical device realized by drop-casting from a solution of diF-TEG-ADT at wt.0.5% in chlorobenzene. It is possible to notice the semiconductor deposited over the interdigitated structure. On the right a schematic view of the OTFT structure is shown.

These samples do not show a good transistor-like behaviour and this fact excludes the possibility of calculation of characteristic parameters. The output characteristics (Figure 4.5b and Figure 4.5c) put in evidence that also in these devices  $I_D$  does not saturate, however for both samples analysed, the maximum drain current reached in the region that should be of saturation is about  $10^{-5}$  A, and does not vary appreciably after irradiation (Figure 4.5b). This statement is valid also for  $I_D$  in linear regime (Figure 4.5a), even if its maximum value is about two orders of magnitude lower. For both regimes, it is difficult to find an off-state. The leakage current during the acquisition of  $I_D$  in the regime that should be of saturation has a value of about  $10^{-9}$  A (Figure A.3 in the appendix).

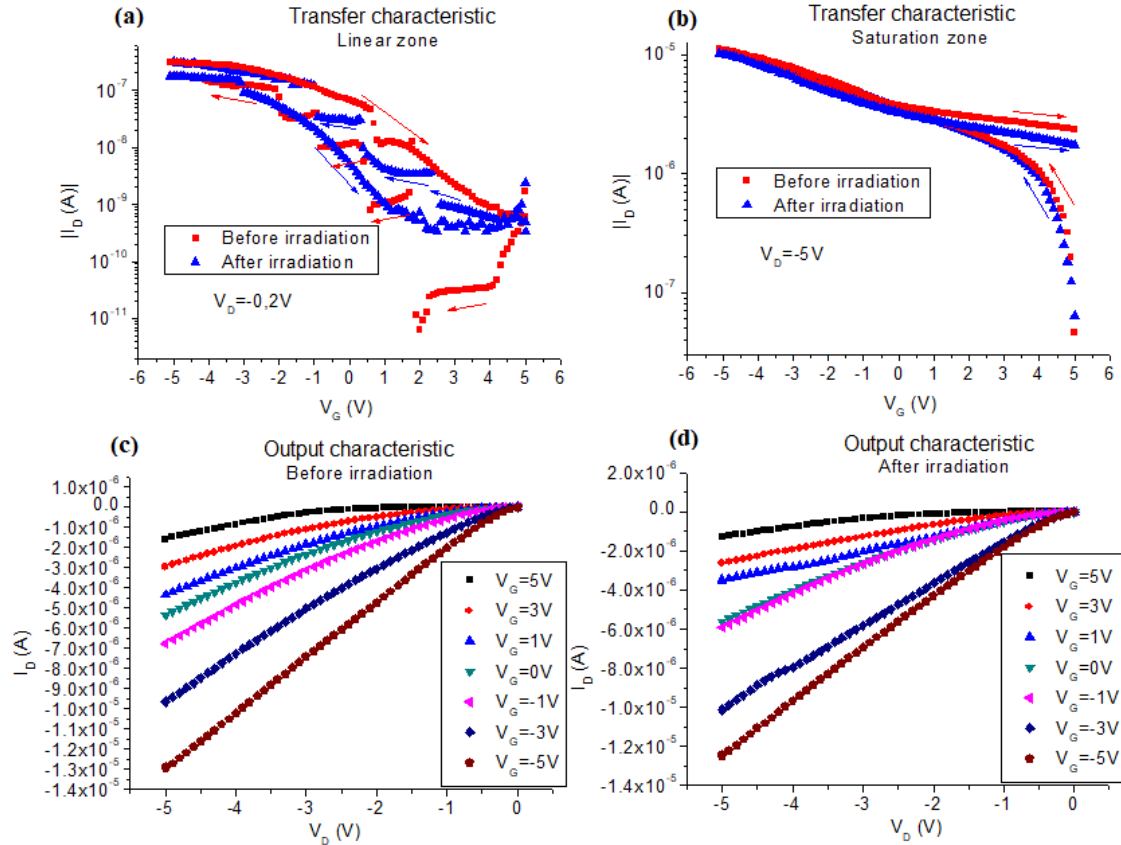


**Figure 4.5:** Electrical characterization of a typical device realized by drop-casting from a solution of diF-TEG-ADT at wt.0.5% in chlorobenzene: (a) Transfer characteristic in linear regime (b) Transfer characteristic in the region that should be of saturation. (c) Output characteristic before the irradiation. (d) Output characteristic after the irradiation.

Under X-rays these devices produce a response only when polarized at  $V_D = -0.5V$  and  $V_G = -1V$  (the plot of a typical response is in Figure 4.6a). With larger values of bias no response was observed. Irradiated at these biases, the samples produce a signal of about  $10^{-9}$  A. The reproducibility of the photocurrent peaks is low also in this case. The photocurrent response plotted as a function of the dose-rate (Figure 4.6b) demonstrates a linear trend, and the sensitivity recorded is up to  $(24 \pm 6)$  nC/Gy. Observing the plot in Figure 4.6a it is possible to notice that the response is characterized by a dynamic that slows as a reverse function of the dose-rate. On the contrary, the recovery after the irradiation appears more comparable for all the four dose-rates  $D_r$  investigated.

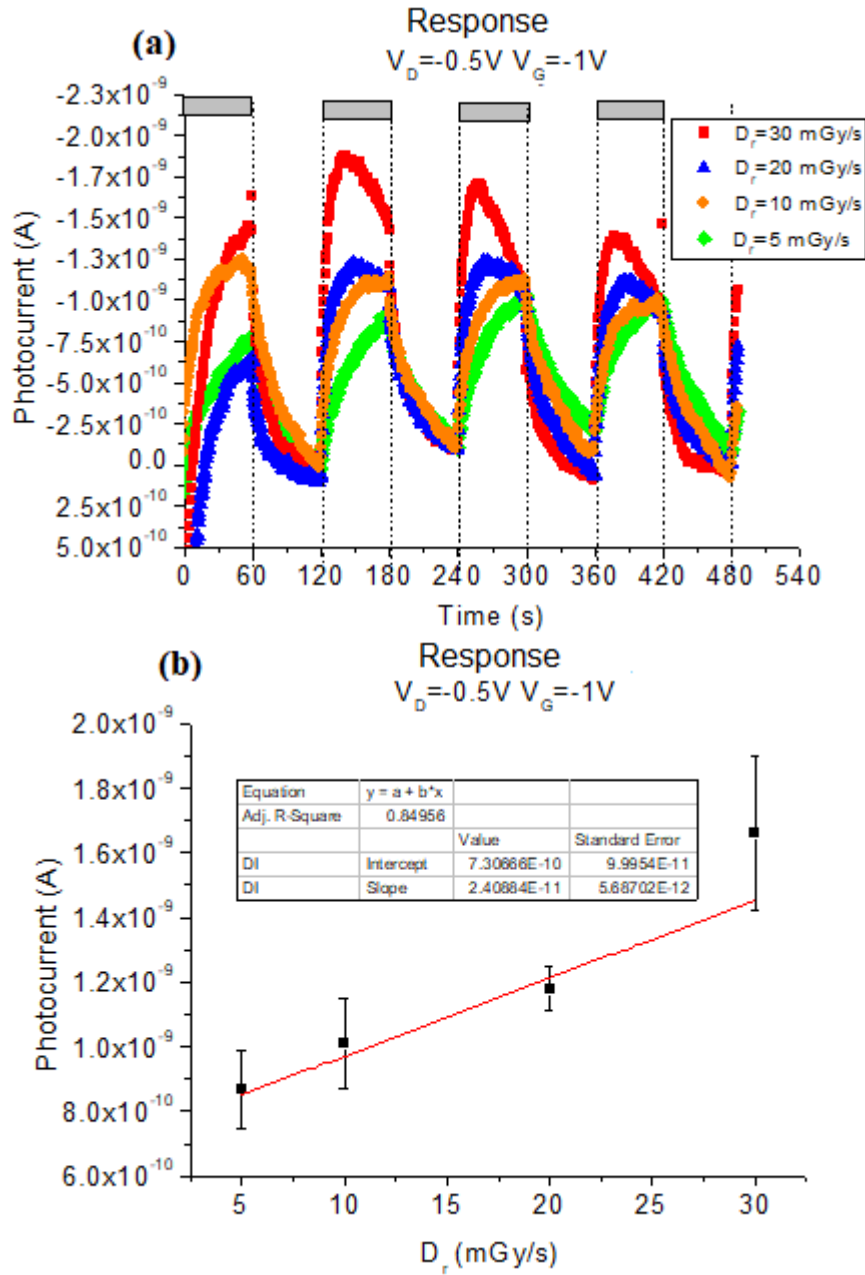


**Figure 4.6:** X-ray response of a typical device realized by drop-casting from a solution of diF-TEG-ADT at wt.0.5% in chlorobenzene: biased at  $V_D = -0.5V$  and  $V_G = -1V$ : (a) Photocurrent vs time plot for four X-ray irradiation cycles having different dose-rates. (b) Photocurrent vs dose-rate plot.

## 4.2 Devices realized by spin-coating from solutions at wt.1.2%

### - Solution at wt.1.2% of diF-TES-ADT

Eleven devices were realized by spin-coating from a solution at wt.1.2% of diF-TES-ADT, of which only five are working properly as X-ray detectors. They present, in general, a good transistor-like behaviour and a good response to the X-ray irradiation. In saturation region (polarized at  $V_D=-3V$  and  $V_G=-2V$ ) they show a reproducible response under irradiation, characterized by a linear dependence of the photocurrent with the dose-rate. In Figure 4.7 a picture of the active layer of a sample is shown. Here it is possible to notice the complete covering of the interdigitated OTFT structure of the semiconductor.

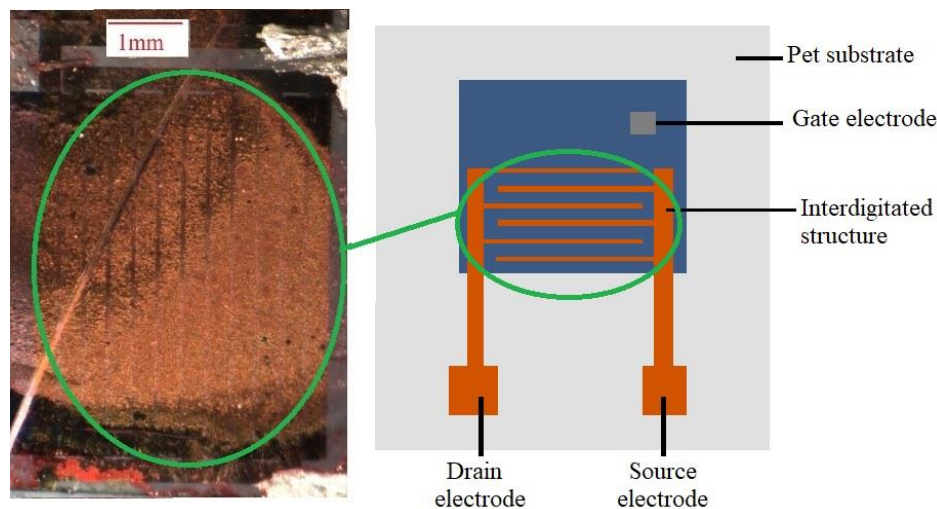


**Figure 4.7:** active layer of a typical device realized by spin-coating from a solution of diF-TES-ADT at wt.1.2% in chlorobenzene.

After the irradiation, the transistors present a lowering of the mobility  $\mu$  ( $\approx 4.8 \cdot 10^{-3} \text{ cm}^2/\text{Vs}$ ) and the threshold voltage  $V_T$  ( $\approx 2.3V$ ) as reported in table 4.2, due to the degradation of the devices under X-rays. On the contrary the  $I_{on}/I_{off}$  ratio remains constant. The leakage current recorded during the acquisition of the transfer characteristic in saturation regime has an average value of about  $10^{-10} \text{ A}$ . (Figure A.5 in the appendix). The Figure 4.8 presents a typical transfer characteristic in linear and

saturation regime, and a typical output characteristic, before and after the irradiation of one of these devices. It is possible to observe the field-effect transistor behaviour, though there is a small hysteresis.

$\mu$ (cm <sup>2</sup> /Vs)		$V_T$ (V)		$I_{on}/I_{off}$	
before X-rays	after X-rays	before X-rays	after X-rays	before X-rays	after X-rays
$(1.01 \pm 0.05) \cdot 10^{-2}$	$(5.3 \pm 0.3) \cdot 10^{-3}$	$2.6 \pm 0.1$	$0.26 \pm 0.01$	$(5.5 \pm 0.3) \cdot 10^2$	$(5.5 \pm 0.3) \cdot 10^2$

**Table 4.2:** Maximum value of characteristic transistor parameters before and after the exposition to X-rays for the devices realized by spin-coating from a solution of diF-TES-ADT at wt.1.2% in chlorobenzene.

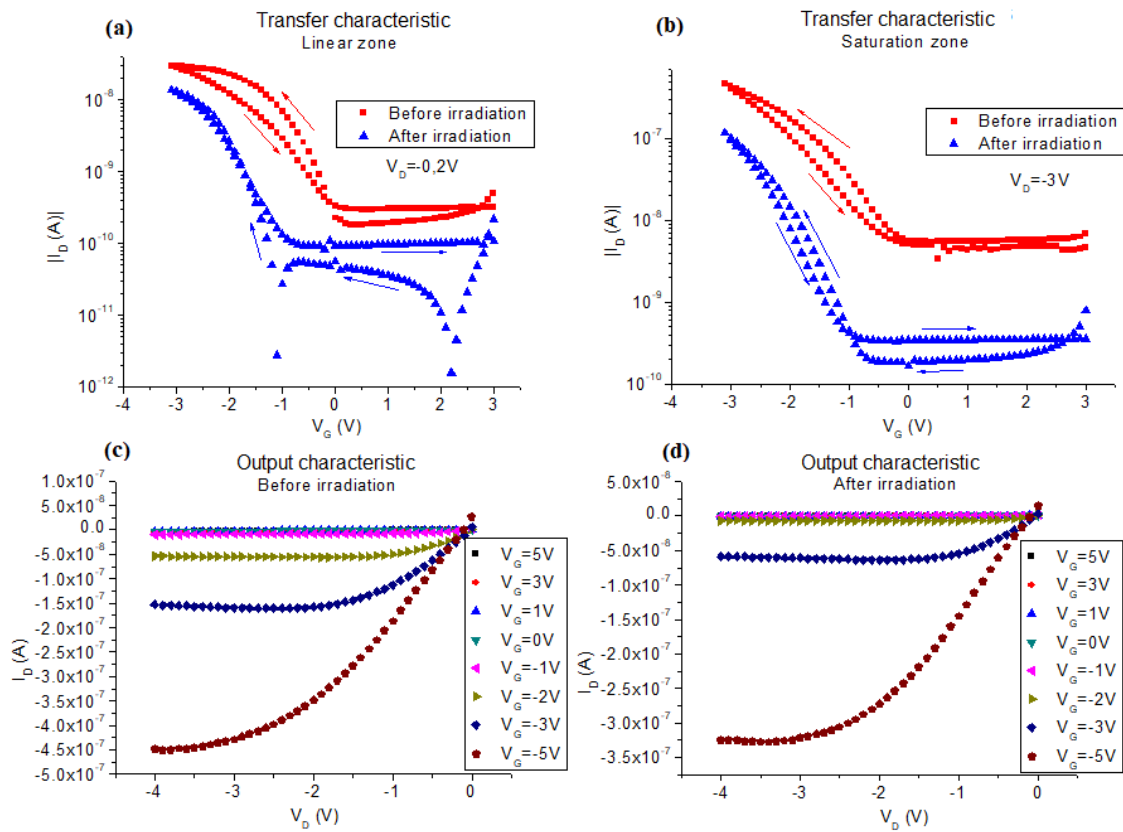


**Figure 4.8:** Electrical characterization of a typical device realized by spin-coating from a solution of diF-TES-ADT at wt.1.2% in chlorobenzene: (a) Transfer characteristic in linear regime (b) Transfer characteristic in saturation regime. (c) Output characteristic before the irradiation. (d) Output characteristic after the irradiation

When these devices are irradiated by the X-ray beam, and biased at  $V_D = -3V$  and  $V_G = -2V$ , they show a signal characterized by a certain noise (Figure 4.9a), probably due to the low current that constitutes the signal, that is of about  $5 \cdot 10^{-10}A$ . From the Figure 4.9a

it is possible to notice that the dynamic of the signal is similar for all the dose-rates investigated. The photocurrent signal has a sawtooth shape, and reaches its maximum value at the end of exposition. When the shutter is closed it starts to decrease. The graph in Figure 4.9b (photocurrent vs dose-rate  $D_r$ ) demonstrates the linearity of a typical response. The average sensitivity for these transistors is  $(19 \pm 7)$  nC/Gy, whereas the maximum sensitivity is  $(28 \pm 2)$  nC/Gy.

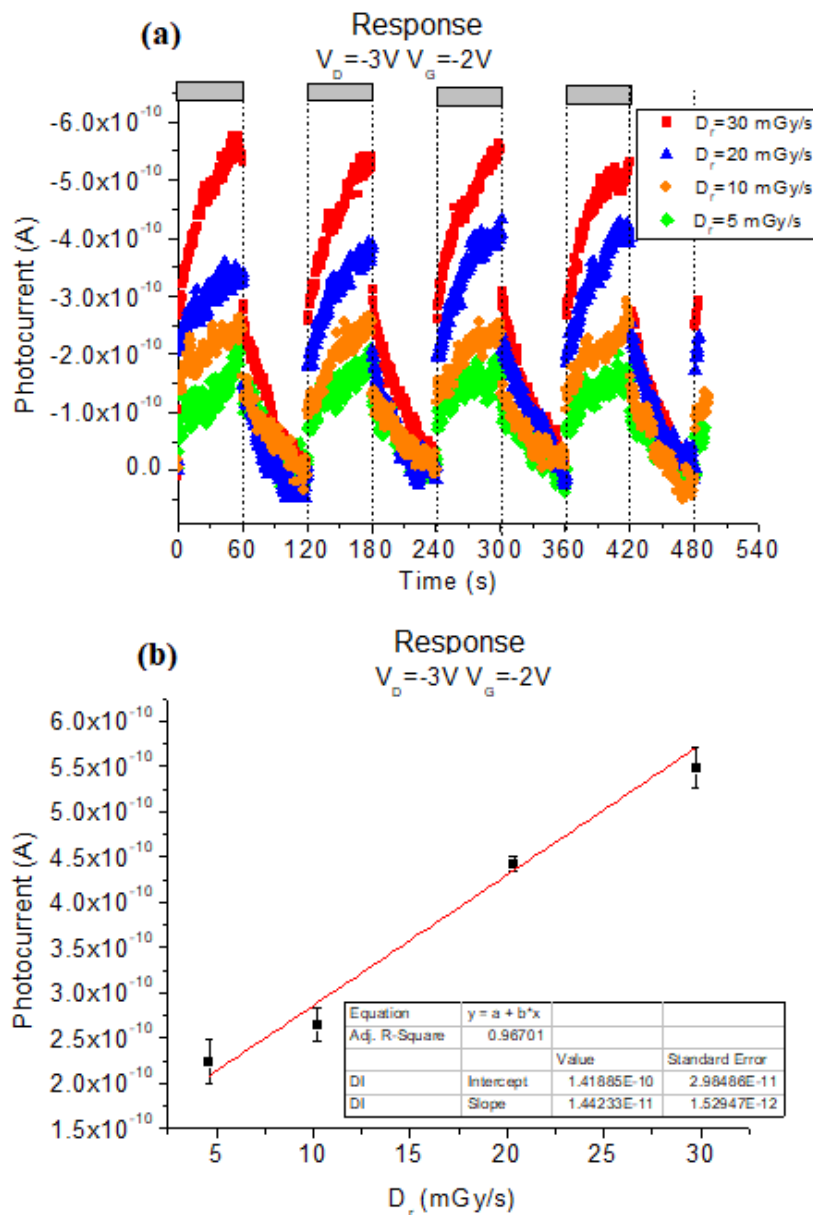


**Figure 4.9:** X-ray response of a typical device realized by spin-coating from a solution of diF-TES-ADT at wt.1.2% in chlorobenzene biased at  $V_D = -3V$  and  $V_G = -2V$ : (a) Photocurrent vs time plot for four X-ray irradiation cycles having different dose-rates. (b) Photocurrent vs dose-rate plot.

The AFM analysis (Figure 4.10) carried out by another member of the research group allowed to obtain the thickness of these samples, estimated as  $(1.2 \pm 0.1) \cdot 10^{-2}$  cm. Thanks to these measurements it is possible to calculate the specific sensitivity, that has a maximum value of  $100 \pm 10$  nC/mGy/cm<sup>3</sup>.

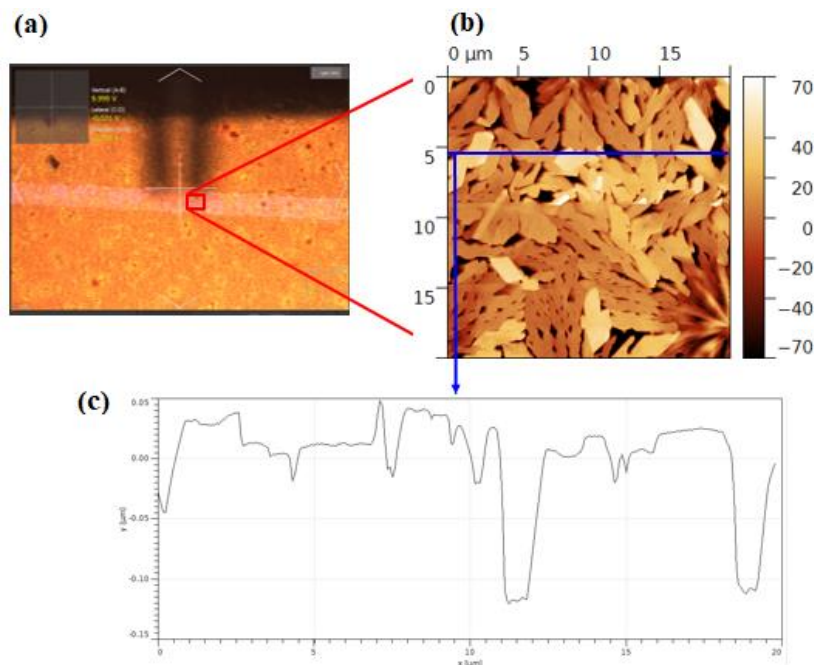


**Figure 4.10:** AFM Measurements of a device realized by spin-coating from a solution of diF-TEG-ADT at wt.1.2% in chlorobenzene. (a) Surface. (b) Zoom on the evidenced area of the surface. (c) Profile.

#### - **Solution at wt.1.2% of diF-TEG-ADT**

Ten devices were realized by spin-coating from a solution at wt.1.2% of diF-TEG-ADT, of which only six resulted properly working as X-ray detectors. They exhibit an excellent transistor transfer and output characteristics, thus clearly indicating that it is possible to use them as transistors. Under irradiation their behaviour was good: the photocurrent signal is characterized by a low noise and the peaks in photocurrent, induced when the samples are irradiated, are reproducible. The Figure 4.11 shows a picture of one device of this kind, where it is possible to see the active zone characterized by the interdigitated structure, covered by the semiconductor.

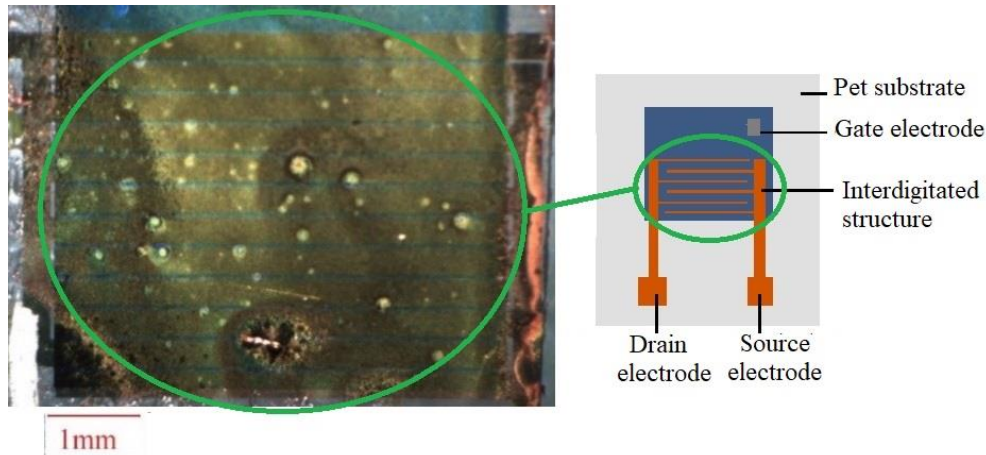


**Figure 4.11:** zoom over the active layer of a typical device realized by spin-coating from a solution of diF-TEG-ADT at wt.1.2% in chlorobenzene. It is possible to notice the interdigitated structure covered by the semiconductor.

A typical transfer characteristic acquired in linear regime is presented in Figure 4.12a. During the acquisition of the transfer characteristic in saturation regime (depicted in Figure 4.12b) these devices exhibit a maximum drain current ( $I_{on}$ ) of about  $10^{-5}$ - $10^{-6}$ A. A non reproducible behaviour of the  $I_{on}$  and  $I_{off}$  current after the irradiation (however  $I_{on}$  presents a decrement for all the samples) determines an absence of a trend for  $I_{on}/I_{off}$  ratio overall the devices. The maximum value of this parameter before and after the irradiation, together with the mobility  $\mu$  and the threshold voltage  $V_T$  are presented in Table 4.3. The leakage current recorded in saturation regime has an average value of about  $5 \cdot 10^{-10}$  A (Figure A.7 in the appendix). In the output characteristics, acquired before and after the exposition of the device to X-rays (Figure 4.12c and 4.12d)  $I_D$  saturates at  $V_D=-3$  and  $V_G=-2$ V as expected.

$\mu$ (cm <sup>2</sup> /Vs)		$V_T$ (V)		$I_{on}/I_{off}$	
before X-rays	after X-rays	before X-rays	after X-rays	before X-rays	after X-rays
$(7.7 \pm 0.4) \cdot 10^{-2}$	$(5.5 \pm 0.2) \cdot 10^{-2}$	$2.1 \pm 0.1$	$1.09 \pm 0.05$	$(1.09 \pm 0.06) \cdot 10^3$	$(3.2 \pm 0.2) \cdot 10^2$

**Table 4.3:** Maximum value of characteristic transistor parameters before and after the exposition to X-rays for the devices realized by spin-coating from a solution of diF-TEG-ADT at wt.1.2% in chlorobenzene.

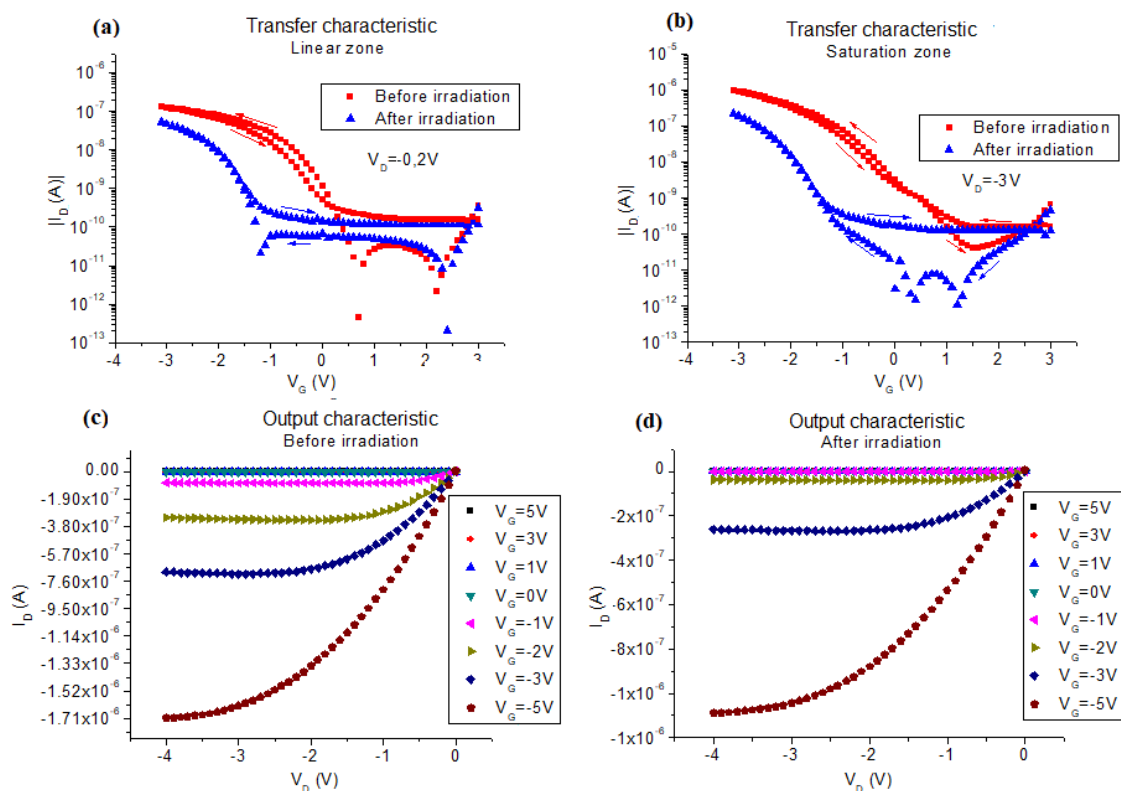


**Figure 4.12:** Electrical characterization of a typical device realized by spin-coating from a solution of diF-TEG-ADT at wt.1.2% in chlorobenzene: (a) Transfer characteristic in linear regime (b) Transfer characteristic in saturation regime. (c) Output characteristic before the irradiation. (d) Output characteristic after the irradiation

When these transistors (biased at  $V_D = -3V$  and  $V_G = -2V$ ) are irradiated by X-rays produce a good response characterized by a low noise (Figure 4.13a), especially in comparison with diF-TES-ADT wt.1.2% devices. Moreover, excluding the photocurrent peak due at the first irradiation, a good reproducibility is achieved, although for some samples at  $D_r = 5$  mGy/s it is not possible to acquire the photocurrent signal because it is too low. In these transistors the photocurrent signal has a value of about  $10^{-8}$  A-  $10^{-9}$  A, and the leakage current, at the bias applied for the characterization under X-rays, has an average value of approximately  $10^{-11}$  A. The dynamic of the response is uniform overall the devices of this type, and it is similar for all the dose-rates at which the samples were irradiated: the signal reaches its maximum at the end of exposition to the X-ray beam, and when the shutter is closed it decreases getting the dark current values before irradiation after 60 s, thus giving a sawtooth shape response. The plot in Figure 4.13b shows a typical response under irradiation. The average sensitivity is  $(200 \pm 300)$  nC/Gy, whereas the maximum sensitivity is  $(690 \pm 80)$  nC/Gy, both larger than the respective

sensitivities of the diF-TES-ADT wt1.2% devices. These transistors provide the best performance as X-ray detectors among all the devices realized during this experimental work. In fact, their average sensitivity is the highest, and their response is characterized by a low noise.

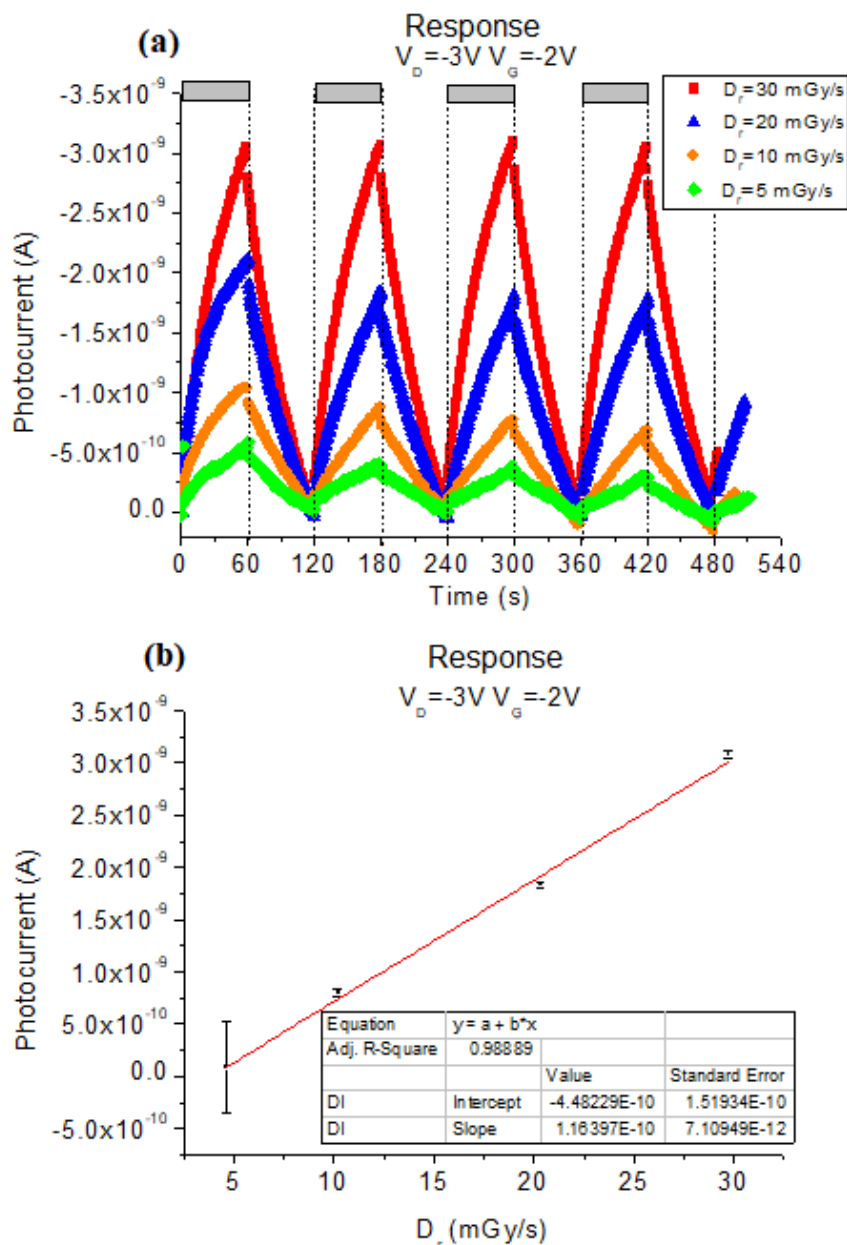


**Figure 4.13:** X-ray response of a typical device realized by spin-coating from a solution of diF-TEG-ADT at wt.1.2% in chlorobenzene biased at  $V_D = -3V$  and  $V_G = -2V$ : (a) Photocurrent vs time plot for four X-ray irradiation cycles having different dose-rates. (b) Photocurrent vs dose-rate plot.

The AFM measurements (Figure 4.14), carried out by another member of the research group, allowed to estimate the thickness of these transistors as  $(9\pm 1)\cdot 10^{-3}$  cm, so the maximum specific sensitivity is  $3400\pm 500$  nC/mGy/cm<sup>3</sup>.

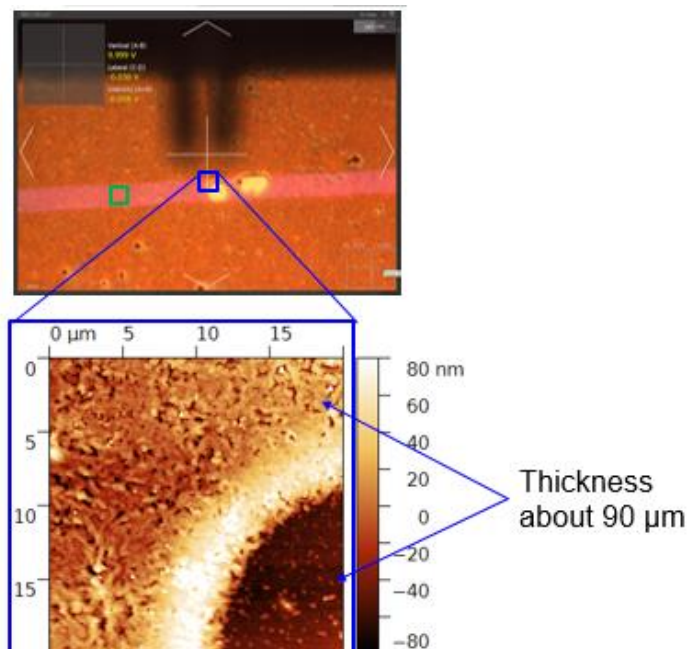


**Figure 4.14:** AFM Measurements of a diF-TEG-ADT wt.1.2% device: Surface and zoom on the evidenced area of the surface.

### 4.3 Devices realized by spin-coating from solutions at wt.0.5%

#### - Solution at wt.0.5% of diF-TES-ADT

Seven devices were fabricated by spin-coating from a solution of diF-TES-ADT at wt.0.5%, but only two resulted properly working as transistors. A picture of one of them is in Figure 4.15. It is possible to notice the source, and drain electrodes (covered by the silver paste), and the active zone, as indicated in the figure. These samples show a good transistor-like behaviour, exhibiting a very good transfer characteristic (depicted in Figure 4.16a and b), with a small hysteresis, reaching a maximum drain current  $I_D$  of about  $10^{-6}$ A in saturation zone, which after the irradiation has a decrement of about

$5 \cdot 10^{-7} \text{A}$  for both devices. In the output characteristics (Figure 4.16c and d)  $I_D$  clearly saturates at  $V_D = -3 \text{V}$  and  $V_G = -2 \text{V}$  as expected, and a good field-effect is present.

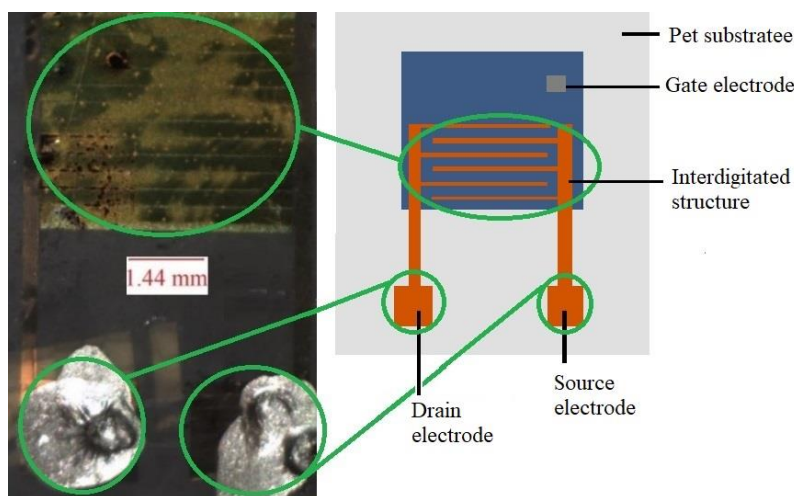


**Figure 4.15:** a typical device realized by spin-coating from a solution of diF-TES-ADT at wt.0.5% in chlorobenzene. The source and drain electrodes are covered by the silver paste and the interdigitated structure is covered by the semiconductor. On the right a schematic view of the OTFT structure is showed

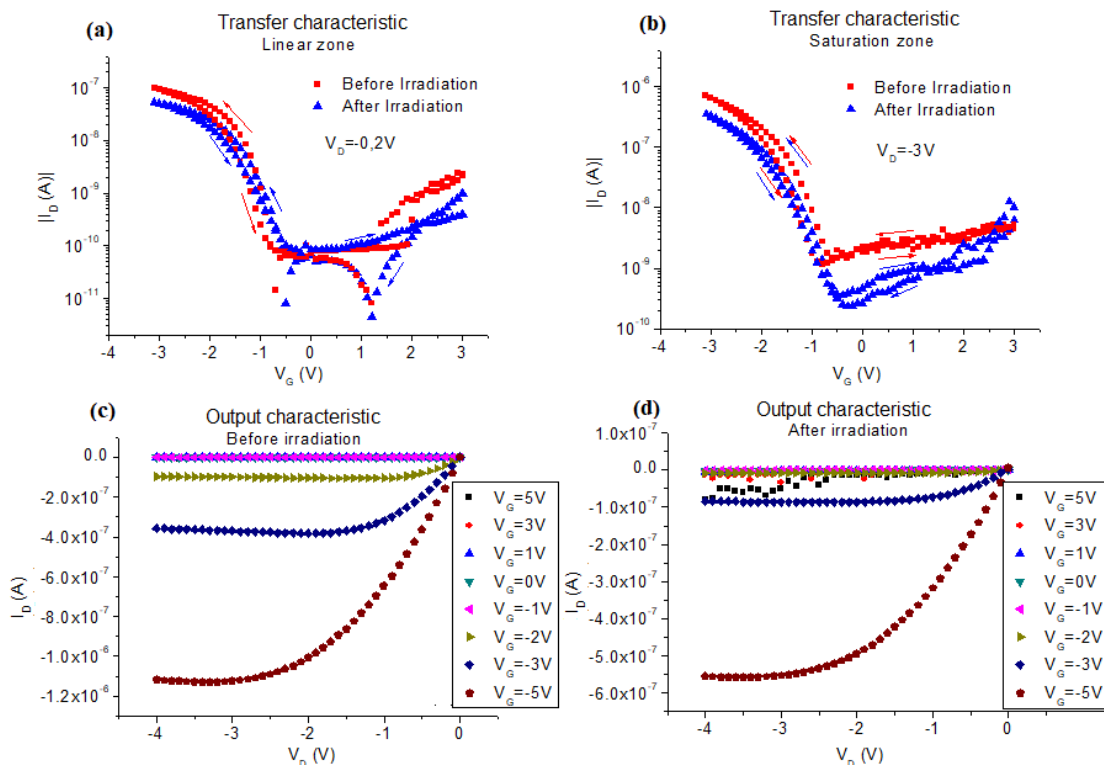


**Figure 4.16:** Electrical characterization of a typical device realized by spin-coating from a solution of diF-TES-ADT at wt.0.5% in chlorobenzene: (a) Transfer characteristic in linear regime (b) Transfer characteristic in saturation regime. (c) Output characteristic before the irradiation. (d) Output characteristic after the irradiation.

The table 4.4 shows the maximum value of the most important parameters, that, except for the  $I_{on}/I_{off}$  ratio, undergo a decrement after the exposition to the X-ray beams, because of the devices degradation after X-rays irradiation. The leakage current of these transistors is about  $10^{-9}$ A (Figure A.9 in the appendix).

$\mu$ (cm <sup>2</sup> /Vs)		$V_T$ (V)		$I_{on}/I_{off}$	
before X-rays	after X-rays	before X-rays	after X-rays	before X-rays	after X-rays
$(1.66 \pm 0.08) \cdot 10^{-2}$	$(1.39 \pm 0.07) \cdot 10^{-2}$	$-0.50 \pm 0.03$	$-0.83 \pm 0.04$	$(6.1 \pm 0.3) \cdot 10^3$	$(9.8 \pm 0.4) \cdot 10^3$

**Table 4.4:** Maximum value of characteristic transistor parameters before and after the exposition to X-rays for the devices realized by spin-coating from a solution of diF-TES-ADT at wt.0.5% in chlorobenzene.

When the samples are irradiated at a polarization of  $V_D = -3V$  and  $V_G = -2V$ , they exhibit a photocurrent of about  $10^{-10}$ A, and a sensitivity up to  $(53 \pm 4)$  nC/Gy. A typical response to X-rays is depicted in Figure 4.17. At the highest dose-rate  $D_r$  tested, the signal saturate in about 30 s, whereas at the other dose-rates it reaches the maximum at the end of the irradiation. The recovery for  $D_r = 30$  mGy/s starts after the attainment of the maximum photocurrent, but it is not possible to individuate an average behaviour, while for the other X-ray dose-rates the recovery starts, as usual, when the shutter is closed.

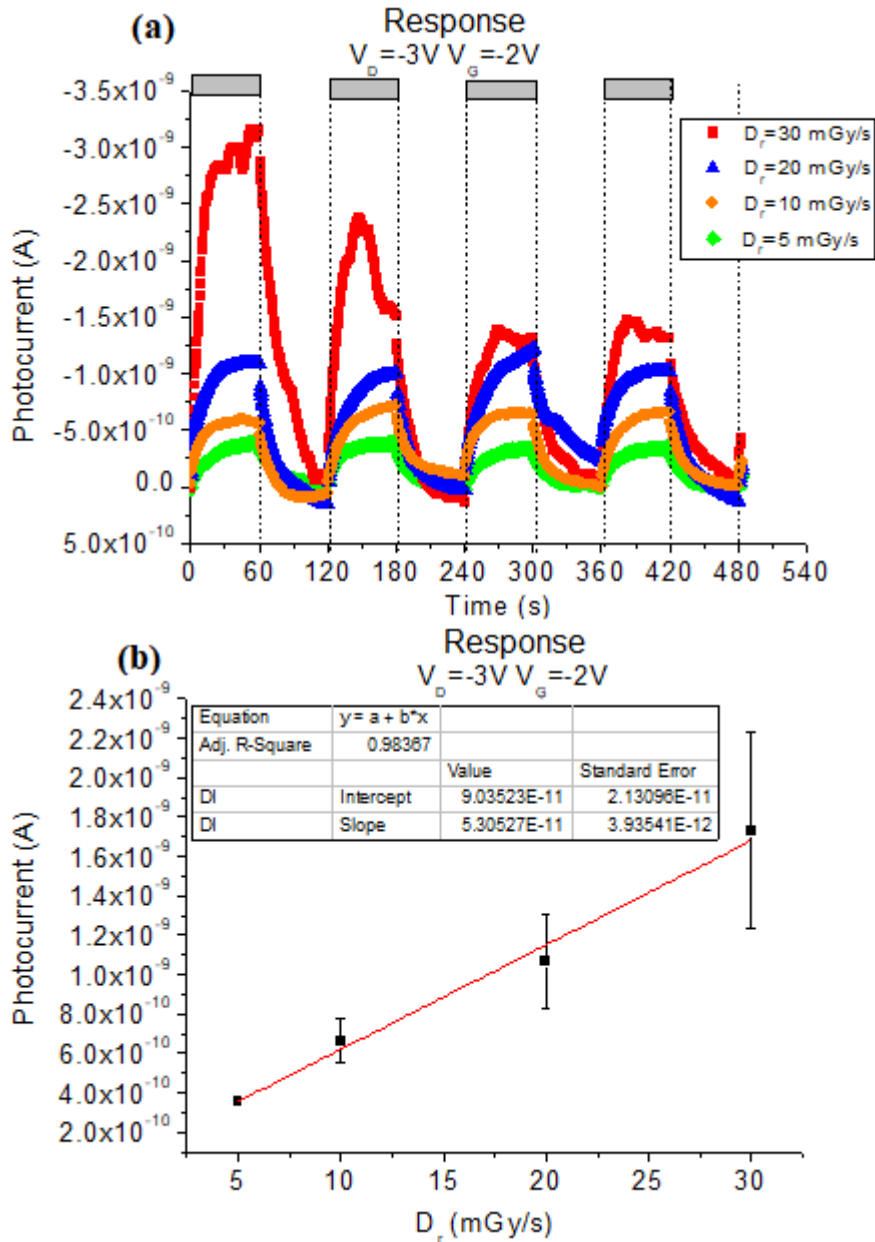


**Figure 4.17:** X-ray response of a typical device realized by spin-coating from a solution of diF-TES-ADT at wt.0.5% in chlorobenzene biased at  $V_D = -3V$  and  $V_G = -2V$ : (a) Photocurrent vs time for four X-ray irradiation cycles having different dose-rates. (b) Photocurrent vs dose-rate plot.

In order to compare the sensitivity of the devices fabricated by spin-coating from a solution of diF-TES-ADT at wt.0.5% in chlorobenzene with the sensitivity of the devices fabricated by spin-coating from a solution of diF-TEG-ADT at wt.0.5% in chlorobenzene, a polarization of  $V_D = -3V$  and  $V_G = -1V$  was applied during another irradiation cycle. A typical response produced at this condition is shown in Figure 4.18.

The photocurrent is about one order of magnitude lower than the photocurrent acquired during the previous measurement and the sensitivity drops to  $(18.9 \pm 0.5)$  nC/Gy. In this case the response of the devices appears reproducible and the dynamic is the same for all the dose-rates.

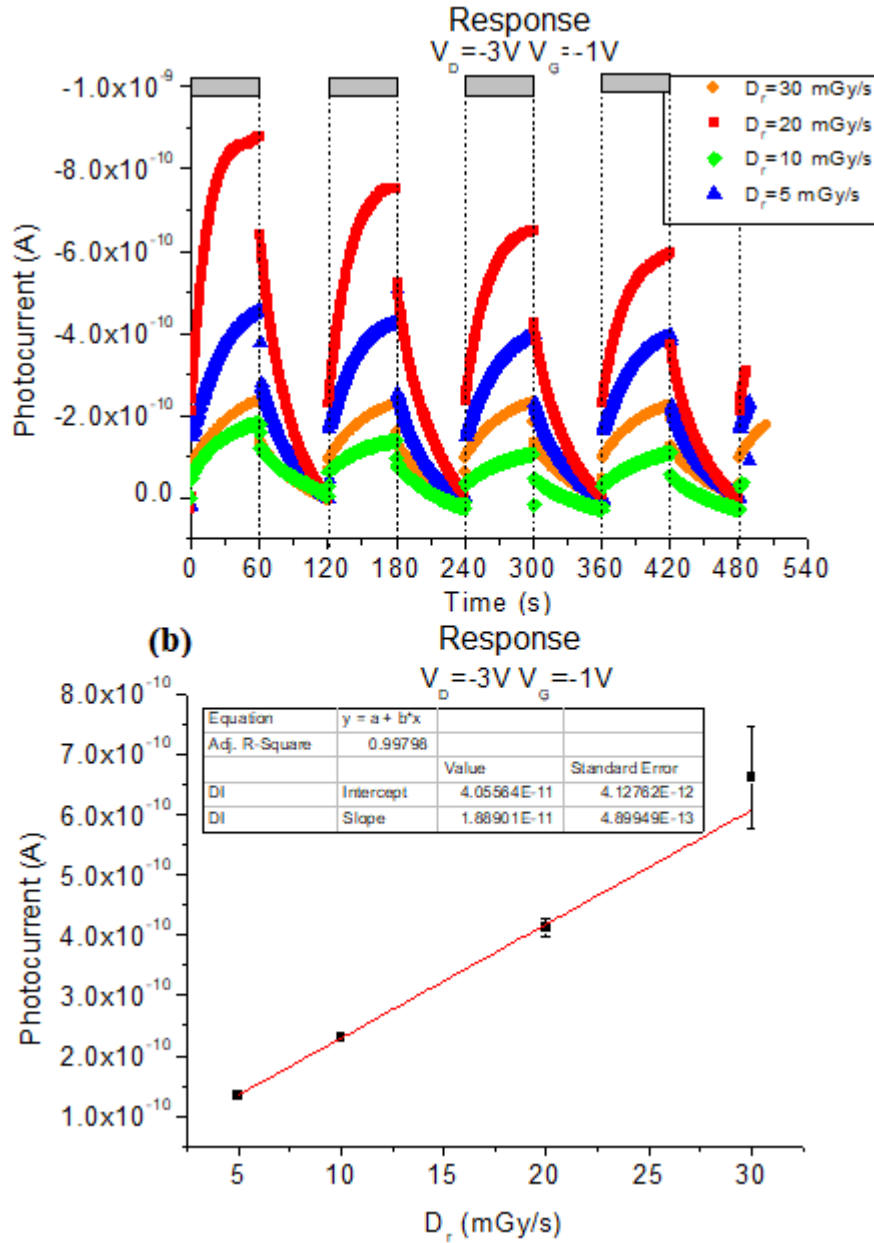


**Figure 4.18:** X-ray response of a typical device realized by spin-coating from a solution of diF-TES-ADT at wt.0.5% in chlorobenzene biased at  $V_D = -3V$  and  $V_G = -1V$ : (a) Photocurrent vs time for four X-ray irradiation cycles having different dose-rates. (b) Photocurrent vs dose-rate plot.

- **Solution at wt.0.5% of diF-TEG-ADT**

Two devices were fabricated by spin-coating from a solution at wt.0.5% of diF-TEG-ADT. They show a good transfer characteristic (Figure 4.20), characterized by a maximum drain current of about  $5 \cdot 10^{-6}$  A, which after the irradiation undergo a drop of about  $3 \cdot 10^{-6}$  A. In the output characteristic a good field effect is achieved, but the measurements carried out under irradiation indicate that they are not suitable to work as X-ray sensor, as detailed in the following. A picture of the active layer of one sample is reported in Figure 4.19.

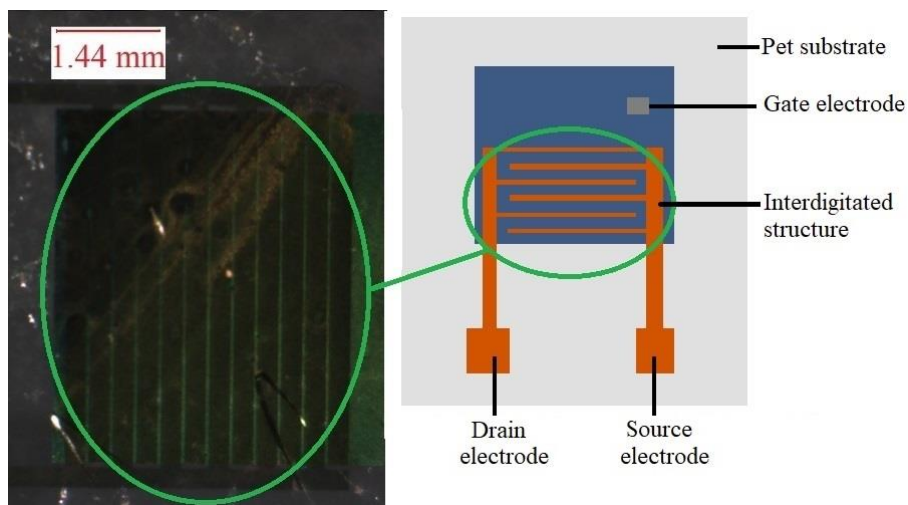


**Figure 4.19:** zoom over the active layer of a typical device realized by spin-coating from a solution of diF-TEG-ADT at wt.0.5% in chlorobenzene. It is possible to notice the interdigitated structure covered by the semiconductor.

The leakage current recorded during the acquisition of the transfer characteristic in saturation zone has a value of  $10^{-9}$  A before and after the irradiation (Figure A.12 in the appendix).

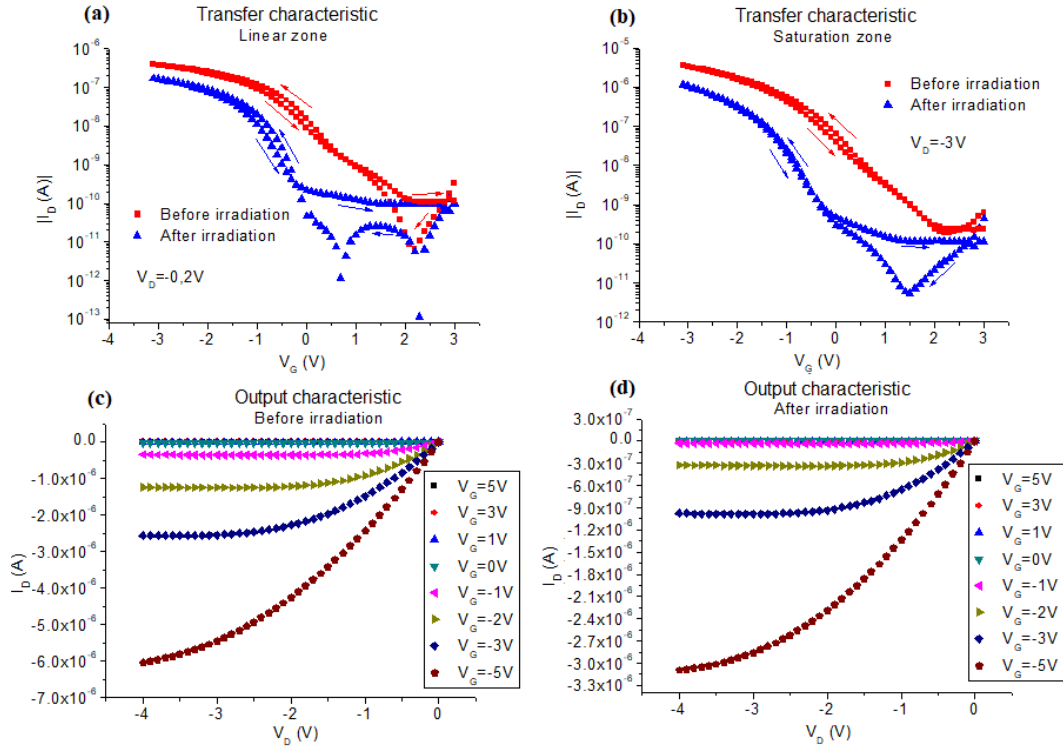


**Figure 4.20** Electrical characterization of a typical device realized by spin-coating from a solution of diF-TEG-ADT at wt.0.5% in chlorobenzene: (a) Transfer characteristic in linear regime (b) Transfer characteristic in saturation regime. (c) Output characteristic before the irradiation. (d) Output characteristic after the irradiation.

In Table 4.5 the maximum mobility  $\mu$ , the maximum threshold voltage  $V_T$  and the maximum  $I_{on}/I_{off}$  ratio are reported.

$\mu$ (cm <sup>2</sup> /Vs)		$V_T$ (V)		$I_{on}/I_{off}$	
before X-rays	after X-rays	before X-rays	after X-rays	before X-rays	after X-rays
$(4.1 \pm 0.2) \cdot 10^{-2}$	$(2.5 \pm 0.1) \cdot 10^{-2}$	$0.37 \pm 0.02$	$-0.31 \pm 0.02$	$(6.8 \pm 0.3) \cdot 10^4$	$(6.6 \pm 0.3) \cdot 10^4$

**Table 4.5:** Maximum value of characteristic transistor parameters before and after the exposition to X-rays for the devices realized by spin-coating from a solution of diF-TEG-ADT at wt.0.5% in chlorobenzene.

Only one of the two samples tested shows a response under X-rays, when polarized at  $V_D = -3V$  and  $V_G = -1V$  (Figure 4.21). The response dynamic is comparable to that of the other devices analysed. However, the photocurrent signal, that has a value of about  $10^{-10}A$ , is characterized by a certain noise and the peaks of photocurrents induced by the X-rays do not seem very reproducible. At this bias, the leakage current across the gate

electrode ( $I_G$ ) has a value of  $10^{-11}$  A, with a small increment in the periods of time when the shutter is open. The photocurrent as a function of the dose-rate has however a linear trend. The sensitivity value is  $(18 \pm 3)$  nC/Gy.

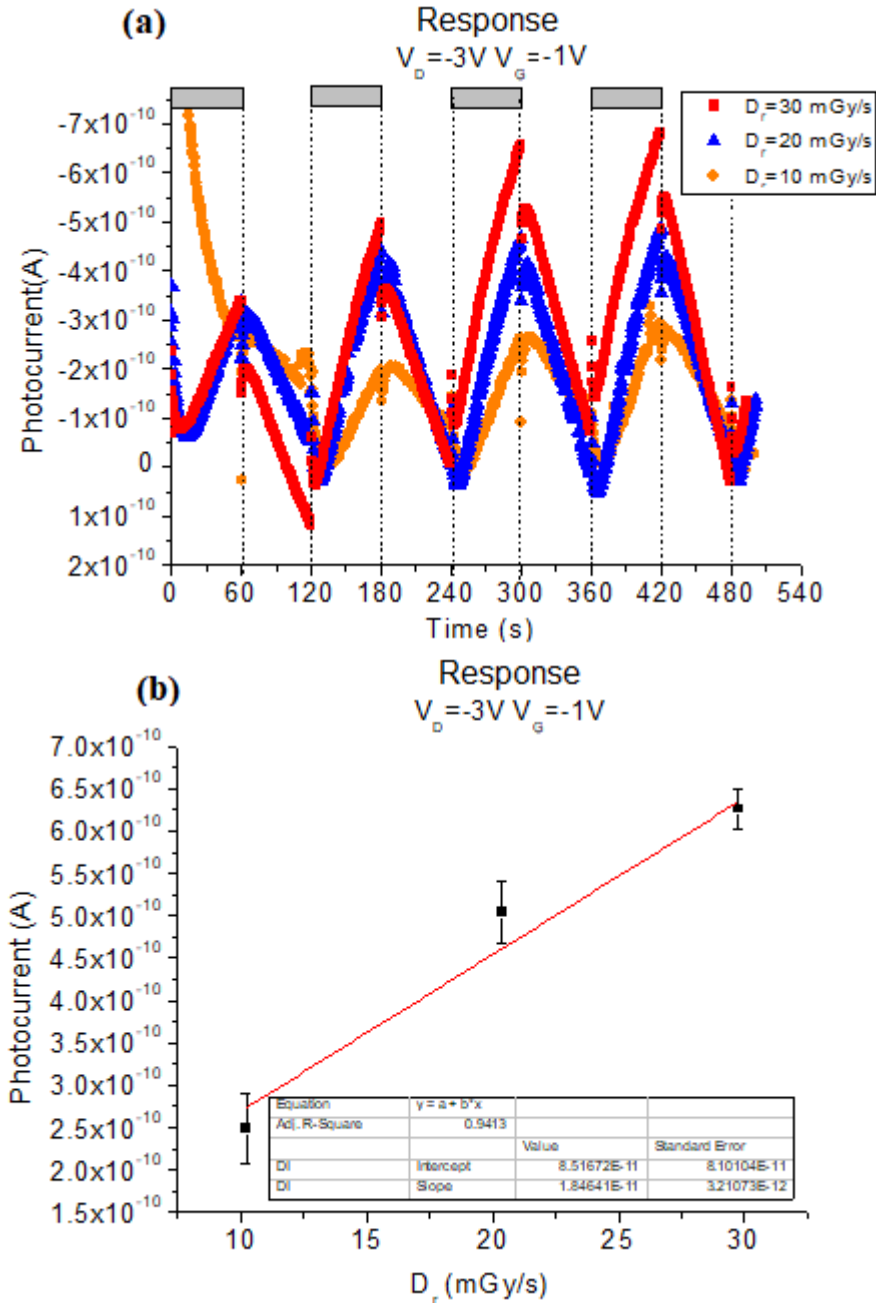


**Figure 4.21:** X-ray response of a typical device realized by spin-coating from a solution of diF-TEG-ADT at wt.0.5% in chlorobenzene biased at  $V_D = -3V$  and  $V_G = -1V$ : (a) Photocurrent vs time for four X-ray irradiation cycles having different dose-rates. (b) Photocurrent vs dose-rate plot.

## 4.4 Devices realized by spin-coating from solutions at wt.2%

### - Solution at wt.2% of diF-TES-ADT

Three devices were realized from a diF-TES-ADT solution at concentration wt.2%, but only two resulted working properly as X-ray detectors. A picture of one device is reported in Figure 4.22. It is possible to notice the three electrodes (source, drain and gate) covered by the silver paste, and the interdigitated structure, covered by the semiconductor. These samples show a good transistor-like behaviour, presented in Figure 4.23a and b (the transfer characteristics) and 4.23c and d (the output characteristics), and worked quite well under X-rays.

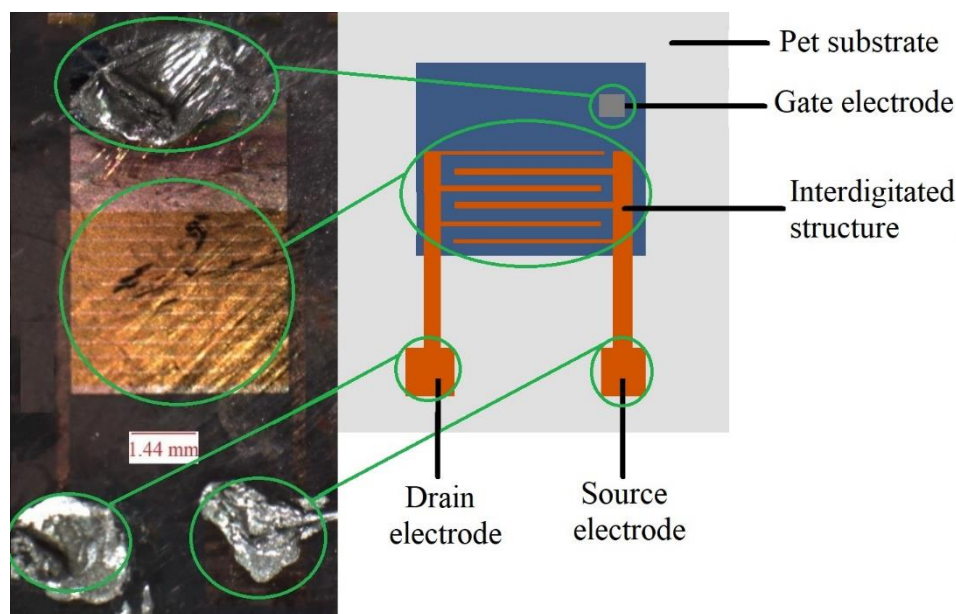


**Figure 4.22:** a typical device realized by spin-coating from a solution of diF-TES-ADT at wt.2% in chlorobenzene. The three electrodes are covered by the silver paste and the interdigitated structure is covered by the semiconductor

The maximum current reached before the irradiation, anyhow, is different for the two devices analysed: in one sample its value is about  $1.4 \cdot 10^{-6}$  A and in the other one is approximately  $6 \cdot 10^{-8}$  A. After measurements under X-rays it results approximately halved. The  $I_{\text{off}}$  before the X-rays exposition is about  $10^{-11}$  A and it is similar for both

devices, as like as the leakage current across the gate ( $I_G$ ), that has a value of about  $10^{-10}$ A. (Figure A.14 in the appendix). The maximum mobility  $\mu$ , the maximum threshold voltage  $V_T$ , are presented in table 4.6 with the maximum  $I_{on}/I_{off}$  ratio. The output characteristics show that the drain current  $I_D$  saturates at  $V_D=-3$  and  $V_G=-2$ V, as expected.

$\mu$ (cm <sup>2</sup> /Vs)		$V_T$ (V)		$I_{on}/I_{off}$	
before X-rays	after X-rays	before X-rays	after X-rays	before X-rays	after X-rays
$(1.38 \pm 0.07) \cdot 10^{-2}$	$(1.23 \pm 0.06) \cdot 10^{-2}$	$0.0 \pm 0.1$	$-1.54 \pm 0.08$	$(2.1 \pm 0.1) \cdot 10^4$	$(2.0 \pm 0.1) \cdot 10^4$

**Table 4.6:** Maximum value of characteristic transistor parameters before and after the exposition to X-rays for the devices realized by spin-coating from a solution of diF-TES-ADT at wt.2% in chlorobenzene.

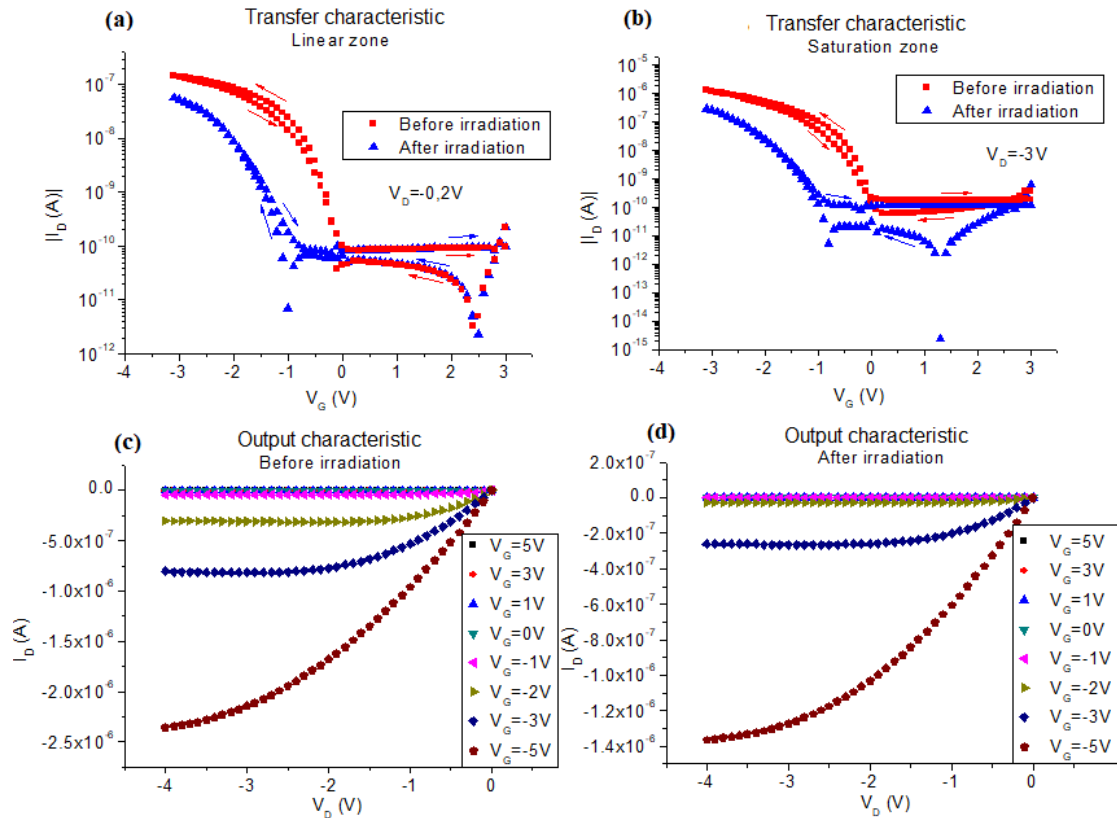


**Figure 4.23:** Electrical characterization of a typical device realized by spin-coating from a solution of diF-TES-ADT at 2% in chlorobenzene: (a) Transfer characteristic in linear regime (b) Transfer characteristic in saturation regime. (c) Output characteristic before the irradiation. (d) Output characteristic after the irradiation

When the devices are irradiated (biased at  $V_D=-3$ V and  $V_G=-2$ V) they produce a photocurrent of about  $10^{-10}$  A (Figure 4.24a). The peaks of photocurrent, due to the

exposition to the X-ray beam, are characterized by a certain noise level, and they are not very reproducible, especially in one device. It is possible to notice the sawtooth shape of the photocurrent signal, when it is plotted as a function of time, whereas when it is plotted as a function of dose-rate  $D_r$  it is linear. The sensitivity found is up to  $(19 \pm 1)$  nC/Gy.

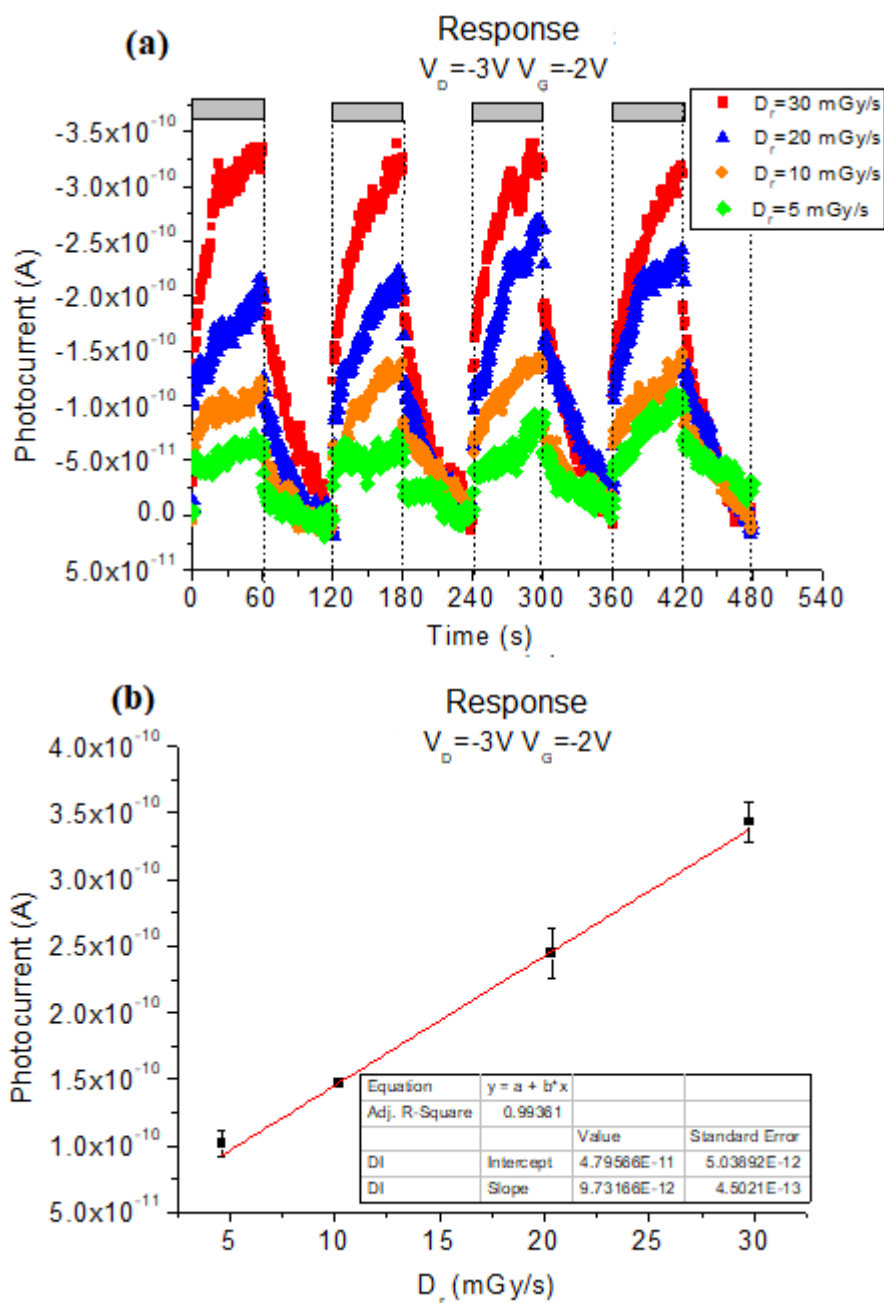


**Figure 4.24** X-ray response of a typical device realized by spin-coating from a solution of diF-TES-ADT at wt.2% in chlorobenzene biased at  $V_D = -3V$  and  $V_G = -2V$ : (a) Photocurrent vs time for four X-ray irradiation cycles having different dose-rates. (b) Photocurrent vs dose-rate plot.

## - Solution at wt.2% of diF-TEG-ADT

Six devices were realized by spin-coating from a solution of diF-TEG-ADT at concentration wt.2%, but only three resulted working properly as transistors. The Figure 4.25 show a picture of the devices, in which it is possible to notice the three electrodes, covered by the silver paste, and the interdigitated structure (covered by the semiconductor), as indicated by the schematic view on the right side. These samples show a very good output and transfer characteristics (Figure 4.26), with no hysteresis for the latter, and also the behaviour under X-rays is satisfactory.

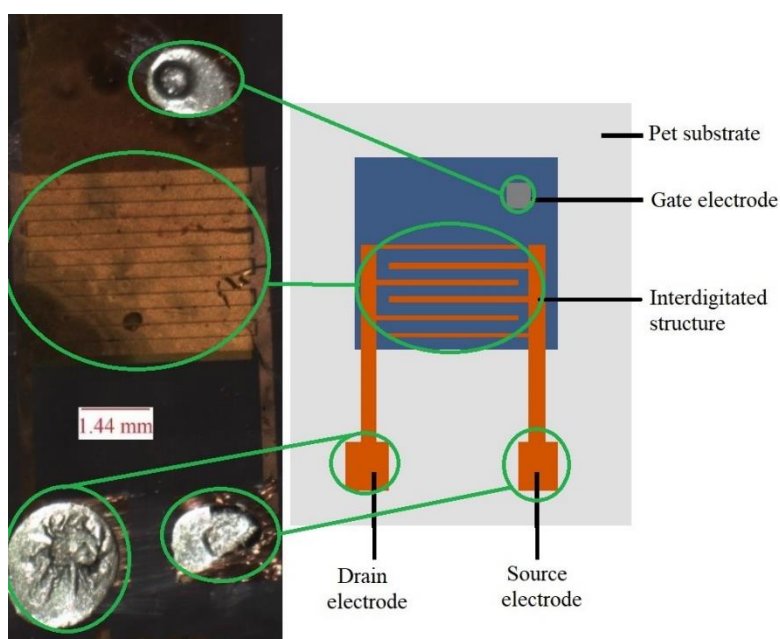


**Figure 4.25:** a typical device realized by spin-coating from a solution of diF-TEG-ADT at 2% in chlorobenzene. The source, drain and gates electrodes are covered by the silver paste and the interdigitated structure is covered by the semiconductor.

The maximum drain current is approximately  $10^{-6}$  A, and it decreases of about one order of magnitude after the irradiation. On the contrary, the off current ( $\approx 10^{-9}$  A) remains almost constant after the X-ray exposition, like the leakage current that has a value of  $10^{-9}$  A- $10^{-10}$  A (Figure A.16 in the appendix). The maximum mobility  $\mu$ , the maximum threshold voltage  $V_T$  and the maximum  $I_{on}/I_{off}$  ratio (reported in Table 4.7) have, a drop after X-ray characterization. Output characteristics (Figure 4.26c and d) show that the drain current  $I_D$  reaches the saturation.

$\mu$ (cm <sup>2</sup> /Vs)		$V_T$ (V)		$I_{on}/I_{off}$	
before X-rays	after X-rays	before X-rays	after X-rays	before X-rays	after X-rays
$(2.6 \pm 0.1) \cdot 10^{-2}$	$(2.3 \pm 0.1) \cdot 10^{-2}$	$0.066 \pm 0.003$	$0.016 \pm 0.001$	$(8.1 \pm 0.4) \cdot 10^2$	$(2.7 \pm 0.1) \cdot 10^2$

**Table 4.7:** Maximum value of characteristic transistor parameters before and after the exposition to X-rays for the devices realized by spin-coating from a solution of diF-TEG-ADT at wt.2% in chlorobenzene.

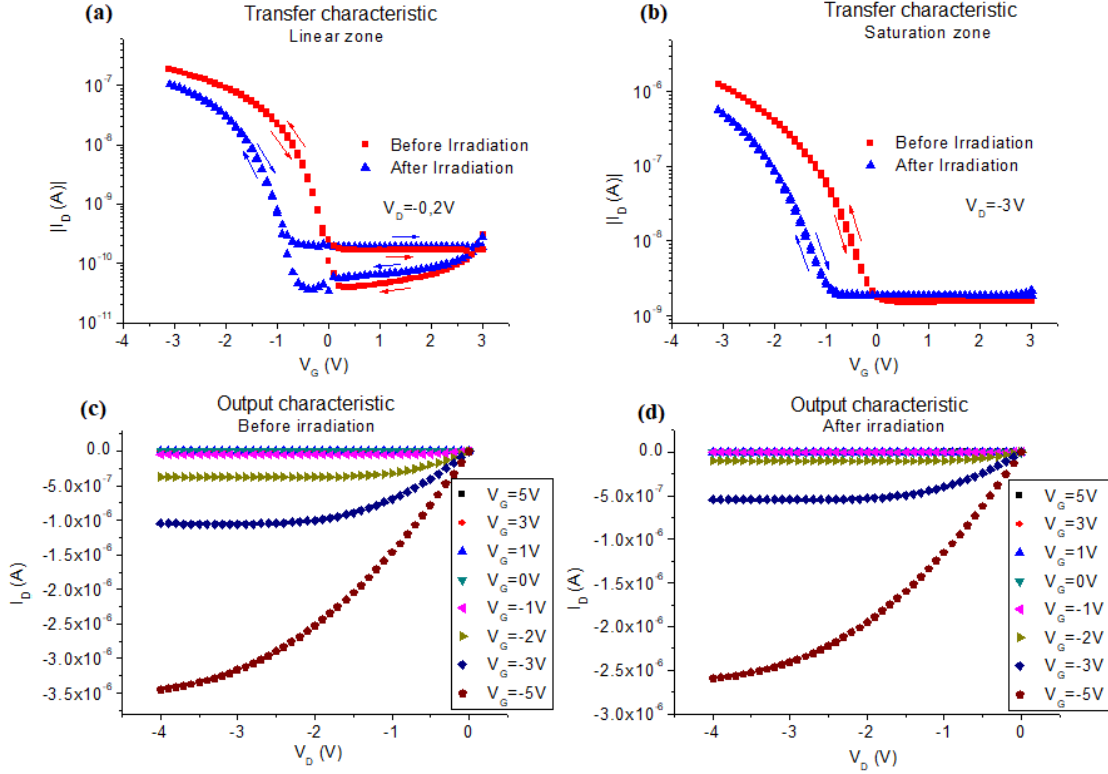


**Figure 4.26:** Electrical characterization of a typical device realized by spin-coating from a solution of diF-TEG-ADT at wt.2% in chlorobenzene: (a) Transfer characteristic in linear regime (b) Transfer characteristic in saturation regime. (c) Output characteristic before the irradiation. (d) Output characteristic after the irradiation

When these devices are irradiated, they produce a photocurrent signal of about  $10^{-9}$ A, that is characterized by a low noise. At this bias, the leakage current is about  $10^{-11}$ A. The photocurrent peaks, formed when the X-ray beam reaches the transistor, appear quite reproducible, and the signal reported as a function of time (Figure 4.27a) is characterized by a sawtooth shape. The sensitivity, that has a linear trend in the plot photocurrent vs dose-rate (Figure 4.27b) has a maximum value of  $150 \pm 30$  nC/Gy. The sensitivity of these X-ray detectors, fabricated starting from a solution at wt.2% of diF-

TEG-ADT, is one order of magnitude larger than the sensitivity of the detectors realized at the same conditions with the molecule diF-TEG-ADT, presented in the previous paragraph.

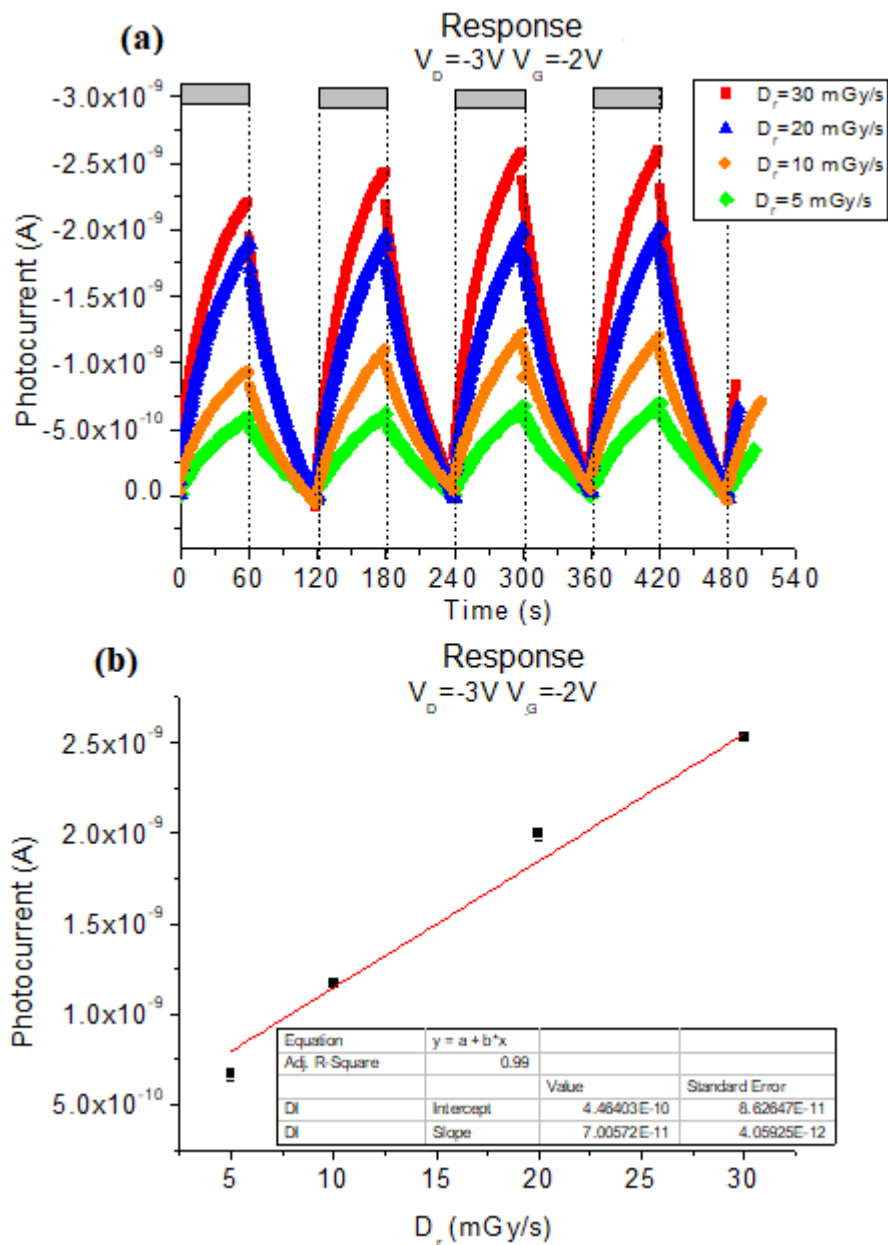


**Figure 4.27:** X-ray response of a typical device realized by spin-coating from a solution of diF-TEG-ADT at wt.2% in chlorobenzene biased at  $V_D = -3V$  and  $V_G = -2V$ : (a) Photocurrent vs time for four X-ray irradiation cycles having different dose-rates. (b) Photocurrent vs dose-rate plot.

# Conclusions

The motivation of this thesis was the comparison of the performance as X-ray detectors of organic thin film transistors, realized with solutions of diF-TES-ADT and diF-TEG-ADT, two novel molecules (provided by Prof. J. Anthony of the University of Kentucky, USA) having in their structure two identical functional groups containing an atom of silicon (diF-TES-ADT) and an atom of germanium (diF-TEG-ADT). The germanium has an atomic number higher than the silicon, that determines a larger absorption cross section for the X-rays than diF-TEG-ADT, and thus a detector with a higher sensitivity. In order to confirm this hypothesis, several samples were fabricated and analysed. The summary table reported below presents the top values of mobility ( $\mu$ ),  $I_{on}/I_{off}$  ratio, sensitivity  $S$  and specific sensitivity  $S_v$  of the eight kinds of devices fabricated and analysed.

Molecule	C (wt%)	Deposition technique	$\mu$ (cm <sup>2</sup> /Vs)	$I_{on}/I_{off}$	S (nC/Gy)	$S_v$ (nC/mGy/cm <sup>3</sup> )
diF-TES-ADT	0.5	Drop-casting	/	/	25±4 (*)	/
diF-TEG-ADT	0.5	Drop-casting	/	/	24±6 (*)	/
diF-TES-ADT	1.2	Spin-coating	(1.01±0.05)·10 <sup>-2</sup>	(5.5±0.3)·10 <sup>2</sup>	28±2	100±10
diF-TEG-ADT	1.2	Spin-coating	(7.7±0.4)·10 <sup>-2</sup>	(1.09±0.06)·10 <sup>3</sup>	690±80	3400±500
diF-TES-ADT	0.5	Spin-coating	(1.66±0.08)·10 <sup>-2</sup>	(6.1±0.3)·10 <sup>3</sup>	53±4	/
diF-TEG-ADT	0.5	Spin-coating	(4.1±0.2)·10 <sup>-2</sup>	(6.8±0.3)·10 <sup>4</sup>	18±3(**)	/
diF-TES-ADT	2	Spin-coating	(1.38±0.07)·10 <sup>-2</sup>	(2.1±0.1)·10 <sup>4</sup>	19±1	/
diF-TEG-ADT	2	Spin-coating	(2.6±0.1)·10 <sup>-2</sup>	(8.1±0.4)·10 <sup>2</sup>	150±30	/

**Summary Table:** Top values of mobility ( $\mu$ ),  $I_{on}/I_{off}$  ratio (both before the irradiation), sensitivity ( $S$ ) and specific sensitivity ( $S_v$ ), for each type of device fabricated. The sensitivity and the specific sensitivity indicated were obtained polarizing the devices at  $V_D=-3V$  and  $V_G=-2V$ , except for the values accompanied by (\*), which indicates that the sensitivity was obtained polarizing the transistors at  $V_D=-0.5V$  and  $V_G=-1V$  or (\*\*), which indicates that the sensitivity was obtained polarizing the transistors at  $V_D=-3V$  and  $V_G=-1V$ . The concentration of the starting solution (C), the deposition technique and the molecule used are indicate.

Summarizing the results obtained, it is possible to conclude that:

- The devices realized by spin-coating from solutions at wt.1.2% of diF-TES-ADT and diF-TEG-ADT in chlorobenzene present a good transistor-like behaviour and they work well as direct X-ray detectors. Their average specific sensitivities differ of two orders of magnitude, (while the maximum specific sensitivities differ of one order of magnitude) and the specific sensitivity of the diF-TEG-ADT is higher, thus confirming the starting hypothesis. Moreover, the diF-TEG-ADT-based detectors show the best performance and reach the highest sensitivity, among all the devices realized.
- The devices realized by spin-coating from solutions at wt.2% of diF-TES-ADT and diF-TEG-ADT in chlorobenzene show a good transistor-like behaviour, and also the response under irradiation is good. The devices fabricated with diF-TEG-ADT have a sensitivity one order of magnitude higher than the one of the diF-TES-ADT-based samples, therefore the starting hypothesis is confirmed also in these transistors.
- The transistors realized by spin-coating from solutions at wt.0.5% of diF-TES-ADT and diF-TEG-ADT in chlorobenzene cannot be employed as X-ray detectors.
- The devices realized by drop-casting from solutions at 0.5% of diF-TES-ADT and diF-TEG-ADT in chlorobenzene do not show transistor-like behaviour but they behave as variable resistors.
- The top mobility is similar for all the types of devices investigated, whereas the maximum value of  $I_{on}/I_{off}$  ratio is different in some kind of devices. Anyhow this difference does not appear correlated with the sensitivity.

In conclusion, the devices fabricated starting from the solutions at wt.1.2% and wt.2% confirm clearly the starting hypothesis and produce a satisfactory response under X-rays. Therefore, it is possible to enhance the sensitivity of the organic X-ray direct detectors including atoms characterized by a high atomic number, that, as demonstrated in this experimental work, thanks to their higher X-ray absorption cross section, allow to reach higher sensitivities, in comparison with the organic semiconductors.

# Appendix

In this appendix the plots of the raw data of drain current  $I_D$  acquired under irradiation, and the plots of the leakage current  $I_G$  are presented.

## A.1 Leakage current plots and raw data plots

In this paragraph two kind of plots (Figure A.1-A.17) are reported:

- The plots of the leakage current during the acquisition of the transfer characteristic in saturation regime.
- The plots of the drain current  $I_D$  acquired during the irradiation cycles

The leakage current, that is the current  $I_G$  flowing in the gate electrode, is plotted as a function of  $V_G$ . Each subparagraph is named by the kind of device at which the plots are referred. As in the chapter 4 the arrows indicate the direction of the  $V_G$  scan, and the grey rectangles indicate the periods of time in which the shutter is open and therefore the sample is irradiated.

### A.1.1 Devices realized by drop-casting from a solution of diF-TES-ADT at wt.0.5%

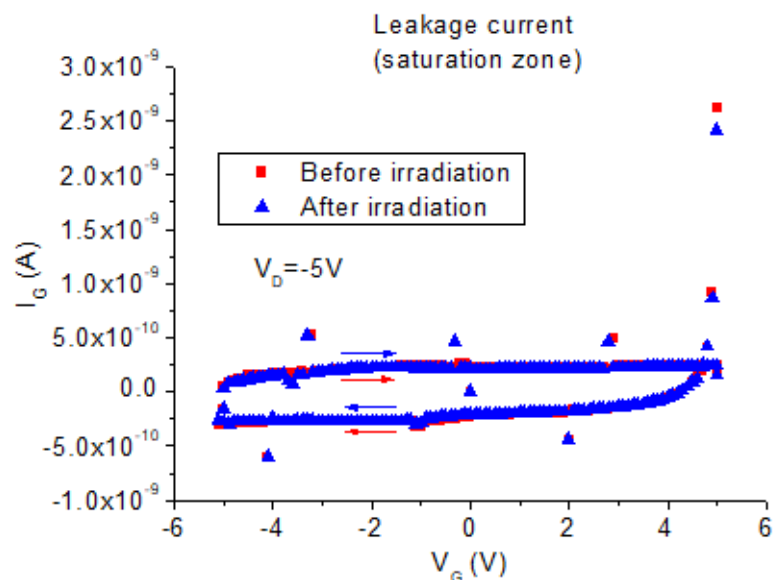


**Figure A.1:** Typical leakage current recorded during the acquisition of the transfer characteristic in the region that should be of saturation in the devices realized by drop-casting from a solution of diF-TES-ADT at wt.0.5%.

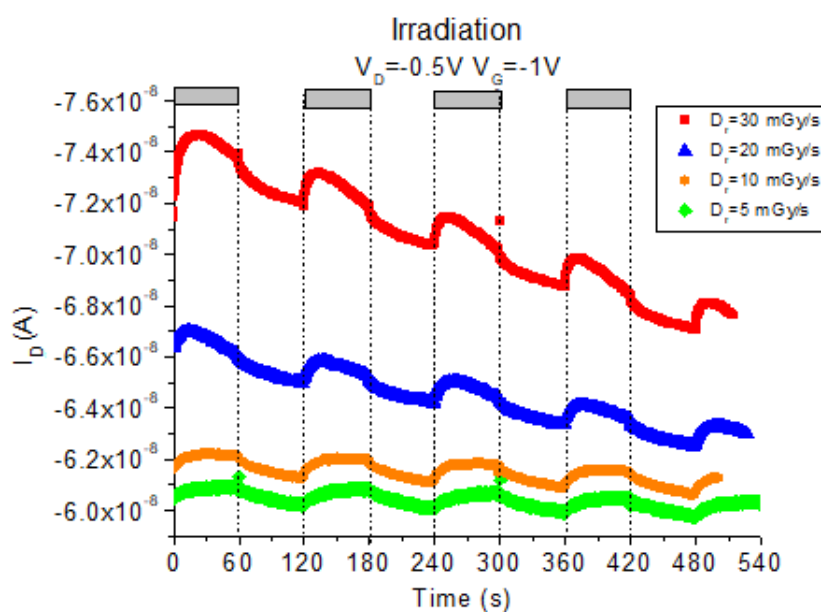


**Figure A.2:** Typical drain current acquired during four different irradiation cycles under X-ray beams having different dose-rates  $D_r$  in the devices realized by drop-casting from a solution of diF-TES-ADT at wt.0.5%, biased at  $V_D = -0.5V$  and  $V_G = -1V$ .

## A.1.2 Devices realized by drop-casting from a solution of diF-TEG-ADT at wt.0.5%

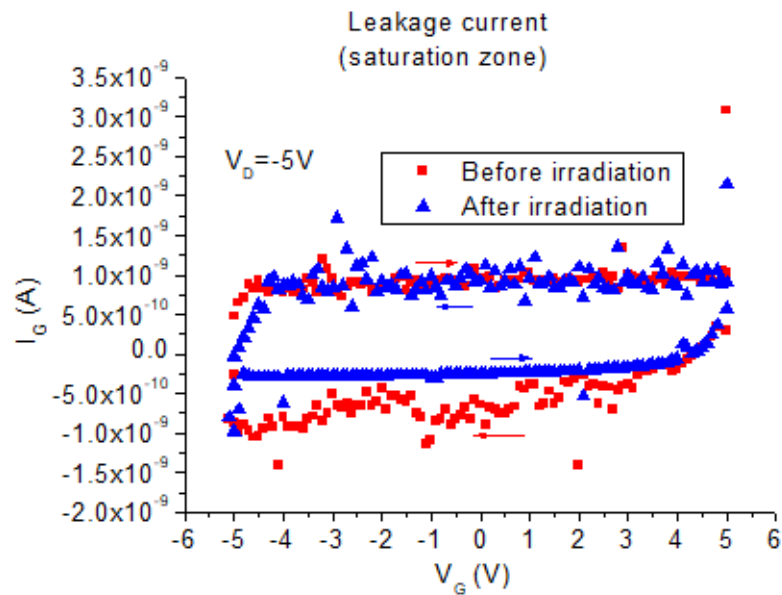


**Figure A.3:** Typical leakage current recorded during the acquisition of the transfer characteristic in the region that should be of saturation in the devices realized by drop-casting from a solution of diF-TEG-ADT at wt.0.5%.

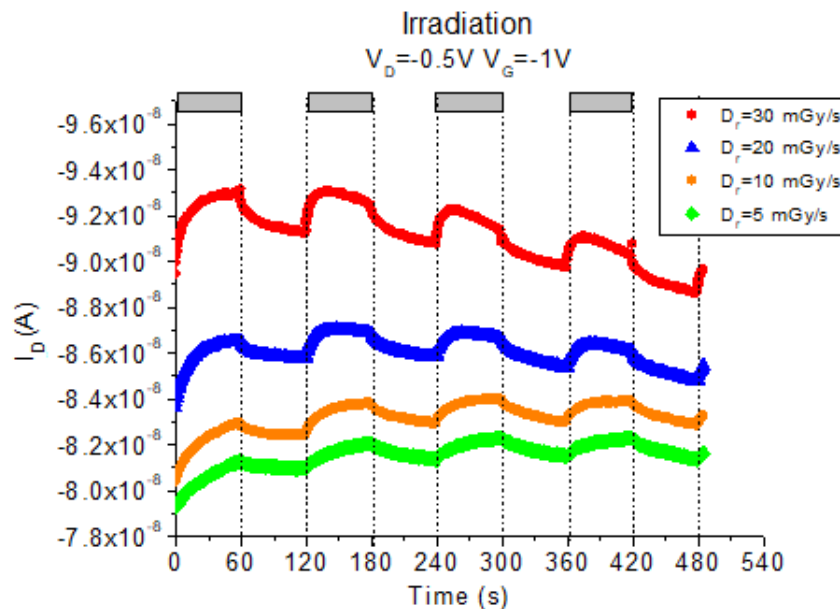


**Figure A.4:** Typical drain current acquired during four different irradiation cycles under X-ray beams having different dose-rates  $D_r$  in the devices realized by drop-casting from a solution of diF-TEG-ADT at wt.0.5%, biased at  $V_D = -0.5V$  and  $V_G = -1V$ .

### A.1.3 Devices realized by spin-coating from a solution of diF-TES-ADT at wt.1.2%

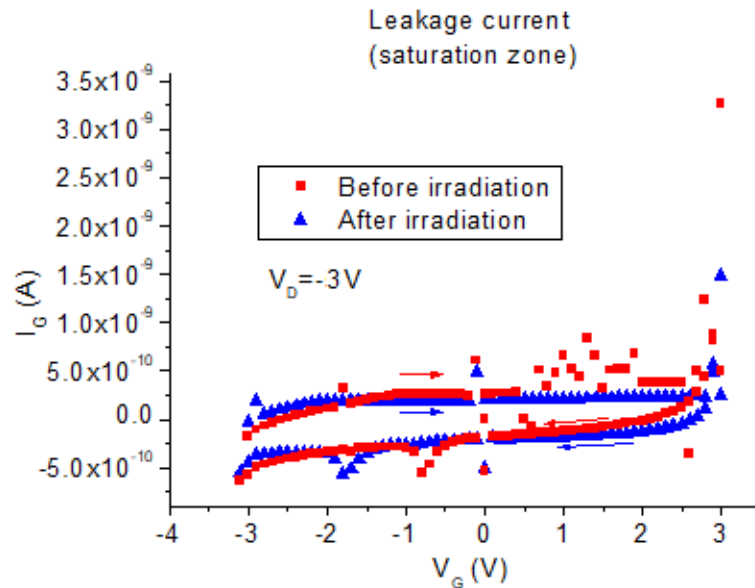


**Figure A.5:** Typical leakage current recorded during the acquisition of the transfer characteristic in the region of saturation in the devices realized by spin-coating from a solution of diF-TES-ADT at wt.1.2%.

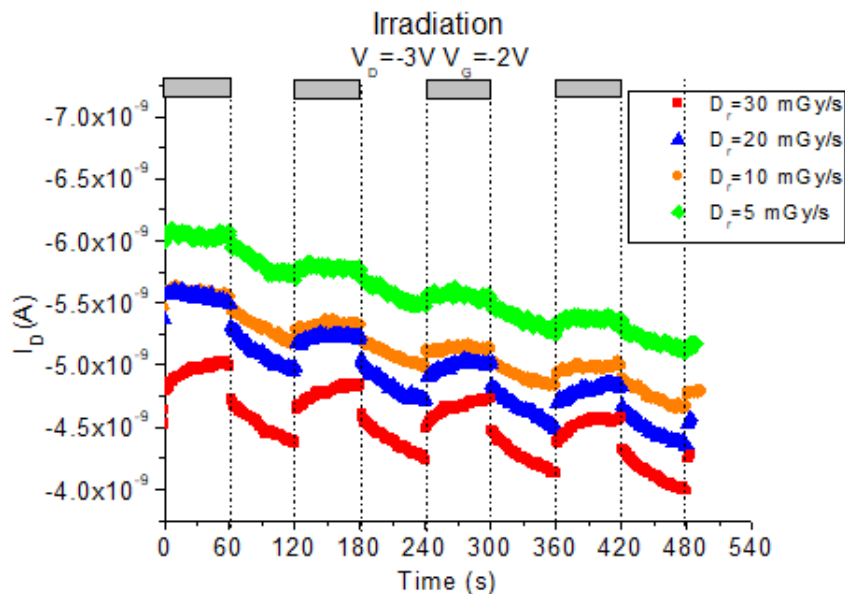


**Figure A.6:** Typical drain current acquired during four different irradiation cycles under X-ray beams having different dose-rates  $D_r$  in the devices realized by spin-coating from a solution of diF-TES-ADT at wt.1.2%, biased at  $V_D = -3V$  and  $V_G = -2V$ .

### A.1.4 Devices realized by spin-coating from a solution of diF-TEG-ADT at wt.1.2%

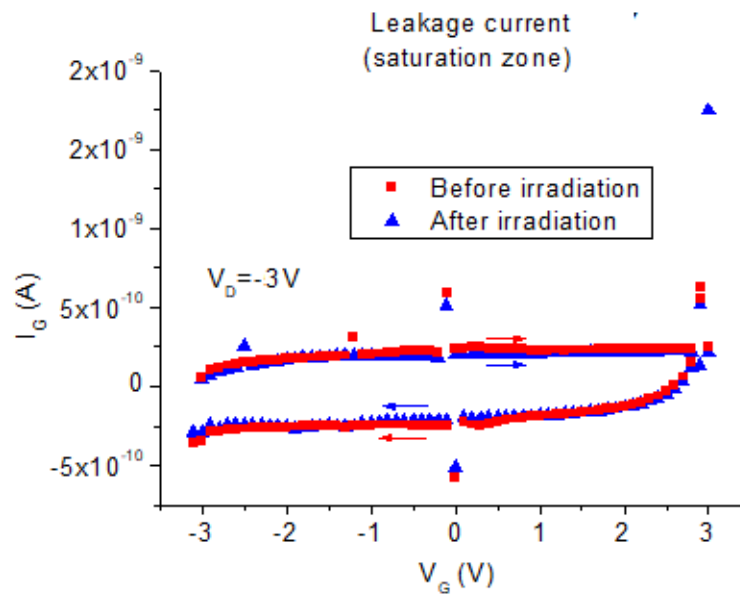


**Figure A.7:** Typical leakage current recorded during the acquisition of the transfer characteristic in the region of saturation in the devices realized by spin-coating from a solution of diF-TEG-ADT at wt.1.2%.

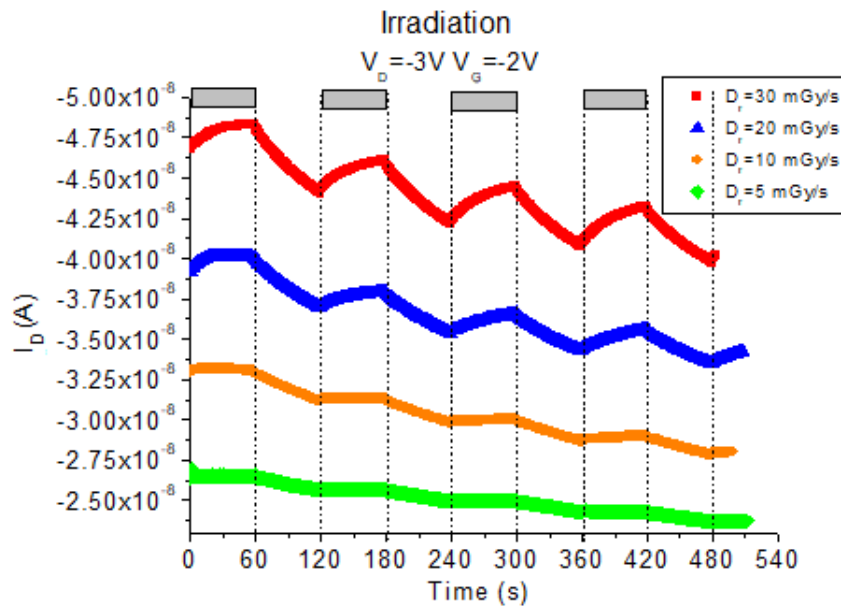


**Figure A.8:** Typical drain current acquired during four different irradiation cycles under X-ray beams having different dose-rates  $D_i$  in the devices realized by spin-coating from a solution of diF-TEG-ADT at wt.1.2%, biased at  $V_D = -3V$  and  $V_G = -2V$ .

### A.1.5 Devices realized by spin-coating from a solution of diF-TES-ADT at wt.0.5%

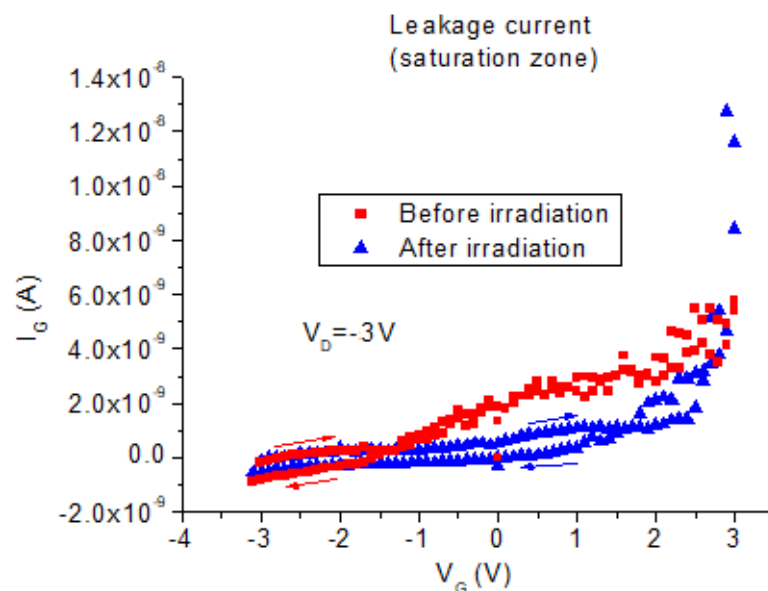


**Figure A.9:** Typical leakage current recorded during the acquisition of the transfer characteristic in the region of saturation in the devices realized by spin-coating from a solution of diF-TES-ADT at wt.0.5%

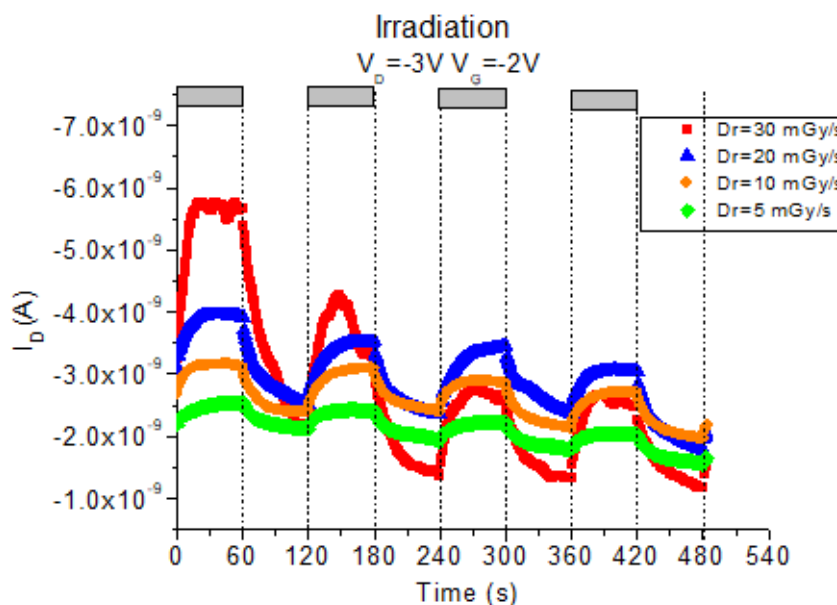


**Figure A.10:** Typical drain current acquired during four different irradiation cycles under X-ray beams having different dose-rates  $D_r$  in the devices realized by spin-coating from a solution of diF-TES-ADT at wt.0.5%, biased at  $V_D=-3V$  and  $V_G=-2V$ .

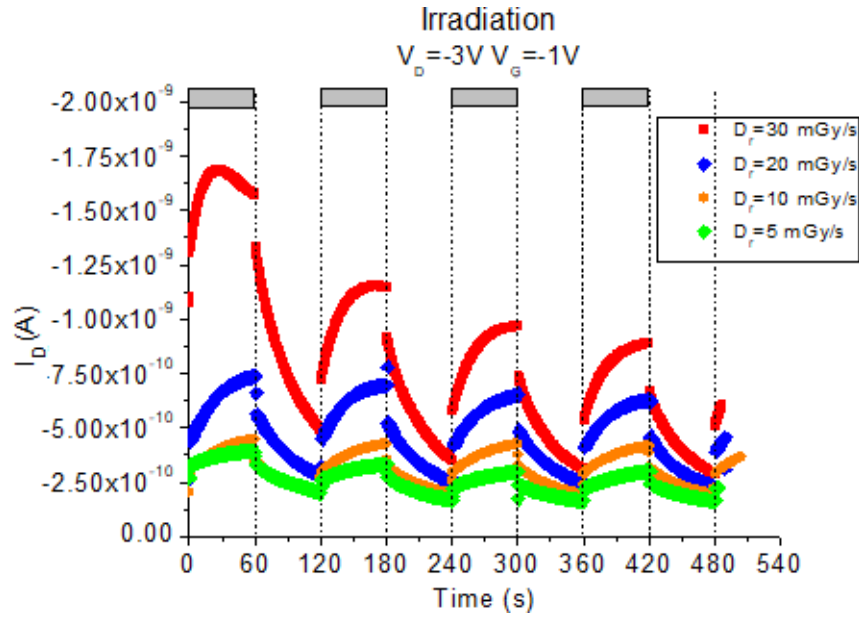


**Figure A.11:** Typical drain current acquired during four different irradiation cycles under X-ray beams having different dose-rates  $D_r$  in the devices realized by spin-coating from a solution of diF-TES-ADT at wt.0.5%, biased at  $V_D = -3V$  and  $V_G = -1V$ .

### A.1.6 Devices realized by spin-coating from a solution of diF-TEG-ADT at wt.wt.0.5%

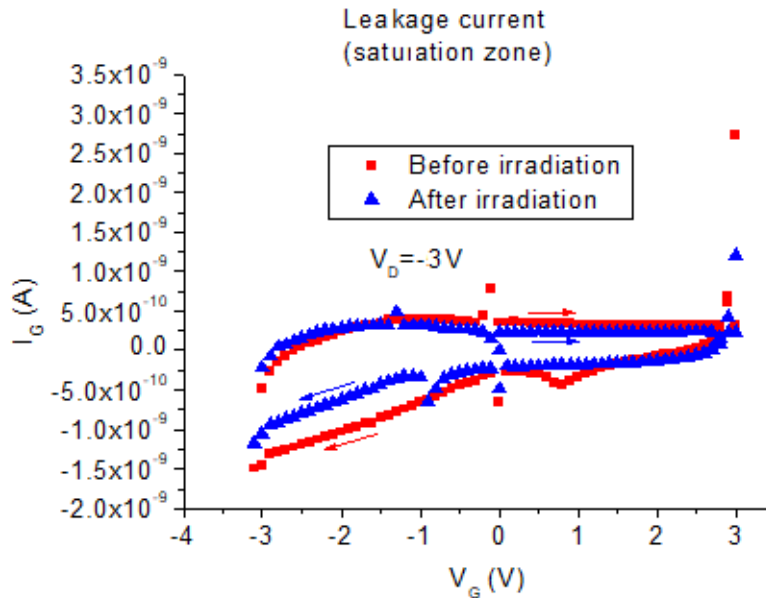


**Figure A.12:** Typical leakage current recorded during the acquisition of the transfer characteristic in the region of saturation in the devices realized by spin-coating from a solution of diF-TEG-ADT at wt.0.5%.

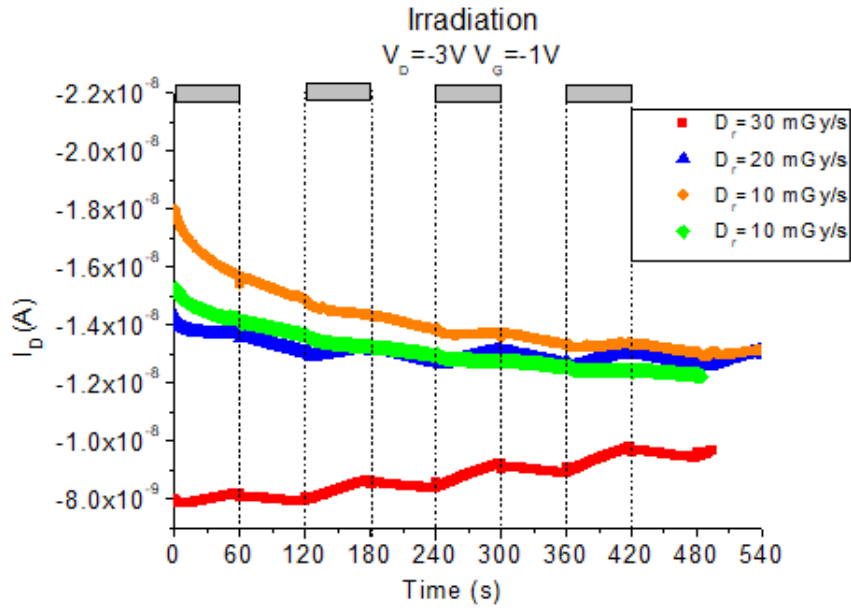


**Figure A.13:** Typical drain current acquired during four different irradiation cycles under X-ray beams having different dose-rates  $D_r$  in the devices realized by spin-coating from a solution of diF-TEG-ADT at wt.0.5%, biased at  $V_D = -3V$  and  $V_G = -1V$ .

### A.1.7 Devices realized by spin-coating from a solution of diF-TES-ADT at wt.2%

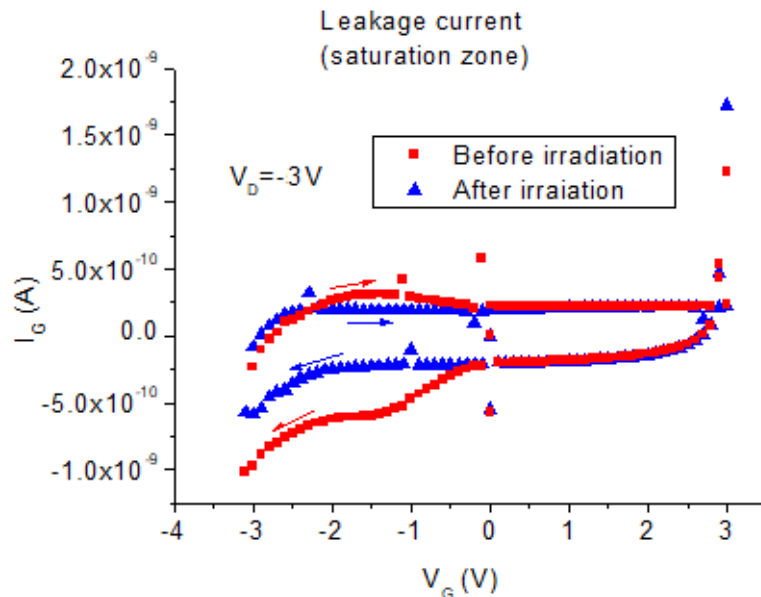


**Figure A.14:** Typical leakage current recorded during the acquisition of the transfer characteristic in the region of saturation in the devices realized by spin-coating from a solution of diF-TES-ADT at wt.2%

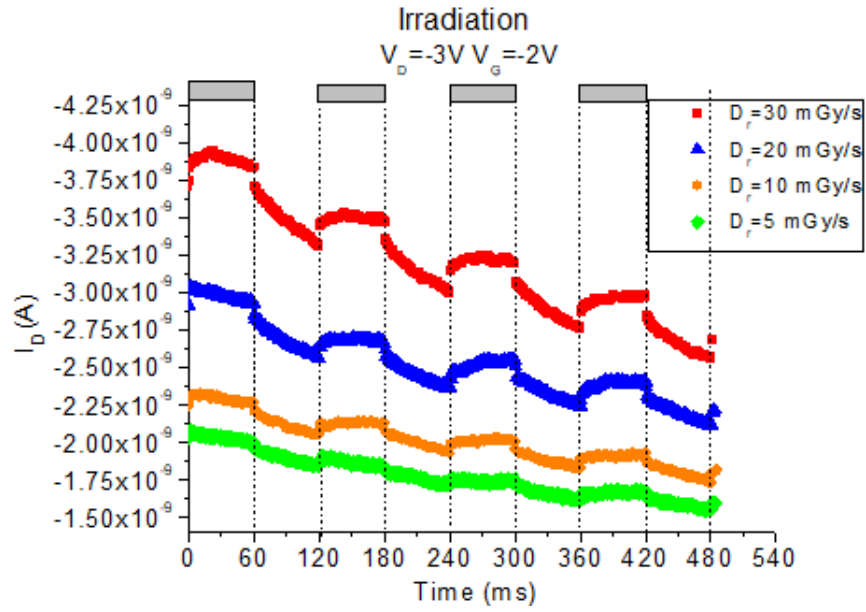


**Figure A.15:** Typical drain current acquired during four different irradiation cycles under X-ray beams having different dose-rates  $D_r$  in the devices realized by spin-coating from a solution of diF-TES-ADT at wt.2%, biased at  $V_D = -3V$  and  $V_G = -2V$ .

### A.1.8 Devices realized by spin-coating from a solution of diF-TEG-ADT at wt.2%

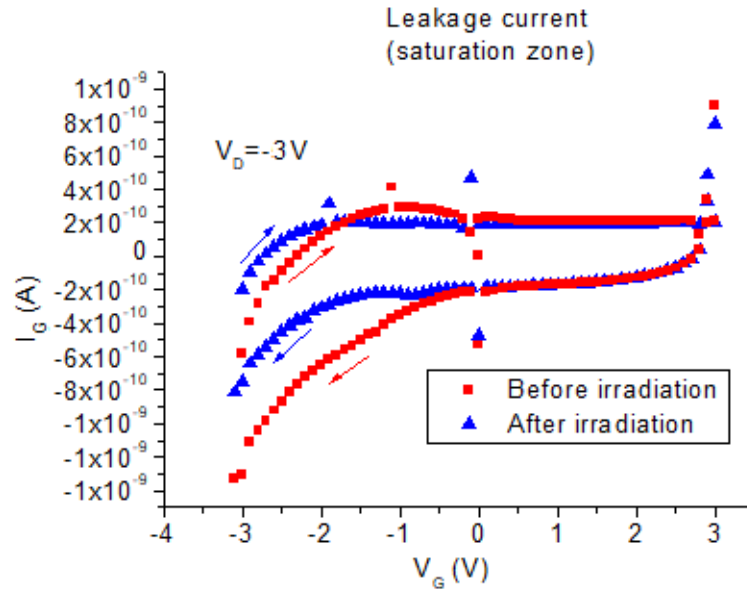


**Figure A.16:** Typical leakage current recorded during the acquisition of the transfer characteristic in the region of saturation in the devices realized by spin-coating from a solution of diF-TEG-ADT at wt.2%

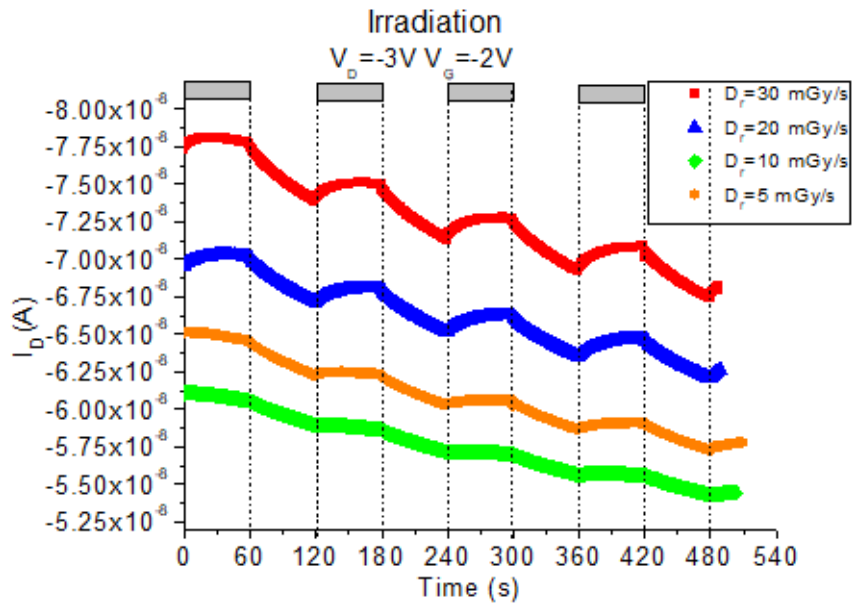


**Figure A.17:** Typical drain current acquired during four different irradiation cycles under X-ray beams having different dose-rates  $D_r$  in the devices realized by spin-coating from a solution of diF-TEG-ADT at wt.2%, biased at  $V_D = -3V$  and  $V_G = -2V$ .

# Bibliography

- [1] F. A. Boroumand, M. Zhu, A. B. Dalton, J. L. Keddie, P. J. Sellin, and J. J. Gutierrez, "Direct x-ray detection with conjugated polymer devices," *Appl. Phys. Lett.*, 2007.
- [2] A. Intaniwet, C. A. Mills, M. Shkunov, P. J. Sellin, and J. L. Keddie, "Heavy metallic oxide nanoparticles for enhanced sensitivity in semiconducting polymer x-ray detectors," *Nanotechnology*, 2012.
- [3] C. A. Mills *et al.*, "Enhanced x-ray detection sensitivity in semiconducting polymer diodes containing metallic nanoparticles," *J. Phys. Appl. Phys.*, 2012.
- [4] H. Han *et al.*, "Enhancement of X-ray detection by single-walled carbon nanotube enriched flexible polymer composite," *Nanoscale Res. Lett.*, 2014.
- [5] A. Koehler and H. Baessler, *Electronic Process in Organic Semiconductor*. Wiley-VCH, 2015.
- [6] G. Mattana, "Realisation and Characterisation of Organic Electronic Devices for E-textiles applications," PhD thesis, Università degli Studi di Cagliari, 2011.
- [7] P. Cosseddu, "Correlation between interface-dependent properties and electrical performances in OFETs," PhD thesis, Università degli Studi di Cagliari, 2006.
- [8] A. M. Manotti and A. Tiripicchio, *Fondamenti di Chimica*. Casa Editrice Ambrosiana, 2006.
- [9] W. Brütting, *Physics of organic semiconductors*. Wiley-VHC, 2005.
- [10] A. Ciavatti, "Transport Properties and Novel Sensing Applications of Organic Semiconducting Crystals," PhD thesis, Alma Mater Studiorum Università di Bologna, 2014.
- [11] H. Klauk, *Organic Electronics II*. Wiley-VCH, 2012.
- [12] Y. N. Gartstein and E. M. Conwell, "High-field hopping mobility in molecular systems with spatially correlated energetic disorder," *Chem. Phys. Lett.*, vol. 245, no. 4, pp. 351–358, Nov. 1995.
- [13] A. Kahn, N. Koch, and W. Gao, "Electronic structure and electrical properties of interfaces between metals and  $\pi$ -conjugated molecular films," *J. Polym. Sci. Part B Polym. Phys.*, 2003.
- [14] C. D. Dimitrakopoulos and D. J. Mascaro, "Organic thin-film transistors: A review of recent advances," *Org. Electron.*, 2001.
- [15] J. Millman and A. Grabel, *Micro Elettronica*. McGraw-Hill, 1995.
- [16] D. Braga and G. Horowitz, "High-Performance Organic Field-Effect Transistors," *Adv. Mater.*, 2009.
- [17] L. Basiricò, A. Ciavatti, T. Cramer, P. Cosseddu, A. Bonfiglio, and B. Fraboni, "Direct X-ray photoconversion in flexible organic thin film devices operated below 1V," *Nat. Commun.*, 2016.
- [18] A. Facchetti, "Semiconductors for organic transistors," *Mater. Today*, vol. 10, no. 3, pp. 28–37, Mar. 2007.
- [19] M. Kitamura and Y. Arakawa, "Pentacene-based organic field-effect transistors," *J. Phys. Condens. Matter*, vol. 20, no. 18, p. 184011, 2008.
- [20] J. Takeya *et al.*, "Very high-mobility organic single-crystal transistors with in-crystal conduction channels," *Appl. Phys. Lett.*, vol. 90, no. 10, p. 102120, Mar. 2007.

- [21] N. Karl, "Charge carrier transport in organic semiconductors," *Synth. Met.*, vol. 133, pp. 649–657, Mar. 2003.
- [22] H. Chung and D. Ying, "Polymorphism as an emerging design strategy for high performance organic electronics," *J. Mater. Chem. C*, 2016.
- [23] Y. Diao *et al.*, "Understanding Polymorphism in Organic Semiconductor Thin Films through Nanoconfinement," *J. Am. Chem. Soc.*, vol. 136, no. 49, pp. 17046–17057, Dec. 2014.
- [24] J. Chen, C. K. Tee, M. Shtein, J. Anthony, and D. C. Martin, "Grain-boundary-limited charge transport in solution-processed 6,13 bis(tri-isopropylsilylethynyl) pentacene thin film transistors," *J. Appl. Phys.*, vol. 103, no. 11, p. 114513, Jun. 2008.
- [25] A. K. Hailey *et al.*, "Understanding the Crystal Packing and Organic Thin-Film Transistor Performance in Isomeric Guest–Host Systems," *Adv. Mater.*, vol. 29, no. 23, p. n/a-n/a, Jun. 2017.
- [26] N. A. Azarova *et al.*, "Fabrication of organic thin-film transistors by spray-deposition for low-cost, large-area electronics," *Org. Electron.*, vol. 11, no. 12, pp. 1960–1965, Dec. 2010.
- [27] G.-P. Rigas, M. M. Payne, J. E. Anthony, P. N. Horton, F. A. Castro, and M. Shkunov, "Spray printing of organic semiconducting single crystals," *Nat. Commun.*, 2016.
- [28] S. Subramanian, S. K. Park, S. R. Parkin, V. Podzorov, T. N. Jackson, and J. E. Anthony, "Chromophore Fluorination Enhances Crystallization and Stability of Soluble Anthradithiophene Semiconductors," *J. Am. Chem. Soc.*, vol. 130, no. 9, pp. 2706–2707, Mar. 2008.
- [29] Y. Mei *et al.*, "High Mobility Field-Effect Transistors with Versatile Processing from a Small-Molecule Organic Semiconductor," *Adv. Mater.*, vol. 25, no. 31, pp. 4352–4357, Aug. 2013.
- [30] C.-H. Kim *et al.*, "Strongly correlated alignment of fluorinated 5,11-bis(triethylgermylethynyl)anthradithiophene crystallites in solution-processed field-effect transistors," *Chemphyschem Eur. J. Chem. Phys. Phys. Chem.*, vol. 15, no. 14, pp. 2913–2916, Oct. 2014.
- [31] I. Temiño, F. G. Del Pozo, M. R. Ajayakumar, S. Galindo, J. Puigdollers, and M. Mas-Torrent, "A Rapid, Low-Cost, and Scalable Technique for Printing State-of-the-Art Organic Field-Effect Transistors," *Adv. Mater. Technol.*, 2016.
- [32] F. G. del Pozo *et al.*, "Single Crystal-Like Performance in Solution-Coated Thin-Film Organic Field-Effect Transistors," *Adv. Funct. Mater.*, vol. 26, no. 14, pp. 2379–2386, Apr. 2016.
- [33] S. Lai, P. Cosseddu, L. Basiricò, A. Ciavatti, B. Fraboni, and A. Bonfiglio, "A Highly Sensitive, Direct X-Ray Detector Based on a Low-Voltage Organic Field-Effect Transistor," *Adv. Electron. Mater.*, 2017.
- [34] G. F. Knoll, *Radiation Detection and Measurements*. John Wiley & Sons, 1999.
- [35] R. D. Evans, *The Atomic Nucleus*. Tata McGraw Hill Publishing Company Limited., 1955.
- [36] B. Fraboni, A. Ciavatti, L. Basiricò, and A. Fraleoni-Morgera, "Organic semiconducting single crystals as solid-state sensors for ionizing radiation," *Faraday Discuss.*, 2014.

- [37] P. Büchele *et al.*, “X-ray imaging with scintillator-sensitized hybrid organic photodetectors,” *Nat. Photonics*, vol. 9, no. 12, pp. 843–848, Dec. 2015.
- [38] S. L. Chuang, *Physics of Photonic Devices, 2nd Edition - Shun Lien Chuang*. John Wiley & Sons, 2009.
- [39] A. G. Milnes and D. L. Feucht, *Heterojunctions Metal Semiconductor Junctions*. Academic Press, 1972.
- [40] J.-P. Hong, A.-Y. Park, S. Lee, J. Kang, N. Shin, and D. Y. Yoon, “Tuning of Ag work functions by self-assembled monolayers of aromatic thiols for an efficient hole injection for solution processed triisopropylsilylethynyl pentacene organic thin film transistors,” *Appl. Phys. Lett.*, vol. 92, no. 14, p. 143311, Apr. 2008.
- [41] S. L. Chuang, *Physics of Optoelectronic Devices*. John Wiley & Sons, 2009.
- [42] K.-J. Baeg, M. Binda, D. Natali, M. Caironi, and Y.-Y. Noh, “Organic light detectors: photodiodes and phototransistors,” *Adv. Mater. Deerfield Beach Fla.*, vol. 25, no. 31, pp. 4267–4295, Aug. 2013.
- [43] L.-L. Chua *et al.*, “General observation of n-type field-effect behaviour in organic semiconductors,” *Nature*, vol. 434, no. 7030, pp. 194–199, 2005.
- [44] H. Sirringhaus *et al.*, “High-Resolution Inkjet Printing of All-Polymer Transistor Circuits,” *Science*, vol. 290, no. 5499, pp. 2123–2126, 2000.
- [45] H. T. Nicolai *et al.*, “Unification of trap-limited electron transport in semiconducting polymers,” *Nat. Mater.*, vol. 11, no. 10, pp. 882–887, 2012.
- [46] S. Yakunin *et al.*, “Detection of X-ray photons by solution-processed lead halide perovskites,” *Nat. Photonics*, 2015.
- [47] P. Beckerle and H. Strobele, “Charged particle detection in organic semiconductors,” *Nucl. Instrum. Methods Phys. Res. Sect. A*, 2000.
- [48] A. Intaniwet, C. A. Mills, M. Shkunov, H. Thiem, J. L. Keddie, and P. J. Sellin, “Characterization of thick film poly(triarylamine... semiconductor diodes for direct x-ray detection,” *J. Appl. Phys.*, 2009.
- [49] A. Intaniwet, M. Shkunov, J. L. Keddie, and P. J. Sellin, “High charge-carrier mobilities in blends of poly(triarylamine) and TIPS-pentacene leading to better performing X-ray sensors,” *Org. Electron.*, 2011.
- [50] B. Fraboni *et al.*, “Organic Semiconducting Single Crystals as Next Generation of Low-Cost, Room-Temperature Electrical X-ray Detectors,” *Adv. Mater.*, 2012.
- [51] A. Fraleoni-Morgera, L. Benevoli, and B. Fraboni, “Solution growth of single crystals of 4-hydroxycyanobenzene (4HCB) suitable for electronic applications,” *J. Cryst. Growth*, vol. 312, no. 23, pp. 3466–3472, Nov. 2010.
- [52] B. Fraboni *et al.*, “Solution-Grown, Macroscopic Organic Single Crystals Exhibiting Three-Dimensional Anisotropic Charge-Transport Properties,” *Adv. Mater.*, vol. 21, no. 18, pp. 1835–1839, May 2009.
- [53] B. Fraboni *et al.*, “Anisotropic charge transport in organic single crystals based on dipolar molecules,” *Org. Electron.*, vol. 9, no. 6, pp. 974–978, Dec. 2008.
- [54] B. Fraboni, A. Fraleoni-Morgera, and A. Cavallini, “Three-dimensional anisotropic density of states distribution and intrinsic-like mobility in organic single crystals,” *Org. Electron.*, vol. 11, no. 1, pp. 10–15, Jan. 2010.
- [55] J. Trotter, “A three-dimensional analysis of the crystal structure of p-benzoquinone,” *Acta Crystallogr.*, vol. 13, no. 2, pp. 86–95, Feb. 1960.
- [56] A. Ciavatti *et al.*, “Toward Low-Voltage and Bendable X-Ray Direct Detectors Based on Organic Semiconducting Single Crystals,” *Adv. Mater.*, 2015.

- [57] I. Clairand *et al.*, “Use of active personal dosimeters in interventional radiology and cardiology: Tests in laboratory conditions and recommendations - ORAMED project,” *Radiat. Meas.*, vol. 46, no. 11, pp. 1252–1257, 2011.
- [58] H. Wei *et al.*, “Sensitive X-ray detectors made of methylammonium lead tribromide perovskite single crystals,” *Nat. Photonics*, 2016.
- [59] S. Yakunin *et al.*, “Detection of gamma photons using solution-grown single crystals of hybrid lead halide perovskites,” *Nat. Photonics*, 2016.
- [60] T. W. Odom, J.-L. Huang, and C. M. Lieber, “Single-Walled Carbon Nanotubes. From Fundamental Studies to New Device Concept,” *Ann. N. Y. Acad. Sci.*, vol. 960, no. 1, pp. 203–215, Apr. 2002.
- [61] J. Geng and T. Zeng, “Influence of Single-Walled Carbon Nanotubes Induced Crystallinity Enhancement and Morphology Change on Polymer Photovoltaic Devices,” *J. Am. Chem. Soc.*, vol. 128, no. 51, pp. 16827–16833, Dec. 2006.
- [62] C. J. Brabec, S. Gowrisanker, J. J. M. Halls, D. Laird, S. Jia, and S. P. Williams, “Polymer-fullerene bulk-heterojunction solar cells,” *Adv. Mater. Deerfield Beach Fla*, vol. 22, no. 34, pp. 3839–3856, Sep. 2010.
- [63] S. O. Kasap, “X-ray sensitivity of photoconductors: application to stabilized a-Se,” *J. Phys. Appl. Phys.*, vol. 33, no. 21, p. 2853, 2000.
- [64] P. Cosseddu, S. Lai, M. Barbaro, and A. Bonfiglio, “Ultra-low voltage, organic thin film transistors fabricated on plastic substrates by a highly reproducible process,” *Appl. Phys. Lett.*, 2011.
- [65] J. W. Ward *et al.*, “Low-temperature phase transitions in a soluble oligoacene and their effect on device performance and stability,” *Appl. Phys. Lett.*, vol. 105, no. 8, p. 083305, Aug. 2014.
- [66] “Keithley SourceMeter 2614B Datasheet.” .
- [67] B. Crasemann, *Atomic Inner-Shell Physics*. Plenum Press, 1985.
- [68] M. Sperrin and J. Winder, *Scientific Basis of the Royal College of Radiologists Fellowship Illustrated questions and answers*. IOP Publishing, 2014.
- [69] “<http://rtigroup.com/home/barracuda-multimeter/>.” .